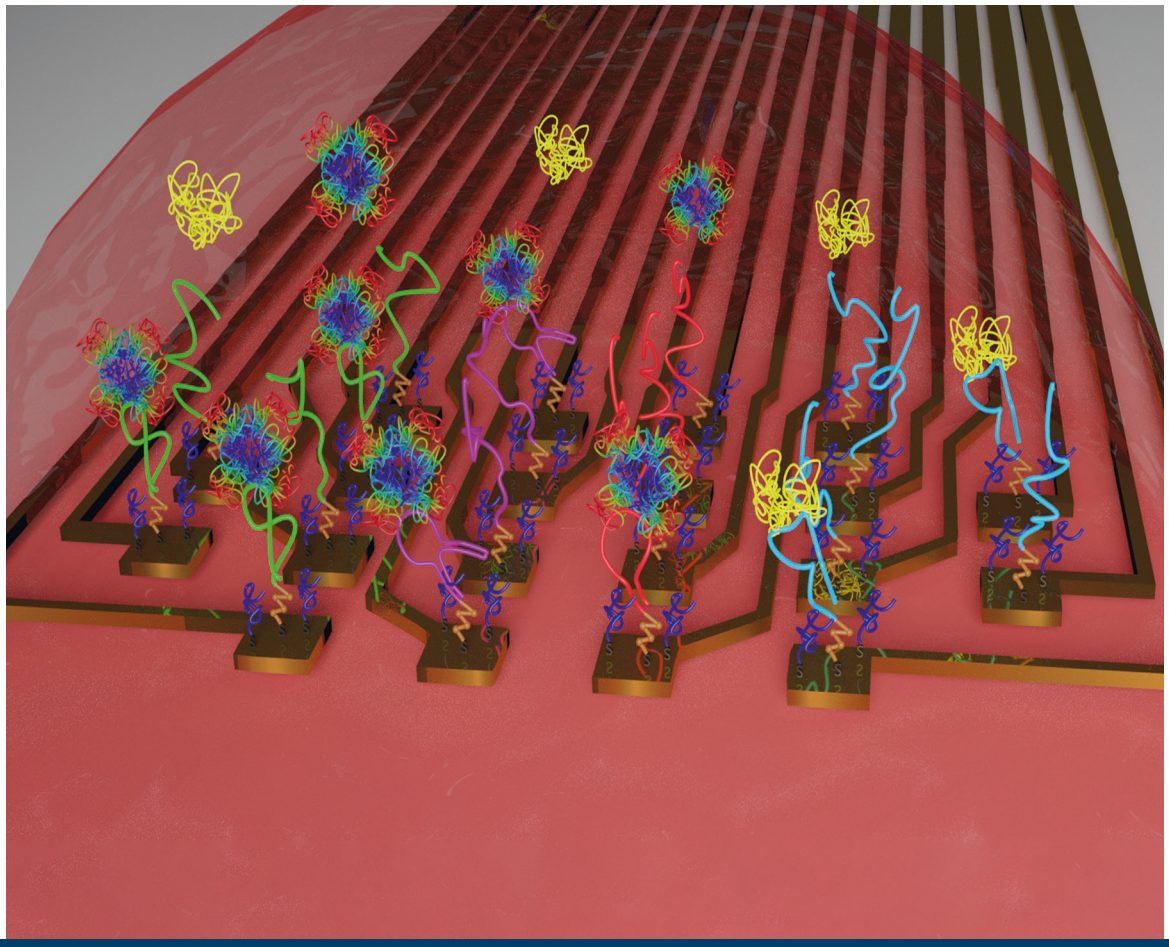

Development of Electrochemical Aptasensors for the Highly Sensitive, Selective, and Discriminatory Detection of Malaria Biomarkers

Gabriela Figueroa Miranda

Information
Band / Volume 75
ISBN 978-3-95806-589-5

Mitglied der Helmholtz-Gemeinschaft

JÜLICH
Forschungszentrum

Schriften des Forschungszentrums Jülich
Reihe Information / Information Band / Volume 75

Forschungszentrum Jülich GmbH
Institute of Biological Information Processing
Bioelectronics (IBI-3)

Development of Electrochemical Aptasensors for the Highly Sensitive, Selective, and Discriminatory Detection of Malaria Biomarkers

Gabriela Figueroa Miranda

Schriften des Forschungszentrums Jülich
Reihe Information / Information Band / Volume 75

ISSN 1866-1777 ISBN 978-3-95806-589-5

Bibliografische Information der Deutschen Nationalbibliothek.
Die Deutsche Nationalbibliothek verzeichnet diese Publikation in der
Deutschen Nationalbibliografie; detaillierte Bibliografische Daten
sind im Internet über http://dnb.d-nb.de abrufbar.

Herausgeber und Vertrieb:	Forschungszentrum Jülich GmbH Zentralbibliothek, Verlag 52425 Jülich Tel.: +49 2461 61-5368 Fax: +49 2461 61-6103 zb-publikation@fz-juelich.de www.fz-juelich.de/zb
Umschlaggestaltung:	Grafische Medien, Forschungszentrum Jülich GmbH
Druck:	Grafische Medien, Forschungszentrum Jülich GmbH
Copyright:	Forschungszentrum Jülich 2021

Schriften des Forschungszentrums Jülich
Reihe Information / Information, Band / Volume 75

D 82 (Diss. RWTH Aachen University, 2021)

ISSN 1866-1777
ISBN 978-3-95806-589-5

Vollständig frei verfügbar über das Publikationsportal des Forschungszentrums Jülich (JuSER)
unter www.fz-juelich.de/zb/openaccess.

ABSTRACT

Malaria, a vector-borne disease caused by *Plasmodium* parasites, still has high mortality rates, mainly in tropical and developing countries. Towards the desired malaria eradication goal, the "test, treat and track" policy of the world health organization (WHO) plays an important role. The early detection of malaria is crucial to provide timely and adequate antimalaria treatment. However, there is still need for the development of a low-cost, highly sensitive, selective, and quantitative malaria test that can also discriminate between the two more common *Plasmodium falciparum* and *Plasmodium vivax* malaria parasites for guiding a correct treatment. This research project aims to develop a novel, highly sensitive, and selective electrochemical aptasensor for discriminatory malaria detection. In this dissertation, the performance of a previously established electrochemical malaria aptasensor is optimized by means of the blocking molecules to detect malaria in biological samples. Posterous, the aptasensor detection was translated into two different transducer detection platforms for their characterization and possible application as point-of-care (POC) malaria detection technologies.

The first point was achieved by implementing a polyethylene glycol (PEG) film to suppress unspecific binding from human serum on an electrochemical malaria aptasensor fabricated on single gold macroelectrodes. A detailed study of the variation of the chemical and morphological composition of the aptamer/polyethylene glycol mixed monolayer as a function of incubation time was conducted. Higher resistance to matrix biofouling was found for polyethylene glycol than for hydrophobic alkanethiol films. The best sensor performance was observed for intermediate polyethylene glycol immobilization times. With prolonged incubation, phase separation of aptamer and polyethylene glycol molecules locally increased the aptamer density, thereby diminishing the analyte binding capability. Remarkably, polyethylene glycols do not affect the aptasensor sensitivity but enhance the complex matrix tolerance, dynamic range, and detection limit. Careful tuning of the blocking molecule immobilization is crucial to achieving high aptasensor performance and biofouling resistance.

Posteriorly, the previously optimized aptasensor detection was then translated from single gold macroelectrodes to fabricated flexible multielectrode array (flex-MEA) sensors. The low cost and robust polymer-based flex-MEAs facilitate the immobilization of different types of aptamer receptors, in this way, providing the possibility to discriminate between the *Plasmodium falciparum* and *Plasmodium vivax* parasitic infection. The first target biomarker was the abundant *Plasmodium* lactate dehydrogenase (PLDH) protein, expressed by both

parasite species and detected by 2008s, pL1, and LDHp11 aptamers. The second target was histidine-rich protein 2 (HRP-2), exclusively expressed by *P. falciparum* and detected by 2106s aptamer. The multi-target flex-MEA aptasensor detection was first tested in blood samples with the spiked proteins, showing broad and sensitive detection ranges for PLDH and HRP-2. Consecutively, the aptasensor detection was challenged in human whole blood samples spiked with *P. falciparum* and *P. falciparum* parasite *in vitro* cultures. In the last kind of sample, the performance of this electrochemical aptasensor was >75 % sensitivities for a parasitemia as lower as 0.001% (50 parasites/μL), overcoming the standards required by WHO. Together with a cost analysis, the obtained findings demonstrate the possible applicability of this low cost and robust fabricated multi-target flex-MEA aptasensor as a disposable POC test in marginal areas dealing with the prevalent malaria infection.

Another highly sensitive aptasensor was also fabricated by implementing reduced graphene oxide field-effect transistors (rGO-FETs) as second transducer platforms. Here, the pyrene-modified 2008s aptamer was utilized as a receptor molecule. An implemented extreme thermal annealing reduction step in the fabrication permitted to obtain rGO-FET devices with high performance. Such optimized transducer characteristics allowed this developed aptasensor to detect PfLDH down to subfemtomolar concentration, an order of magnitude smaller than the previously developed aptasensor and than other reported state-of-the-art electrochemical sensors. The electrical transduction mechanism of aptamer-PfLDH binding on rGO-FET is also discussed. The higher selectivity of 2008s aptamer for PfLDH was also corroborated versus human lactate dehydrogenase and a control aptamer. All those results also demonstrate the feasibility of this ultrasensitive fabricated rGO-FET aptasensor to detect PfLDH in human serum samples as possible POC test application.

In summary, two different transduction platforms were tested and optimized for the fabrication of an electrochemical malaria aptasensor. All optimized conditions allowed to achieve highly sensitive detection of malaria biomarkers. These developed technologies pave the way as promising detection platforms for future translation for the detection of other disease-related biomarkers.

ZUSAMMENFASSUNG

Malaria, eine durch Vektoren übertragene Krankheit, die durch Plasmodium-Parasiten verursacht wird, hat immer noch eine hohe Sterblichkeitsrate, vor allem in tropischen und Entwicklungsländern. Auf dem Weg zum angestrebten Ziel der Ausrottung von Malaria spielt die "Test, Treat and Track"-Politik der Weltgesundheitsorganisation (WHO) eine wichtige Rolle. Die Früherkennung von Malaria ist entscheidend, um eine rechtzeitige und adäquate Malariabehandlung zu ermöglichen. Es besteht jedoch noch Bedarf an der Entwicklung eines kostengünstigen, hochsensitiven, selektiven und quantitativen Malariatests, der auch zwischen den beiden häufigeren Malariaparasiten Plasmodium falciparum und Plasmodium vivax unterscheiden kann, um eine korrekte Behandlung zu steuern. Ziel dieses Forschungsprojekts ist die Entwicklung eines neuartigen, hochempfindlichen und selektiven elektrochemischen Aptasensors für den diskriminierenden Malaria-Nachweis. In dieser Dissertation wird die Leistungsfähigkeit eines bereits etablierten elektrochemischen Malaria-Aptasensors mit Hilfe von blockierenden Molekülen zum Nachweis von Malaria in biologischen Proben optimiert. Anschließend wurde der Aptasensor-Nachweis in zwei verschiedene Transducer-Detektionsplattformen übersetzt, um diese zu charakterisieren und als mögliche Point-of-Care (POC) Malaria-Nachweistechnologien einzusetzen.

Der erste Punkt wurde durch die Implementierung eines Polyethylenglykol (PEG)-Films zur Unterdrückung der unspezifischen Bindung aus menschlichem Serum auf einem elektrochemischen Malaria-Aptasensor erreicht, der auf einzelnen Gold-Makroelektroden hergestellt wurde. Es wurde eine detaillierte Studie über die Variation der chemischen und morphologischen Zusammensetzung der gemischten Aptamer/Polyethylenglykol-Monoschicht als Funktion der Inkubationszeit durchgeführt. Es wurde eine höhere Resistenz gegenüber Matrix-Biofouling für Polyethylenglykol als für hydrophobe Alkanethiol-Filme gefunden. Die beste Sensorleistung wurde für mittlere Polyethylenglykol-Immobilisierungszeiten beobachtet. Bei längerer Inkubation kam es zu einer Phasentrennung von Aptamer und Polyethylenglykolmolekülen, was die Aptamerdichte lokal erhöhte und damit die Analytbindungsfähigkeit verringerte. Bemerkenswerterweise beeinträchtigen Polyethylenglykole nicht die Empfindlichkeit des Aptasensors, sondern verbessern die Toleranz gegenüber komplexer Matrix, den dynamischen Bereich und die Nachweisgrenze. Eine sorgfältige Abstimmung der Blockierungsmolekül-Immobilisierung ist entscheidend, um eine hohe Aptasensorleistung und Biofouling-Resistenz zu erreichen.

Anschließend wurde die zuvor optimierte Aptasensor-Detektion von einzelnen Gold-Makroelektroden auf gefertigte flexible Multielektroden-Array (flex-MEA)-Sensoren übertragen. Die kostengünstigen und robusten polymerbasierten flex-MEAs ermöglichen die Immobilisierung verschiedener Arten von Aptamer-Rezeptoren und bieten so die Möglichkeit, zwischen der parasitären Infektion mit Plasmodium falciparum und Plasmodium vivax zu unterscheiden. Der erste Ziel-Biomarker war das reichlich vorhandene Plasmodium-Laktatdehydrogenase (PLDH)-Protein, das von beiden Parasitenarten produziert wird und von den Aptameren 2008s, pL1 und LDHp11 erkannt wird. Das zweite Ziel war das histidinreiche Protein 2 (HRP-2), das ausschließlich von P. falciparum produziert wird und von dem Aptamer 2106s erkannt wird. Der Multi-Target-Aptasensor flex-MEA wurde zunächst in den mit Proteinen versehenen Blutproben getestet und zeigte sowohl für PLDH als auch für HRP-2 einen breiten und empfindlichen Detektionsbereich. Anschließend wurde die Aptasensor-Detektion in menschlichen Vollblutproben, die mit P. falciparum und P. falciparum-Parasiten in vitro-Kulturen dotiert waren, getestet. In der letztgenannten Probenart lag die Leistung dieses elektrochemischen Aptasensors bei einer Sensitivität von >75 % für eine Parsitämie von nur 0,001 % (50 Parasiten/µL) und übertraf damit die von der WHO geforderten Standards. Zusammen mit einer Kostenanalyse zeigen die gewonnenen Erkenntnisse die mögliche Anwendbarkeit dieses kostengünstigen und robust hergestellten Multi-Target-Flex-MEA-Aptasensors als Einweg-POC-Test in Randgebieten, die mit der vorherrschenden Malariainfektion zu tun haben.

Ein weiterer hochempfindlicher Aptasensor wurde ebenfalls durch den Einsatz von ionenempfindlichen Feldeffekttransistoren aus reduziertem Graphenoxid (rGO-FETs) als zweite Transduktionsplattform hergestellt. Hier wurde das Pyren-modifizierte Aptamer 2008s als Rezeptormolekül verwendet. Durch einen thermischen Reduktionsschritt bei der Herstellung konnten rGO-FETs mit hoher Leistung hergestellt werden. Diese optimierten Wandlereigenschaften ermöglichten es dem entwickelten Aptasensor, PfLDH bis hinunter zu fM-Konzentrationen zu detektieren, eine Größenordnung kleiner als der zuvor entwickelte Aptasensor und als andere berichtete elektrochemische Sensoren nach dem Stand der Technik. Der elektrische Transduktionsmechanismus der Aptamer-PfLDH-Bindung am rGO-FET wird auch in dieser Arbeit diskutiert. Die höhere Selektivität des 2008er Aptamers für PfLDH wurde auch im Vergleich zur menschlichen Laktatdehydrogenase und einem Kontroll-Aptamer bestätigt. All diese Ergebnisse zeigen auch die Machbarkeit dieses ultrasensitiv hergestellten

rGO-FET-Aptasensors zum Nachweis von PfLDH in menschlichen Serumproben als mögliche POC-Testanwendung.

Zusammenfassend wurden zwei verschiedene Transduktionsplattformen getestet und für die Herstellung eines elektrochemischen Malaria-Aptasensors optimiert. Die optimierten Bedingungen ermöglichten eine hochsensitive Detektion von Malaria-Biomarkern. Diese entwickelten Technologien ebnen den Weg als vielversprechende Detektionsplattformen für die zukünftige Implementierung bei der Detektion anderer krankheitsbezogener Biomarker.

Table of Contents

Chapter 1

Introduction

Malaria, a vector-borne disease and one of the oldest known infectious diseases on earth, continues to have a high statistical incidence. Although all the investment and research for eradicating malaria and after an unprecedented period of success in global malaria control, progress has stalled. Data presented in the last world malaria report by the World Health Organization (WHO) highlights that "no significant progress in reducing global malaria cases was made" [1]. According to that report, there were estimated 229 million cases and up to 409000 deaths worldwide in 2019. Malaria is caused by *Plasmodium* parasites transmitted to humans through the bite of infected female *Anopheles* mosquitoes. There are five know species of the protozoan *Plasmodium* parasite. Among them, *Plasmodium falciparum* and *Plasmodium vivax* are responsible for most malarial morbidity and mortality.

Although malaria can occur in moderate temperature regions, it is most common in tropical and subtropical areas such as many parts of Sub-Saharan Africa, Southeast Asia, the northern half of South America, and Central America. The majority of the *P. falciparum* infections are found in the Africa region (99.7 %), while in South-East Asia and the American countries, both *P. falciparum* and *P. vivax* infections are prevalent [1]. *P. falciparum* is potentially deadly if not treated promptly and effectively, whereas *P. vivax* is less virulent but can cause relapse by dormant forms residing in the livers that require specific drug treatment.

Tropical and developing countries are most affected by this parasitic disease due to inappropriate healthcare infrastructure for prevention and care. With an early treatment start, infections with *Plasmodium* can be completely cured [2,3]. If the diagnosis is based merely on clinical symptoms, malaria can not only be confused with other diseases like enlarged spleen [4] or typhoid fever [5] but also leading to drug resistance and poor management of other febrile illnesses. Therefore, the WHO strongly advocates its policy of "test, treat and track" for improving the quality of care and surveillance of malaria. It is crucial not only to confirm the infection but also quantitatively discriminate between the two main malaria parasite species, *P. falciparum* and *P. vivax,* to correct guiding the treatment and the rational use of antimalarial

medicines [3,6]. Furthermore, WHO recommends that all suspected malaria cases should be confirmed by diagnostic testing before treatment is administered to not further fuel the parasite drug resistance[7].

The malaria diagnostic method must be accurate and easily available at the point-of-care (POC) since it is commonly needed in remote areas. The considered gold-standard method is the microscopy test, which consists of detecting parasites in the blood. However, due to the previously mentioned poor infrastructure in the malaria-endemic countries, microscopy-based diagnosis or adequate training in microscope handling is not available [8]. Malaria rapid diagnostic tests (RDTs), introduced widely over the past decade, can assist in making it easier and faster to discriminate between malarial and non-malarial fevers, and thus enabling timely and appropriate treatment. Their detection is based on antibody-antigen detection interaction, utilizing antibodies as receptor molecules. Unfortunately, such commercial RDTs still lack analytical sensitivity, and most of them do not discriminate between the malaria parasites [9–13]. Besides, the receptor antibodies have reduced thermostability at higher temperatures, considerable production costs, and have limited potential for chemical modifications to adapt them to other diagnostic platform technologies directly.

In this regard, more robust detection molecules like aptamers have been proposed [14–16]. Aptamers are short single-stranded artificial RNA or DNA oligonucleotides [17,18], peptides [19–21], or any of these chemically-modified molecules [22]. They recognize and bind to a target analyte with high specificity and strong affinity. Compared to antibodies, aptamers are thermostable, affordable, easily synthesized, and easily chemically modified. Hence, aptamers are an alternative remedy in overcoming difficulties associated with using antibody-based tests [10]. Several detection platforms with different transducers, ranging from optical to electrochemical, have been proposed by implementing aptamers as receptor molecules [10,12,23–26]. Those reported systems mainly sense protein biomarkers since they are upregulated for the infecting parasite's demanding metabolic rate. One of the main targeted proteins of RDTs is *Plasmodium* lactate dehydrogenase (PLDH), produced by all malaria parasites. This essential energy-converting enzyme can indicate a recent infection due to its correlation with the level of parasitemia [12,27,28]. The second common biomarker is histidine-rich protein 2 (HRP-2), which is also an abundant protein but exclusively expressed by the *P. falciparum* parasite. It has been found in red blood cells, serum, cerebrospinal fluid, and urine of malaria-infected patients [11,27]. A combination of receptors targeting these two main malaria biomarkers could be of great advantage in confirming the infection by excluding

false-positive tests and discriminating between *P. falciparum* and *P. vivax* parasites. Among the different implemented detection platforms, electrochemical sensors have demonstrated that they can outperform optical methods because of their high sensitivities, straight forward use, and operation detection, with the possibility of miniaturizing the electrodes and making them suitable for point-of-care (POC) applications [23]. However, despite the great variety in proposed electrochemical biosensors, a still missing task is to develop a low cost, stable, sensitive, quantitative, and discriminatory malaria biosensor. Based on the prior background, this dissertation research project aims to develop a novel, highly sensitive, and selective electrochemical multi-target biosensor for malaria detection based on *Plasmodium falciparum* LDH (PfLDH), *Plasmodium vivax* LDH (PvLDH), and *Plasmodium falciparum* HRP-2 discriminatory recognition by specific aptamer/target binding events.

An aptamer-based impedimetric malaria biosensor was previously developed on a single gold macroelectrode using the 2008s PfLDH aptamer and the hydrophobic 6-mercapto-1-hexanol (MCH) blocking molecule [29]. However, challenges were faced for this system to perform the detection of the biomarker directly in biological fluids, and it was only possible to measure in serum that was highly diluted (10 % serum). Since it is intended to fabricate a point-of-care malaria diagnostic biosensor, fabrication improvements were required in order to achieve the detection in biological samples. Polyethylene glycol (PEG), a hydrophilic material, has been widely used in biomedical devices as an antifouling coating since it possesses low interfacial energy in an aqueous medium. Consequently, proteins or cells closer to this material face thermodynamically unfavorable interactions that lead to their repulsion [30–32]. Owing to these antifouling properties, PEG has been used as a surface coating for various sensor materials such as quartz, silicon dioxide, gold, silver, or graphene [33–39]. Recently, the implementation of polyethylene glycol has also gained attention as a blocking molecule in biosensors [39–44]. In Chapter 4, the improved detection of the previously developed impedimetric aptasensor in human serum is presented by implementing a polyethylene glycol film as a blocking molecule. A detailed study of the variation of the chemical and morphological composition of the aptamer/polyethylene glycol mixed monolayer as a function of incubation time was conducted by quartz crystal microbalance with dissipation, X-ray photoelectron spectroscopy, contact angle, and atomic force microscopy. The optimized aptasensor sensitivity performance was achieved by monitoring different PEG immobilization times. The selectivity and stability of the aptasensor in human serum were also tested.

After the optimized detection in the biological samples, the aptasensor principle was translated to flexible substrate gold multielectrode array (flex-MEA) chips, Chapter 5. MEA chips have recently become an exciting approach for multi-target electrochemical biosensing [45–47]. The multi-target biosensing is a better way to discard false-positive results by detecting not only one, but several infection-related biomarkers. In this regard, MEA chips serve as a platform for immobilization of multiple aptamer types on the different electrodes that allow for simultaneous detection of multiple antigens via individually addressable aptasensors. The here fabricated, low cost and robust flex-MEAs facilitate the immobilization of different types of aptamer receptors, in this way, providing the possibility to discriminate between *P. falciparum* and *P. vivax* parasitic infection. The first target protein was PfLDH detected by 2008s, pL1, and LDHp11 aptamers [29,24,48,16]. The 2008s and pL1 also showed some selectivity for PvLDH. The second target protein was HRP-2, detected by 2106s aptamer [49]. First, the flex-MEA multi-target aptasensor was used for the detection of spiked analytes in blood. Posterous, the flex-MEA performance was also tested and characterized in *P. falciparum* parasitized blood samples. Comparative discussion of the performance of this aptasensor versus reported commercial RDTs was done throughout this chapter. Control experiments were also carried out with random ssDNA sequences and a receptor-free electrode surface, blocked with PEG. A final cost analysis of the flex-MEA multi-target aptasensor fabrication was included.

Reduced graphene oxide field-effect transistors (rGO-FETs) are highly sensitive devices, which can be used as label-free detection, provide a fast signal response, have easy operation, require small sample volume, and suppose low-cost mass production of nanoscale device dimensions [50]. Due to such characteristics that suggest them as suitable devices for point-of-care detection, rGO-FETs were implemented as a second detection platform for another aptasensor development (Chapter 6). The pyrene-modified 2008s aptamer was implemented as a receptor molecule. The improved rGO-FET characteristic performances, by the implementation of an extreme thermal annealing step, were demonstrated. The aptamer density on rGO-FET was optimized by different incubation times of the aptamer. The electrical transduction mechanism and a proposed model of aptamer-PfLDH binding on rGO-FET were discussed. The ultralow detection of the rGOFET aptasensor was proven in a buffer and human serum samples. The higher selectivity of the 2008s aptamer for detecting PfLDH was also demonstrated versus human lactate dehydrogenase and a control aptamer.

Chapter 2

Fundamentals and Theory

2.1 Aptamers

The term "Aptamer" was coined in 1990 by Andy Ellington. It stems from the Latin word "*aptus*", meaning to fit, and the Greek "*meros*", meaning part. Aptamers are short, single-stranded DNA or RNA (ssDNA or ssRNA) oligonucleotides [17,18], peptides [19–21], or any of these chemically-modified molecules [22]. They are incredibly versatile and bind their targets with high affinity and specificity. Among the different targets are proteins, peptides, carbohydrates, small molecules, toxins, and even whole cells [17,18,51]. Aptamers assume a variety of shapes due to their tendency to form helices and single-stranded loops. Target recognition and binding involve three-dimensional (3-D), shape-dependent interactions that include electrostatic interactions, hydrophobic interactions, base-stacking, and intercalation [18,52–54]. Aptamers bind because they "fit" their targets.

2.1.1 SELEX aptamer selection process

Aptamers with an affinity for the desired target are selected *in vitro* from an extensive oligonucleotide library through a process called SELEX, which stands for Systematic Evolution of Ligands by Exponential Enrichment [51,55,56]. Through an iterative process, randomly selected DNA sequences are incubated with the target; those non-binding sequences are discarded by elution. Then, only binding DNA aptamers to the proposed target are amplified by PCR. Multiple rounds of SELEX are performed, thus at the end, a DNA sequence with a high affinity for the target molecule is obtained (Figure 2.1).

Through this SELEX process, the 2008s aptamer was obtained in the group of Dr. J. Tanner, which has been reported to recognize the malaria biomarker *P. falciparum* lactate dehydrogenase (PfLDH) protein [14]. Some cross-selectivity was found for this aptamer versus *P. vivax* LDH (PvLDH). They also found another aptamer called 2106s that recognizes histidine-rich protein 2 (HRP-2) [49]. This protein is exclusively produced from the

P. falciparum parasite. The group of C. Ban reported the pL1 aptamer that recognizes not only *P. falciparum* but also *P. vivax* LDH (PvLDH) [15]. Recently, the development of a new aptamer (LDHp11) was reported that specifically bind to lactate dehydrogenase of *P. falciparum,* giving the possibility to discriminate between PfLDH and PvLDH proteins [16].

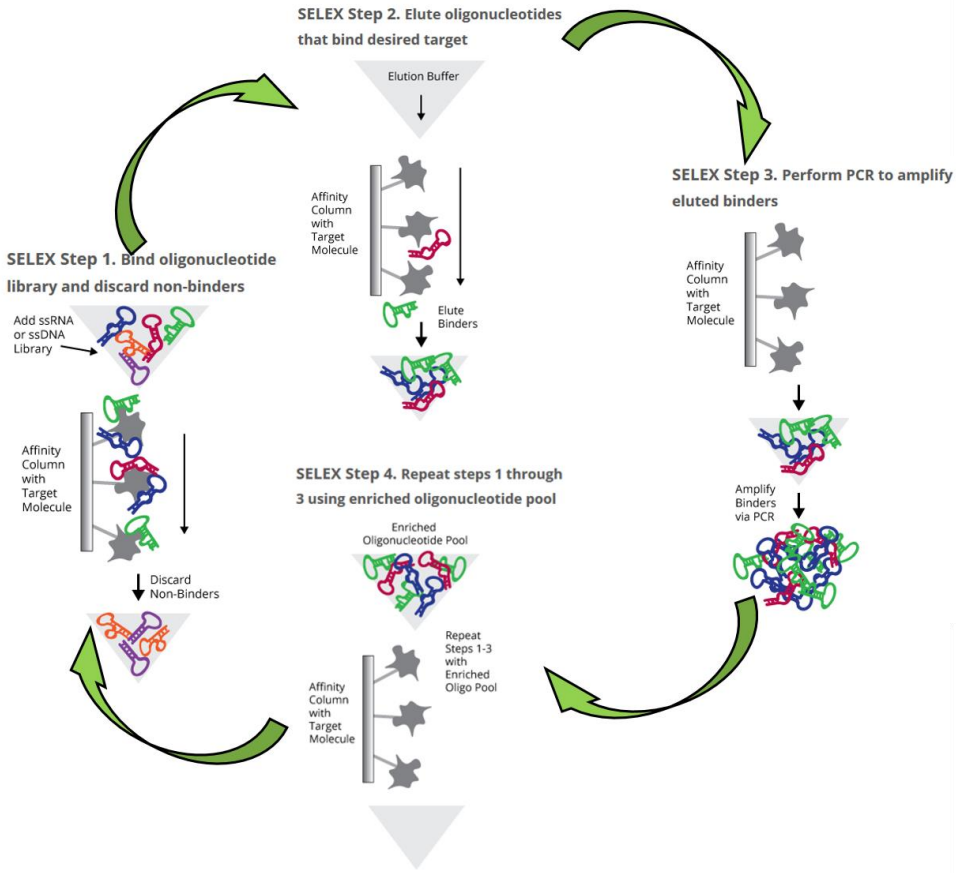

Figure 2.1 Systematic Evolution of Ligands by Exponential Enrichment (SELEX) process [57]. In the SELEX process, a set of randomly selected oligonucleotides is used to obtain the first binding sequences for a specific target, which usually is immobilized to an affinity column (Step 1). Consecutively the first bound sequences to the target are eluted from the column (Step 2) and amplified through polymerase chain reaction (PCR) in order to generate more copies of those binding sequences (Step 3). The previous steps are repeated several times to obtain only DNA sequences with high affinity for the target, which are known as aptamers (Step 4).

2.2 Electrochemical Aptamer-based Biosensor

2.2.1 Aptasensor characteristics

In 1956 Leland C. Clark, Jr., the biosensors' father, developed his first "Clark electrode", a device used to measure oxygen in the blood or other liquids, establishing with his invention the beginning of the biosensor's era [58]. According to the UIPAC, a biosensor is defined as a device that selectively transforms chemical information into an analytically useful signal. Besides the analyte (molecule to be detected) and a signal processing system, two essential components predict the performance of the biosensor: a biological recognition system, the *bioreceptor*, and a physicochemical *transducer* [59]. In the case of an aptasensor, as the name states, the bioreceptor used is an aptamer that specifically or selectively interacts with the target analyte (Figure 2.2). The transducer is in charge of converting the biorecognition event into a measurable signal. It produces a signal correlating with the kind of transducer used (electrical, optical, among others) that usually is proportional to the analyte-bioreceptor binding interaction taking place on the surface of the transducer. The signal amplification can be done as part of the same transducer (see section 2.4 G-FET) and also is integrated as part of the signal processor.

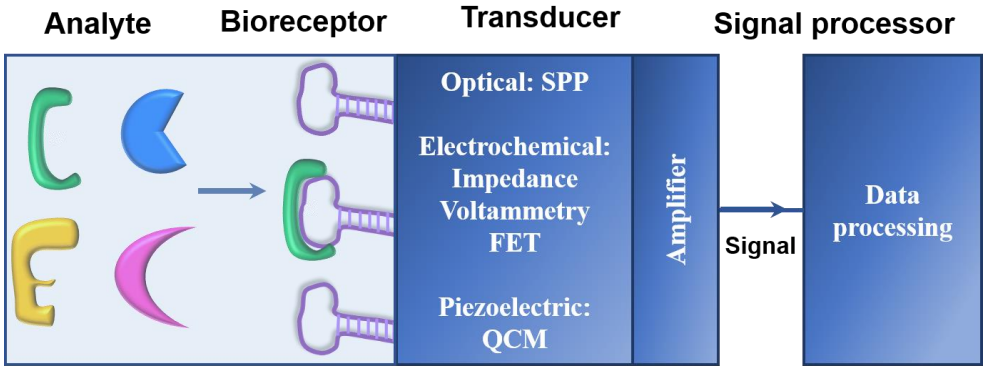

Figure 2.2 Schematic of the components of a biosensor. The analyte is the molecular compound to be detected. The main components of the biosensor are the bioreceptor molecule (here an aptamer) and the transducer. The amplification is often done in the transducer and intrinsically as part of the signal processor, which finally digitalizes the signal. SPP: surface plasmon polariton. FET: field-effect transistor. QCM: quartz crystal microbalance.

Aptamers process many advantages over antibodies when used as receptor molecules in biosensing. Some of those advantages include their *in vitro* obtention, as described before, through the SELEX process, so there is no need to use experimental animals for their production as required for antibodies [60–62]. The *in vitro* preparation also makes their fabrication cost cheaper. Aptamers possess mean melting temperatures above 40°C; thus, they are more thermostable than antibodies, which suffer from denaturation at such high temperatures [63,64]. Chemical modification of aptamers is easy, which in biosensing is of great usefulness for two reasons. On the one hand, they can be modified with tags, e.g., redox molecules, for their electrochemical detection. On the other hand, their chemical modification with different terminal groups (SH, NH_2, or pyrene) allows them to be immobilized on various solid supports with high stability, giving the possibility of signal regeneration without loss of integrity and selectivity [17,18,52].

Among the different transducers implemented in aptasensing, electrochemical methods have gained significant attention as transducer platforms. Electrochemical aptamer-based biosensors (aptasensors) have seen a fast implementation because of their characteristics like easy signal readout, fast response, high sensitivity, and cost-effective fabrication [51,65]. Those aptasensor characteristics, together with the fast development of technology that made the miniaturization of the electrodes possible, have helped to bring the research each time closer to the desired point-of-care detection application [66,67].

2.2.2 Performance factors

As with any relatively new technique, one needs to establish the criteria by which the performance of an aptasensor can be measured. Each aptasensor needs to fulfill specific performance requirements for a particular application. In this way, the successful clinical implementation of the aptasensor should be enabled.

- **Dynamic range of detection**: This is one of the essential characteristics that shows if the developed aptasensor can cover the analyte's detection in the relevant clinical concentration range, assuring the sensor's applicability. This parameter is defined as the concentration window from the minimum detectable quantity or limit of detection to the maximum unsaturated signal. The dynamic range of detection represents the linear response of a calibration curve in which the relationship between a measured analyte concentration (x) is proportional to the signal (y) response of the transducer [68,69]. The calibration curve can also be fitted to the Langmuir-Freundlich adsorption isotherm

(Eq. 2.1), which provides a simple model to describe the system's adsorption mechanism quantitatively and can be utilized to estimate the receptor-target binding affinity constant (k_{eq}) at equilibrium [70].

$$\theta = \frac{\theta_{max} k_{eq} \cdot c^n}{1 + k_{eq} \cdot c^n} \quad (2.1)$$

where θ is the measured signal (impedance, current, voltage) that correlates with the concentration of target detected, θ_{max} is the maximum possible signal obtained, c is the target concentration, and n is the homogeneity coefficient with a value from 0 to 1.

- **Limit of detection (LOD)**: This is the minimum quantity of a target analyte that can be detected, representing the lowers confidence detection value [69]. It can be calculated with the following formula, according to the IUPAC [71]:

$$LOD = \bar{B} + 3\sigma \quad (2.2)$$

where $\bar{B}$ is the average blank signal 3 represents the constant of random error (the typical value used as the signal-to-noise ratio), σ the standard deviation of the blank [71]. The LOD can also be obtained from the Langmuir-Freundlich fitting curve (Eq. 2.1) using the average blank signal obtained.

- **Sensitivity**: The sensitivity can be defined as the change in the sensor response for a given change in analyte concentration. It is calculated from the linear slope of the calibration curve. In general, the sensitivity is mainly limited by the intrinsic resolution of the used transducer platform to convert the binding event into a detectable signal [68,69].
- **Stability**: This parameter not only can tell how long the biosensor can be stored until an unreliable signal output is measured, but it also can give a correction factor for an expected drift. The stability is, in other words, the lifetime of the aptasensor [68,69].
- **Selectivity**: This factor is of the essence of a biosensor. Selectivity is the ability of the aptasensor to identify or discriminate the target analyte in a mixture of other interference molecules, especially in complex systems like blood or serum. That means that the signal generated by the aptasensor has to originate only from capturing the target molecule in such a complex system. Two factors usually determine the selectivity. The first one is the binding selectivity of the aptamer receptor to its target. The second factor

is the efficiency in passivating the free-aptamer transducer surface to prevent non-specific adsorption by applying a correct blocking molecule [68,69].

2.2.3 Immobilization methods

The immobilization of aptamers to a solid support is a crucial step, not only for assuring the proper receptor immobilization but also for controlling the surface density, accessibility, and stability of the surface-bound aptamer. Different immobilization methods can be applied according to the solid substrate's chemical nature intended to use for the aptamer immobilization. Those methods can be classified as:

- **Physical adsorption**: This occurs via electrostatic interactions, hydrophobic exclusion, van der Waals and London forces. That is not suitable for a stable sensor modification due to the weak bonding strength, causing the easy aptamer desorption from the surface. Physisorption occasionally occurs together with hydrogen bonds or charge-transfer forces [51,69,72]. This kind of immobilization is used, for example, to adsorbed aptamers onto multiwalled carbon nanotubes and their composites [73] or on graphene surface [74] together with electrochemical indicators such as methylene blue. Another example is the easy adsorption of ssDNA oligonucleotides like adenine (A) on gold surfaces, better known as PolyA-mediated DNA assembly [75,76].
- **Chemisorption**: This is also a simple but more effective immobilization method than physical adsorption. This method involves the covalent bonding between a functional group in the biomaterial to the supporting matrices. The functional groups usually involved in covalent bonding are SH, NH_2, COOH, OH, and C_6H_4OH [51,69,72]. Examples of this kind of immobilization have been shown on conducting single-walled carbon nanotubes (SWCNTs) [77,78], multiwalled carbon nanotubes (MWCNTs) [73,79,80], and reduced graphene oxide (rGO) [81] with amino-terminated aptamers. The gold-sulfur bond forms another standard immobilization of this classification. This kind of immobilization is highly implemented in electrochemical aptasensor fabrication and is achieved mainly by so-called self-assembled monolayers (SAMs), where thiol-labeled aptamers form a stable bond to a gold surface. They can create a dense monolayer via rigid intermolecular packing [51,82,83]. The aptamer receptors are often immobilized together with shorter backfill molecules such as mercapto alkanethiols or thiol-terminated polyethylene glycols into mixed monolayers to tune the optimal receptor density on the surface [43,82–85]. That keeps enough room

for the aptamer 3-D conformation with its target, ensuring the aptamers' high binding efficiency. On the other hand, the blocking molecule avoids non-specific adsorption, effectively reducing false-positive signals on the analysis results.

- **pi-pi interaction**: Because of the significant development of graphene-based materials in aptasensing, new immobilization methods have been generated by immobilizing pyrene like compounds to the graphene surface and linking an amino-terminated aptamer to this compound [39,86,87] or by directly immobilizing a pyrene-terminated aptamer on graphene [88,89]. The pyrene terminal group of the molecule and the graphene lattice form a non-covalent interaction between their aromatic groups. This immobilization form represents a non-invasive solution compared with covalent attachment, allowing the graphene to retain most of its electronic sensitivity [90].

2.3 Electrochemistry

By the end of the 18th century, the Italian physician and anatomist Luigi Galvani marked the birth of electrochemistry by establishing a bridge between chemical reactions and electricity. From his experiments with animal tissues, he proposed that the biological life forms possessed what he called *"nerveo-electrical substance"* [91]. In fact, electrochemistry studies the relationship between electricity, a measurable and quantitative phenomenon, and an identifiable chemical change. Thus, its reactions involve electric charges moving between electrodes and an electrolyte (ionic species in a solution) [92,93].

Before delving into the electrochemical analysis techniques, in this section, the electrode-electrolyte interface's electrical properties and the fundamental principles of an electrochemical cell are defined. Posteriorly, the fundamental principles of the electrochemical methods used in this work for the aptasensor characterization are described.

2.3.1 Electrode/electrolyte interface

In electrochemical systems, the transport of charge between an electronic conductor (an electrode) and an ionic conductor (an electrolyte) can be measured through different types of electrochemical techniques [68]. The charge is transported through the electrode by the movement of electrons (and holes). Typical electrode materials include solid metals (e.g., Pt, Au), liquid metals (Hg, amalgams), carbon (graphite, graphene), and semiconductors (indium-tin-oxide, Si). In the electrolyte phase, the charge is carried by the movement of contained ions in the solution, known as *supporting electrolyte*. The most frequently used

electrolytes are liquid solutions containing anionic and cationic species, such as H^+, Na^+, or Cl^-, most commonly in water. The electrolyte system must be sufficiently conductive for the electrochemical experiment envisioned to be useful in an electrochemical cell.

The electrode-electrolyte interface has been shown experimentally to behave like a double-plate capacitor. At a given potential, there will exist a charge (potential) on the electrode (φ_E) and a charge in the solution (φ_L). The whole array of charged species and oriented dipoles existing at the electrode-solution interface is called the *electrical double layer* (EDL). In 1879, Hermann von Helmholtz introduced a simple model for the EDL. The solution side of the double layer is thought to be made up of several "layers". The closest layer to the electrode contains solvent molecules and sometimes other species (ions or molecules) that are specifically adsorbed. This inner layer is also called the *inner Helmholtz plane* (IHP). Solvated ions can approach the electrode surface only to a certain distance; the locus of centers of these nearest solvated ions is called the *outer Helmholtz plane* (OHP) (Figure 2.3). The interaction of the solvated ions with the charged surface involves only long-range electrostatic forces. A potential is formed in this rigid layer (φ_H), which decays linearly from the electrode's surface towards the OHP ($\Delta\varphi_{rigid}$). The structure of the double layer can affect the rates of electrode processes [93].

Because of thermal agitation in the solution, the nonspecifically adsorbed ions are distributed in a three-dimensional region called the diffuse layer, extending from the OHP into the bulk of the solution. In 1913, Gouy and Chapman introduced another model that involves a *diffuse double layer* rather than a compact rigid layer, as in the Helmholtz model. Therefore, with this model, the structure inside the double layer remained unconsidered. A third model was proposed in 1924 by Otto Stern, name as Gouy-Chapman-Stern model. The model basically combines the Helmholtz model with the Gouy-Chapman model.

A final and complete model was proposed in 1947 by Grahame. In the Grahame model, Stern's work was further developed by considering the scenario when the ions lose their hydration shell and penetrate the Stern layer (Figure 2.3). The ions in the OHP region are less concentrated as compared to the IHP. Next to this layer comes the diffuse double layer. The diffuse double layer has a thickness usually represented by the *Debye length* (λ_D). The region starts from OHP into the solution up to the point where the surface effect is no longer present ($\Delta\varphi_{diffuse}$).

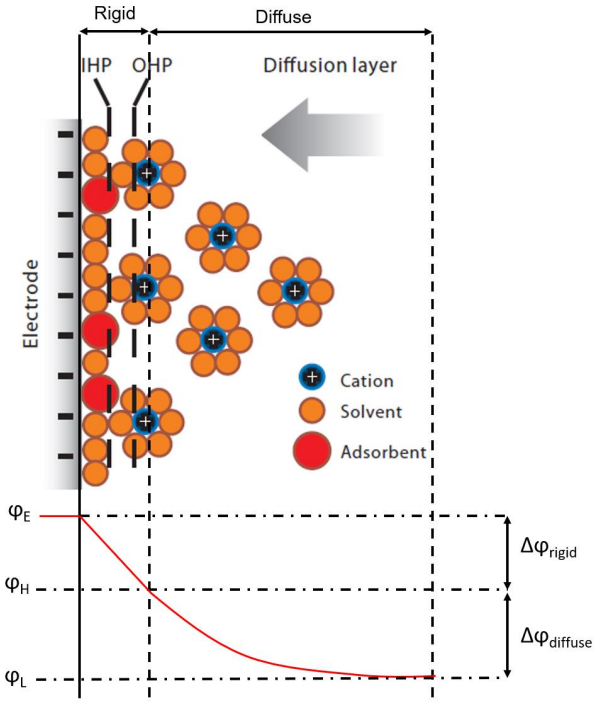

Figure 2.3 Schematic representation of the EDL formed at the electrode/electrolyte interface, according to the Grahame model. It contains a rigid plane closer to the electrode (Helmholtz or Stern layer), which is composed of the adsorbed molecules on the electrode (inner Helmholtz plane, IHP) and a second layer of solvated ions (outer Helmholtz plane, OHP). The diffuse layer contains those non-adsorbed and distributed ions that go from OHP into the solution's bulk. φ_E represents the electrode potential, φ_H the potential at the Helmholtz plane, φ_L the potential inside the solution, $\Delta\varphi_{rigid}$, and $\Delta\varphi_{diffuse}$, the lineal potential drop at the rigid plane and the exponential potential drop at the diffuse layer, respectively. Adapted from [94].

Therefore, the Debye length is highly dependent on the concentration of ions in the electrolyte solution. For instance, the Debye length for pure water is approximately 1 μm, while the Debye length for 1 M KCl dissolved in water is just 0.3 nm [68].

Besides, the transition in electric potential in crossing from one conducting phase to another usually occurs almost entirely at the interface. The high rate of the transition implies that a very high electric field exists at the interface, and it is expected to exert effects on the behavior of charge carriers (electrons or ions) in the interfacial region. Also, the magnitude of the potential difference at an interface affects the carriers' relative energies in the two phases; hence, it controls the direction and the rate of charge transfer. The potential sign is established relative to a reference potential, which is referred to the standard hydrogen electrode (standard for zero potential).

By conducting the electrode to more negative potentials, the energy of the electrons is raised. They can reach a level high enough to transfer into vacant electronic states on species in the electrolyte. In that case, a flow of electrons from electrode to solution, a *reduction current*, occurs (Figure 2.4a). Similarly, the energy of electrons can be lowered by imposing a more positive potential, and at some point, electrons of solutes in the electrolyte will find more favorable energy on the electrode and transfer there. Such electron flow, from the solution to the electrode, is known as an *oxidation current* (Figure 2.4b) [93].

2.3.2 Electrochemical cell

One must study the properties of collections of interfaces called *electrochemical cells.* These systems are defined most generally as two electrodes separated by at least one electrolyte phase. The overall chemical reaction taking place in a cell comprises two independent *half-reactions,* which describe the real chemical changes at the two electrodes.

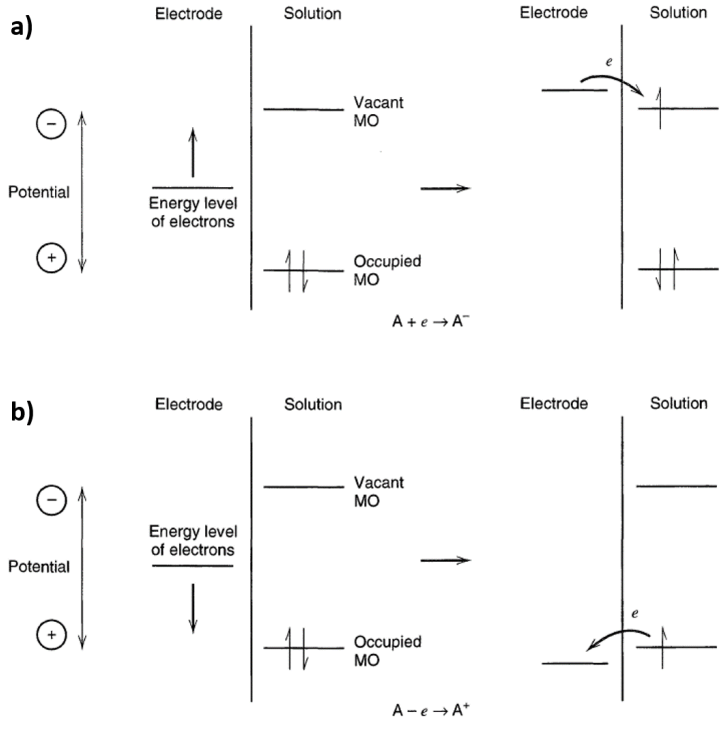

Figure 2.4 Representation of a) reduction and b) oxidation process of species, A, in solution. The shown molecular orbitals (MO) of species A are the highest occupied MO and the lowest vacant MO [93].

Most of the time, one is interested in only one of these reactions, and the electrode at which it occurs is called the *working electrode* (WE). To focus on it, one standardizes the other half of the cell by using an electrode called a *reference electrode* (RE) made up of phases having essentially constant composition. Since the reference electrode has a constant makeup, its potential is fixed. An example of RE is the commonly used *silver/silver chloride electrode* (Ag/AgCl/KCl, 3 M in water), with a potential of 0.21 V *vs. standard hydrogen electrode* (SHE) [92].

There exist two electrochemical cell designs commonly used. In the first case, if the current is small (less than 1-2 mV) that does not affect the potential of the reference electrode, the *two-electrode cell* configuration is used. In experiments where the current may be high, a *three-electrode cell* is preferable. In this arrangement, the current is passed between the working electrode and a *counter* (or *auxiliary) electrode.* The auxiliary electrode can be any convenient one (e.g., Platinum wire) because its electrochemical properties do not affect the working electrode [93].

The number of electrons that cross an interface is related stoichiometrically to the extent of the chemical reaction. The number of electrons is measured in terms of the total charge (Q) passed in the circuit. The charge is expressed in units of coulombs (C), where 1 C is equivalent to 6.24 X 10^{18} electrons. The relationship between charge and amount of product formed (N) is given by *Faraday's law* [92]:

$$Q = n\mathrm{F}N \tag{2.3}$$

where F is the Faraday's constant (96,485.3 C/mol) and n the number of transferred electrons. The current (i) is the rate of flow of coulombs (or electrons), where a current of 1 ampere (A) is equivalent to 1 C/s.

Processes which are not involving a charge transfer but rather the structure of the electrode-solution interface accompanied with a change of the electrode potential are called *non-Faradaic processes*. However, processes that involve electrochemical reactions follow Faraday's law, which means that they involve a flow of electrons (holes) transferred at the interface. Those reactions are called *Faradaic processes.* Both Faradaic and non-Faradaic processes occur when electrode reactions take place.

The critical potentials at which Faradaic processes occur are related to the *standard potential* ($E°$) of the specific chemical substances in the system. One can consider the following redox (a portmanteau of reduction and oxidation) reaction:

$$O + ne^- \rightleftharpoons R \tag{2.4}$$

where O is the oxidized species, R is the reduced species, and n the number of electrons exchanged between O and R. The relationship between the concentration of oxidized species, $[O]$, the concentration of reduced species, $[R]$, and free energy, is given as:

$$\Delta G = \Delta G^0 + \mathrm{R}T\, ln\frac{[R]}{[O]} \tag{2.5}$$

where R is the gas constant (8.3145 J/molK), and T is the temperature (K). The ratio of the reduced to oxidized species can be related to the Gibbs free energy change (ΔG, J/mol), from which one can derive the potential (E, V). When the E is the maximum potential between two electrodes, also known as the *open circuit potential* (OCP) or equilibrium potential, which is present when no current is flowing through the cell, and if the reactant and product have unit activity, then the equation can be written as:

$$\Delta G^0 = -n\mathrm{F}E^0 \tag{2.6}$$

In this case, the potential is known as the *standard electrode potential* (E^0, V) and relates to the *standard Gibbs free energy change* (ΔG^0 J/mol). The mathematical expression describing the correlation between potential and concentration for a cell reaction is a central tenant of electrochemistry and is known as the Nernst equation, obtained by combining equations 2.5 and 2.6 [92]:

$$E = E^0 + \frac{\mathrm{R}T}{n\mathrm{F}} ln\frac{[O]^*}{[R]^*} \tag{2.7}$$

where $[O]^*$ and $[R]^*$ are the bulk concentrations of the oxidized and reduced species.

2.3.2.1 Mass-transfer limited current

An electrochemical reaction taking place in an electrochemical cell is a *heterogeneous reaction* since it occurs at the electrode-electrolyte interface. Its rate also depends on mass transfer to the electrode, which plays a significant role in electrochemical dynamics. The typical mass transfer process taking place in an electrochemical reaction is *diffusion*, which is caused by the

movement of species under the influence of a concentration gradient. Assuming that the conversion of the redox species at the electrode is fast, then the net rate of the electrode reaction is governed mainly by the rate at which the electroactive species are brought to the surface. The expression that considers this phenomenon is the *mass-transfer limited current* (I_l, A), given by [92,93]:

$$I_l = n\mathrm{F}AmC^* \tag{2.8}$$

here the A (cm^2) is the area of the electrode, m denotes the *mass-transfer coefficient*, which is obtained from $m = D/\delta$, where D (cm^2/s) represents the diffusion coefficient, δ is the thickness of the diffusion layer, and C^* is the bulk concentration of the electrochemically active species.

The Cottrell equation, derived from Fick's second law of diffusion, predicts the current variation in time (t) when a potential step is applied under conditions of large overpotential and for an unstirred solution.

$$I(t) = \frac{n\mathrm{F}AD^{1/2}C^*}{\pi^{1/2}t^{1/2}} \tag{2.9}$$

2.3.3 Electrochemical Impedance Spectroscopy

The electrochemical impedance spectroscopy (EIS) is an electrochemical technique known and applied for more than a century [95]. In the field of biosensors, it is of particular interest as a tool for characterizing surface modifications like the detection of binding events [96].

The impedance (Z) of a system is determined by applying an alternating voltage perturbation of small amplitude and detecting the current response (Figure 2.5a). The term spectroscopy derives from the fact that the impedance is monitored in a range or spectrum of frequencies most of the time. From the definition, impedance is the quotient of the voltage-time function, $V(t)$, and the resulting current-time function, $I(t)$ [97]:

$$Z = \frac{V(t)}{I(t)} = \frac{1}{Y} \tag{2.10}$$

In analogy to the conductance definition in a dc circuit, one can define the admittance (Y) as the reciprocal impedance or complex conductance. The impedance is a complex value since the current can differ in the amplitude (as in the case for a pure ohmic resistance) and show a phase shift compared to the voltage-time function. Thus, the value can be described either by the modulus ($|Z|$) and the phase shift (θ) or by the real part (Z_R) and the imaginary part (Z_I) of the

impedance (Figure 2.5b). The first way of representing it is by the *Bode plot*, where $|Z|$ and θ are plot versus the logarithm of the measured frequency range ($\log f$) (Figure 2.5c) [97]. The impedance can be computed in its polar form as:

$$Z = |Z|e^{j\theta} \tag{2.11}$$

The second way of representing impedance is the so-called *Nyquist plot*, which is obtained by plotting Z_R versus Z_I (Figure 2.5d) [96]. In this way of representation, the impedance is obtained by its Euler's form as:

$$Z = Z_R + jZ_I \tag{2.12}$$

where j is $\sqrt{-1}$, which represents the complex number coming from the imaginary part of the impedance.

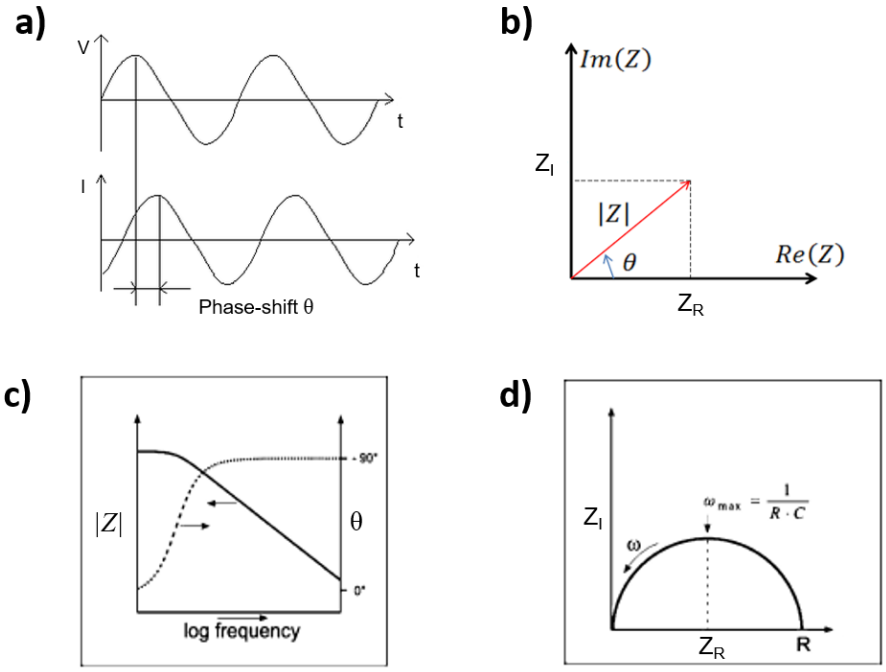

Figure 2.5 a) Impedance is defined as the quotient of the voltage, V (time), and current, I (time) function. b) Impedance can be represented as of the phase angle (θ) and modulus ($|Z|$) or as its real (Z_R) and imaginary (Z_I) components. c) Bode plot representation of impedance by $|Z|$ and θ over the whole range of log frequency measured. d) Nyquist plot representation of impedance by Z_R versus Z_I of a parallel RC element [97].

EIS uses electrical equivalent circuits (EECs) as models to describe the phenomena taking place at the electrode-electrolyte interface and to fit the experimental data. The current flowing at an electrified interface due to an electrochemical reaction always contains non-Faradaic components, no matter how well the measurement is made. The Faradaic part arises from the charge transfer via a reaction like the one shown in Eq. 2.4, across the interface by the charge-transfer resistance (R_{ct}) at the standard electrode potential and by the solution resistance (R_s) (Figure 2.6). The non-Faradaic current results from charging the double-layer capacitor. More commonly, a constant phase element (CPE) is used to fit the impedance measurements instead of a capacitor due to intrinsic inhomogeneities of the electrode surface [98–100]. Due to the reaction taking place near the electrode surface, the mass transport also plays a role in determining the electron transfer rate. Therefore, another term known as Warburg impedance is introduced (Z_W).

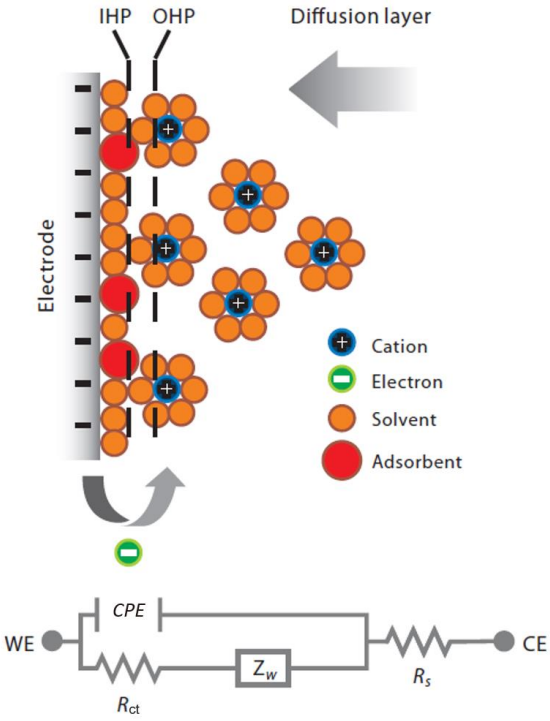

Figure 2.6 At the top, an electrified interface is depicted in which the electrode is negatively charged, countercations are aligned along with the electrified interface. At the bottom are the electrical circuit elements corresponding to each interface component. The high-frequency impedance components are *CPE*, double-layer capacitor represented by a constant phase element; R_{ct}, charge transfer resistance; and R_s, solution resistance. The low-frequency component is Z_W, Warburg impedance. WE, working electrode, and CE, counter electrode [94].

Those electrical elements form part of the so-called Randles equivalent circuit, which is the most commonly used circuit [94,97]. However, other kinds of modified Randles models have been reported, like the simplified Randles model, which does not consider the Z_W due to the mass transport process not taking place in the measured frequency range [98]. A Nyquist plot shows a characteristic form of the semicircle at higher frequencies correlated with the charge transfer control process by R_{ct}, and a straight line at low frequencies, which correlates with the diffusion control process by Z_W, if taking place (Figure 2.5d).

2.3.4 Voltammetry

In voltammetry, one applies a time-dependent potential (E) to an electrode via an electrochemical cell and measure the resulting current (I) flowing through the cell. The resulting plot of current versus applied potential is called a voltammogram [101]. In many cases, the applied potential is varied, or the current is monitored over a period of time (t) [101,102]. In this section, the principle of the voltammetric techniques used for the aptasensor detection (differential pulse voltammetry) and characterization (cyclic voltammetry and chronocoulommetry) are described.

2.3.4.1 Differential pulse voltammetry

As compared with linear sweep voltammetry (LSV), where the electrode potential varies at a constant rate (Figure 2.7a), in differential pulse voltammetry (DPV), the applied potential consists of a ramp with superimposed small-amplitude potential pulses (Figure 2.7b). The current is sampled directly before each pulse, and this value is subtracted from the current measured at the end of the pulse. By sampling the current just before the potential is changed, the effect of the charging current can be decreased. Thus, the current is given in the differential form, and the peaks for electrolyzed species (redox probes) are much sharper than found in other voltammetric methods (Figure 2.7b). Considering the increment from negative towards positive potential, and according to the reaction shown in Figure 2.4b, an increased rate of electron transfer from the solution to the electrode takes place. A peak occurs since, at some point, the diffusion layer has grown sufficiently above the electrode so that the flux of reactant to the electrode is not fast enough to satisfy the amount of redox species on the surface of the electrode (Eq. 2.8). Therefore, the current begins to drop, limited then by diffusion transport, which follows the same behavior as predicted by the Cottrell equation (Eq. 2.9) [101,103,104]. In this case, the peak generated by sweeping the potential towards positive potential is known as anodic peak potential (E_{pa}).

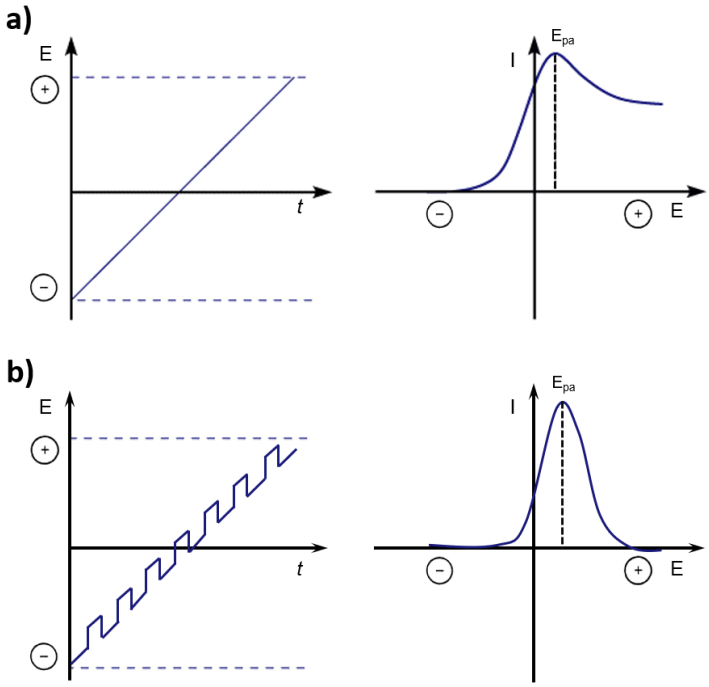

Figure 2.7 a) Linear sweep voltammetry and b) differential pulse voltammetry plots of potential (E) vs. time (t) and the correspondent current (I) vs. E. This last plot shows the characteristic anodic peak potential (E_{pa}) by sweeping from negative to a positive potential. Adapted from [104].

2.3.4.2 Cyclic voltammetry

Cyclic voltammetry (CV) is very similar to LSV. In this technique, the electrode potential is swept in forward and reverse scans (Figure 2.8). The electrode potential ramps in very small potential steps. Consequently, the current response comprises both fast charging and relatively slow Faradaic components. The voltammogram generated in CV has not only an anodic sweep with an anodic peak potential (E_{pa}) (forward scan), but also a cathodic sweep with a cathodic peak potential (E_{pc}) formed when reversing the scan from positive back to negative potentials (reverse scan) [72,102,104].

The peak height, I_p, is given by the Randles-Sevcik equation [69,72]:

$$I_p = 2.69 \times 10^5 n^{3/2} A D^{1/2} C^* v^{1/2} \qquad (2.13)$$

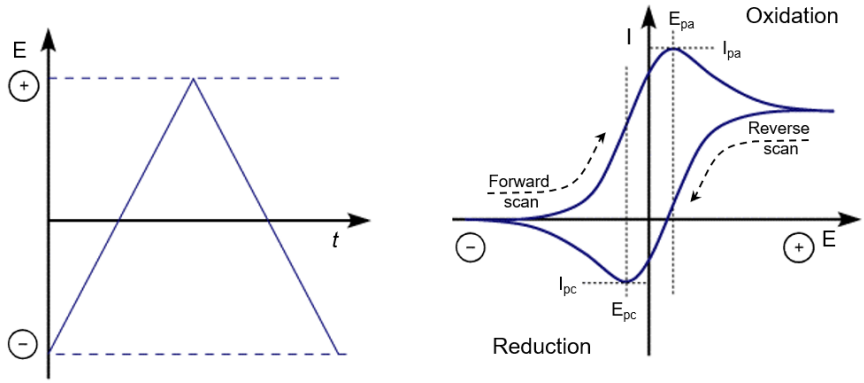

Figure 2.8 Plot of potential (E) vs. time (t) in cyclic voltammetry (left) and corresponding cyclic voltammogram of a redox molecule (left). The voltammogram depicts the anodic and cathodic peak potentials (E_{pa}, E_{pc}) and corresponding peak currents (I_{pa}, and I_{pc}). Adapted from [104].

where n is the number of transferred electrons, A the electrode area, D is the diffusion coefficient, C^* is the bulk concentration of the electrochemically active species, and v is the scan rate (V/s).

The location of the peaks on the voltage axis is useful for the identification of compounds. If the electron transfer process is fast compared with other processes (such as diffusion), the reaction is said to be electrochemically reversible, and the peak separation (ΔE_p) is:

$$\Delta E_p = E_{pa} - E_{pc} = \frac{59}{n}\ [\text{mV}] \tag{2.14}$$

In many cases, the mid-point between E_{pa} and E_{pc} values is identical to the standard electrode potential (E^0) (see Eq. 2.6) [102]:

$$E^0 = \frac{E_{pa}+E_{pc}}{2} \tag{2.15}$$

2.3.4.3 Chronocoulommetry

Chronocoulometry (CC) is an analytical method that monitors the relationship between charge (Q) and time (t). CC is employed to interrogate charge changing events happening at the electrode's surface by measuring the time-dependent flow of charge in response to an applied potential step waveform [69,105]. Commonly, the potential step starts right before and ends after the redox potential of the redox species of interest to keep the contribution from the charging current as small as possible but include all surface-confined redox molecules. This

technique is a more sensitive and reliable approach for detecting surface-confined electroactive species than current-based electrochemical methods. With this method, it is easy to distinguish between contributions from double-layer charging and absorbed species using the Cottrell plot (Q as a function of t, Figure 2.9). Thus, one can accurately measure redox charges confined at the electrode surface [105].

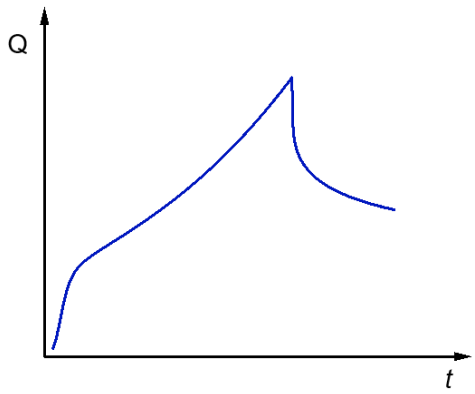

Figure 2.9 The charge-time profile associated with the potential step of a redox process.

2.4 Graphene-based field-effect transistor (G-FET) principle

A transistor is a semiconducting electrical element used to amplify or switch electrical signals upon applying an external bias and a control (often called gate or base) voltage. The field-effect transistor (FET) is a type of transistor that uses an electric field to control the conductivity within a semiconducting channel by varying the electric field applied via a gate electrode. It consists of *source* (S), *drain* (D), and *gate* (G) electrodes. The S and D electrodes are in direct contact with the channel, while the G electrode is separated via a dielectric or an electrolyte. When a potential is applied to the G electrode, it can facilitate the flow of charge carriers between S and D electrodes or interrupt the circuit, thus acting as a switch [90,106,107].

The operational principle of graphene-based sensors relies on the interaction of biomolecules with the graphene surface. Those molecules affect the free flow of charge carriers in graphene and are immediately detected as a change in conductivity. This perturbation leads to the real-time observation of biomolecular binding events without the need for labels. When graphene is used as the 2D semiconductor channel material to implement a biosensor FET (BioFET), and this channel is functionalized with bioreceptors, the biological recognition

and binding of the analyte species causes a variation of the charges near the graphene surface, resulting in modulation of the BioFET channel conductance. Most biomolecules (proteins, antibodies, nucleotides, amino acids, among others) carry charged groups and thus an effective net-charge, which alters the charge distribution at the graphene/medium interface and, consequently, within the BioFET channel (Fig 2.10).

The transistor's field-effect behavior is obtained by plotting the drain-source current (I_D) versus the applied gate potential (V_G) applied (Fig 2.11). The field-effect behavior of graphene field-effect transistor (G-FET) shows a characteristic cone-like shape. On the left side (negative gate potentials), the current is dominated by holes, then reaches the minimum at the Dirac point (V_{Dirac}) where the number of charge carriers is minimal and then increases again on the right side (positive gate potentials), where the current is then dominated by electrons. The overall relation in the linear regimes of the plots can be expressed by the following formula [108]:

$$I_D = \frac{W}{L} C_{edl} \mu (V_G - V_{Dirac}) V_D \tag{2.16}$$

W and L stand for width and length of the channel, C_{edl} is the electrical double layer capacitance, μ is the charge carrier mobility, and V_D the drain-source bias potential. From this relation, the characteristic parameters of the G-FET can be obtained. One of those parameters is the transconductance (g), which indicates how much the I_D is changed (measured) upon changes in the V_G [108].

$$g = \frac{\partial I_D}{\partial V_G} \tag{2.17}$$

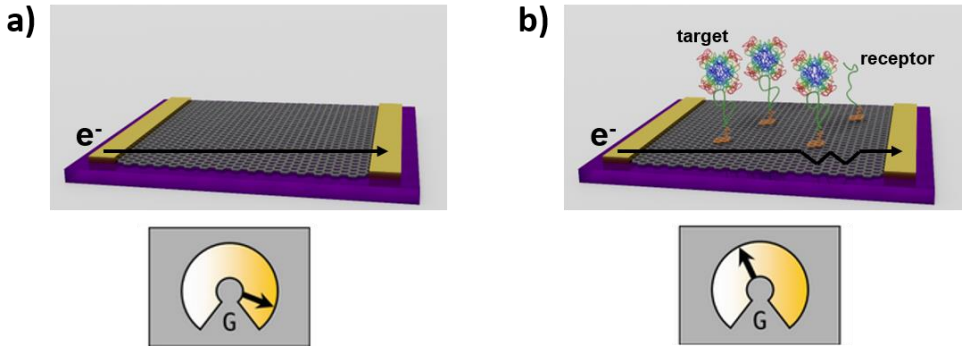

Figure 2.10 Graphene FET. a) Unimpeded electron flow. b) Changed conductivity of graphene due to surface receptor-target binding on the surface of graphene.

Thus, transconductance represents the sensitivity factor of the G-FET.

Another parameter is the electron/hole mobility (μ), which depends on the device properties, with the following formula [50]:

$$\mu = g \frac{L}{C_{edl} V_D} \tag{2.18}$$

where C_{edl} is the electrical double layer capacitance and can be calculated as:

$$C_{edl} = \frac{\varepsilon_r \varepsilon_0 A}{\lambda_D} \tag{2.19}$$

$$\lambda_D = \frac{0.304}{\sqrt{M}} \text{ [nm]} \tag{2.20}$$

ε_r is the dielectric permittivity of the buffer solution, consider as 78, ε_0 is the vacuum permittivity (8.85 $\times 10^{-12}$ F cm^{-1}), A is the surface area, and λ_D is the Debye length, which depends on the electrolyte molarity (M).

The standard graphene production methods for BioFETs include exfoliated graphene, chemical vapor deposition (CVD) of graphene, and production from reduced graphene oxide (rGO). This last one is the most implemented method in G-FET technology due to its low cost of production, high channel conductivity, and easy chemical modification [50].

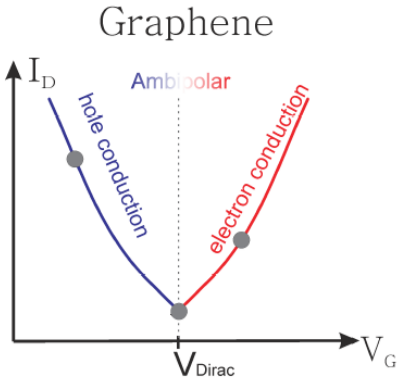

Figure 2.11 Field-effect behavior curve of the graphene-based FET devices. Graphene, as a zero-gap semiconductor, upon a small gate potential, jumps into either hole or electron conductivity and therefore is an ambipolar transistor. The minimum point is known as charge neutrality point or Dirac point (V_{Dirac}). Adapted from [108].

A model for rGO-electrolyte interface with negatively charged functional layer, originating from the remaining oxide containing functional groups after the thermal reduction of GO, is depicted in Figure 2.12 [109]. The model considers a negatively charged functional layer (FL) on top of rGO, which attracts positively charged ions on the Outer Helmholtz Plane (OHP) and forms the electrical double layer (EDL). The red-coloured line in Figure 2.12 shows the electrostatic potential profile across this interface. Applying Gouy-Chapman theory for solid-liquid interfaces gives us the charge distribution at the OHP of the interface, which can be shown as [110]:

$$\sigma_{OHP}(\psi_{OHP}) = -\left[\frac{(2\varepsilon_0\varepsilon_r)}{\lambda_D \beta e}\right] \sinh\frac{\beta e \psi_{OHP}}{2} \qquad 2.21$$

ψ_{OHP} is the potential at OHP, $\beta = 1/k_b T$, and λ_D is the Debye screening length (see Eq. 2.20), e is the electronic charge.

The electrostatic potential at the rGO-electrolyte interface (ψ_0) can be written as:

$$\psi_0(\psi_{OHP}) = \frac{\psi_{OHP} - \sigma_{OHP}(\psi_{OHP})}{C_{edl}} \qquad 2.22$$

where C_{edl} is represented by the specific capacitance of the Stern layer (see section 2.3.1).

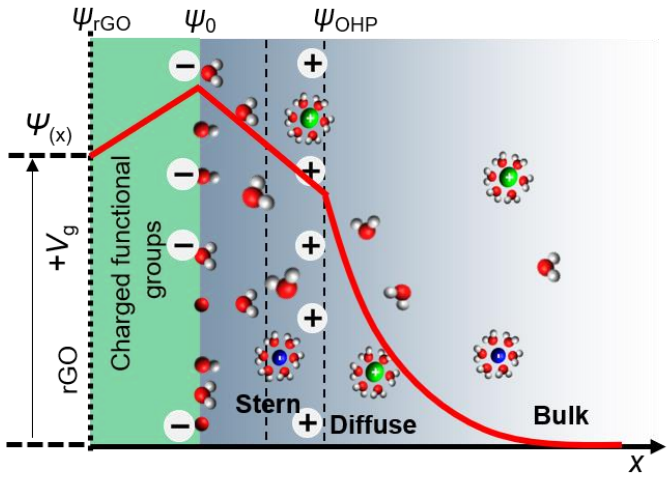

Figure 2.12 Schematic representation of the electrostatic potential at the rGO-electrolyte interface. Adapted from [110]

The acid-base dissociation constants (pK_a/pK_b) of the ionizable functional groups in the FL determine the sign of the charge distribution (σ_{OHP}) and the potential (ψ_0) at the FL-Stern interface. Langmuir-Freundlich theory can be applied to calculate the net charge density by assuming the highest surface charge densities at maximum protonation and dissociation of ionizable functional groups [111]. The charge-carrier density in the rGO upon applying a particular voltage at the reference electrode can now be given as:

$$\sigma_{rGO}(\psi_{OHP}) = \psi_{rGO} - \psi_0(\psi_{OHP}) \times C_{FL} \qquad 2.23$$

where ψ_{rGO} is the electrostatic potential of rGO. The capacitance of the functional layer (C_{FL}) can be given as $C_{FL} = \varepsilon_0\varepsilon_{rFL}/t_{FL}$ with ε_{rFL} and t_{FL} being the relative permittivity and the thickness of the functional layer, respectively [112].

2.5 Physicochemical characterization methods

In this section, the theoretical principle of the used physicochemical methods is described for the characterization of the aptamer/blocking molecule immobilization, the structural and chemical surface morphology, as well as the target detection.

2.5.1 Quartz crystal microbalance with dissipation

The quartz crystal microbalance with dissipation (QCM-D) method facilitates the determination of changes in the mass and viscoelastic properties of a molecular layer assembled on an electrode's surface. Here, the sensor oscillates at a specific frequency (*resonance frequency*) driven by an alternating voltage applied to a disc-shape, piezoelectric quartz crystal sandwiched between a pair of electrodes. The change in resonance frequency signal correlates with the number of added molecules, while the dissipation change corresponds to the rigidity of the adsorbed film (rigid or soft). For instance, a soft molecule layer causes a more significant change in the dissipation signal than a rigid molecule does (Figure 2.13) [113,114].

Therefore, in the QCM-D plot, the frequency decreases, and the dissipation changes when a molecular film binds to the sensor surface due to the molecules' added mass and the energy dissipation associated with the molecule's softness, respectively (Figure 2.14) [115].

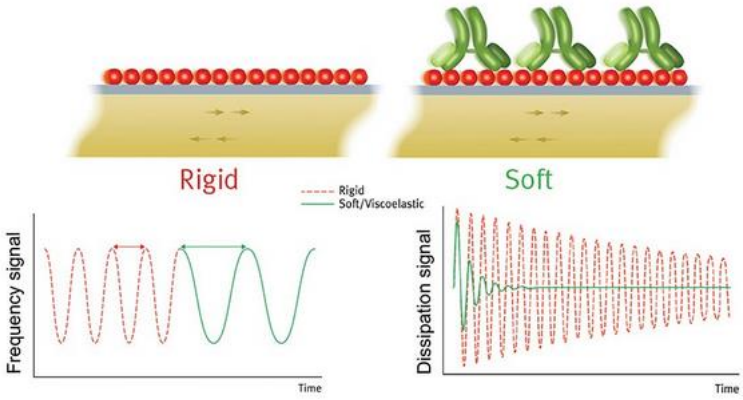

Figure 2.13 The frequency of the oscillating sensor crystal (gold) changes when the mass is increased by adding a molecular layer. Here antibodies (green) are added to a layer of protein (red). Difference in dissipation signal generated by a rigid (red) and soft (green) molecular layer on the sensor crystal [113].

For thin and rigid films, the frequency change, Δf, is proportional to the mass increase, which can be calculated with the Sauerbrey equation [116]:

$$\Delta f = \frac{2f_0^2}{A\sqrt{\rho_q \mu_q}} \Delta m \tag{2.24}$$

f_0 stands for the resonant frequency of the fundamental mode (Hz), Δf is the frequency change, Δm is the mass change, A is the area of the piezoelectrically active crystal, ρ_q is the density of quartz (ρ_q = 2.648 g/cm^3), and μ_q is the shear modulus of the quartz for AT-cut crystal ($\mu_q = 2.947\times10^{11}$ g/cm s^2).

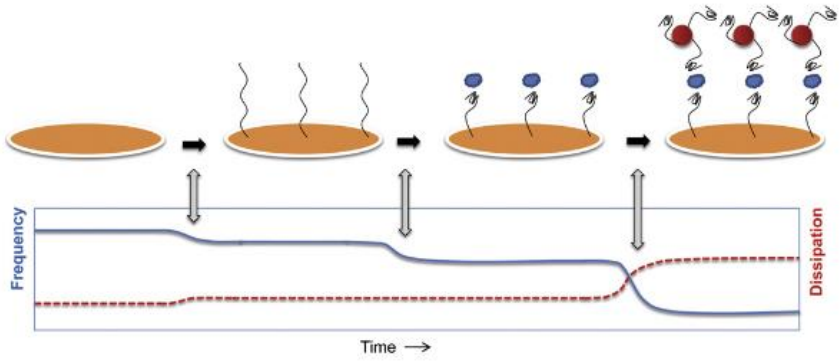

Figure 2.14 Schematic representation of a sandwich QCM-D biosensor for on-line detection. The solid curve shows the corresponding frequency shift and the dashed curve the dissipation shift for the above three steps [114].

Dissipation (D) occurs when the driving voltage to the crystal is shut off, and the energy from the oscillating crystal dissipates from the system. D is defined as:

$$D = \frac{E_{lost}}{2\pi E_{stored}} \tag{2.25}$$

where E_{lost} is the energy lost during one oscillation cycle, and E_{stored} is the total energy stored in the oscillator.

2.5.2 X-ray photoelectron spectroscopy

X-ray photoelectron spectroscopy (XPS) is a surface-sensitive quantitative spectroscopic technique that measures the elemental composition at the parts per thousand range, chemical state, and electronic state of the elements that exist within a material. It can define the elemental composition from the top (0-10 nm) of any solid conducting substrate [117,118].

The principle behind XPS relies on the excitation of photoelectrons during X-ray irradiation. In its simplest form, Photoelectron production describes a single-step process in which an electron initially bound to an atom/ion is ejected by a photon of the X-ray. Since photons are massless, chargeless energy packages, these are annihilated during photon-electron interaction with a complete energy transfer. If this energy is larger than the binding energy of the electron, it will result in the electron's emission from the atom/ion. The kinetic energy that remains on the electron is the quantity measured (Figure 2.15) [117]. Because the energy of an X-ray with a particular wavelength is known, and because the emitted electrons' kinetic energies are measured, the *electron binding energy* of each of the emitted electrons can be determined by using the equation based on the work of Ernest Rutherford [118]:

$$E_{binding} = E_{photon} - (E_{kinetic} + \phi) \tag{2.26}$$

where E_{binding} is the binding energy of the electron, E_{photon} is the energy of the X-ray photons being used, E_{kinetic} is the kinetic energy of the electron as measured by the instrument, and ϕ is the work function, which is an adjustable instrumental correction factor that accounts for the few electronvolts (eV) of kinetic energy given up by the photoelectron as it becomes absorbed by the instrument's detector. Thus, ϕ depends on both the spectrometer and the material. This equation is essentially a consequence of the conservation of energy.

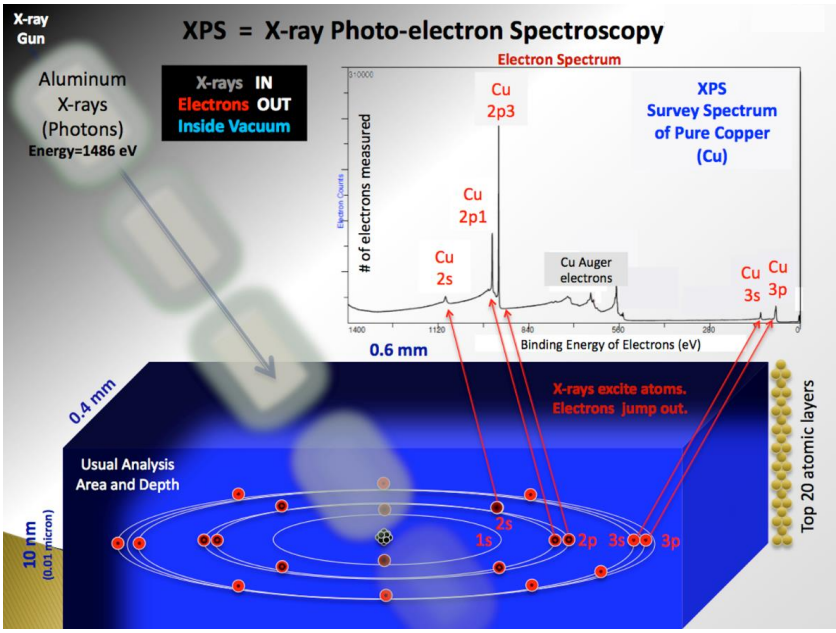

Figure 2.15 Schematic depicting the "Photoelectric Effect" process as it pertains to XPS [118].

A typical XPS spectrum is a plot of the number of electrons detected versus the binding energy of the photoelectrons (Figure 2.15). Each element produces a characteristic set of XPS peaks at characteristic binding energy values that directly identify each element that exists in or on the surface of the material being analyzed. These characteristic spectral peaks correspond to the electron configuration within the atoms (e.g., 1*s*, 2*s*, 2*p*, 3*s*, etc.). The number of detected electrons in each of the characteristic peaks is directly related to the number of atoms in a particular element within the XPS sampling volume. To generate atomic percentage values, each raw XPS signal must be corrected by dividing its signal intensity (number of electrons detected) by a *relative sensitivity factor* (RSF) and normalized over all of the elements detected. The high surface sensitivity of this method is a given due to the fact that only unscattered electrons are contributing to the element-specific XPS peaks. Photoelectrons excited with Mg or Al X-ray sources typically have kinetic energies (<1400 eV) that permit mean free paths of only a few nm in solids.

2.5.3 Contact angle

The contact angle is one of the most used measurement methods to study surface properties. It is an easy and quick method to estimate the surface free energy of a material surface. It can be used, for instance, to evaluate the adhesion and the homogeneity of hydrophilic and

hydrophobic molecules immobilized on a surface. The static contact angle is defined geometrically as the angle formed by a liquid at the three-phase boundary where a liquid, gas, and solid intersect (Figure 2.16) [119,120].

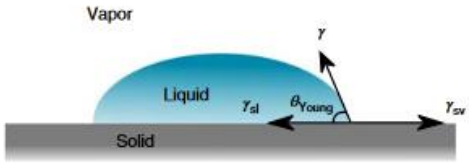

Figure 2.16 A drop of water on an ideal solid substrate. The Young contact angle, θ_{Young} is determined by a balance of the horizontal projection of the surface tension of the water along the solid surface ($\gamma \cos \theta_{Young}$) and interfacial tensions γ_{sv} and γ_{sl} [119].

The well-known Young equation describes the balance at the three-phase contact of solid-liquid and gas [119]:

$$\cos \theta_{Young} = \frac{\gamma_{sv} - \gamma_{sl}}{\gamma} \tag{2.27}$$

where θ_{Young} is the Young contact angle, γ_{sv}, and γ_{sl} the solid–vapor and solid-liquid interfacial tensions, respectively, and γ the surface tension of the liquid.

It can be seen that low contact angle values indicate that the liquid spreads on the surface, said that the liquid wets the surface (hydrophilic surface, if water is used as liquid), zero contact angle representing complete wetting. If the contact angle is greater than 90°, the surface is said to be non-wetting with that liquid (hydrophobic surface, if water is used as liquid), see Figure 2.17 [120].

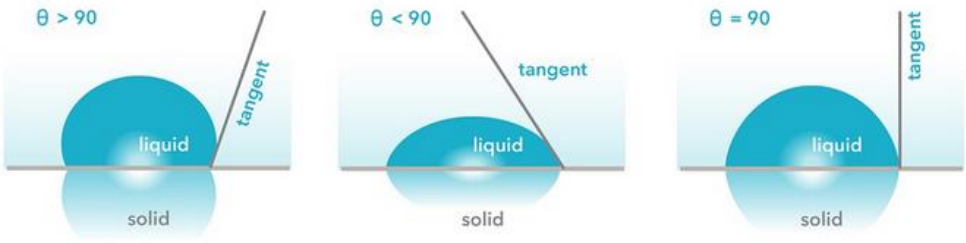

Figure 2.17 Contact angles indicating non-wettable (θ> 90°) and wettable (θ< 90°) surfaces [120].

2.5.4 Atomic force microscopy

The atomic force microscopy (AFM) is a tool that allows generating images of the sample surface topography with nanometric resolution, for example, to see even the structure of individual molecules. AFM has a significant advantage in that almost any sample can be imaged. The kind of samples can go from very hard, such as the surface of Si or SiO_2, or dispersion of metallic nanoparticles, to very soft, such as highly flexible polymers, lipid bilayers, or individual molecules of DNA. Its main feature is that the sample is probed by an ultrasharp tip keeping the interaction force between the sample and tip constant [121–123].

The AFM is made up of the following essential elements: Sample movement scanner, AFM probe (cantilever), laser beam source, photodetector and optical system, electronic feedback system, and computer with control software (Figure 2.18) [123,124].

The long and narrow cantilever is a microfabricated lever with a very sharp tip (typical curvature radius for commercial tips is 5-10 nm) that hangs off the bottom of the cantilever. This tip gets in touch with the sample's surface, resolving its shape with nanometric resolution. AFM cantilever material typically consists of either silicon or silicon nitride, where silicon nitride is reserved for softer cantilevers with lower spring constants. The cantilever's dimensions are critical as they also dictate its spring constant or stiffness [121,124]. This stiffness is fundamental to governing the interaction between the AFM cantilever tip and the sample surface and can result in low image quality if not chosen carefully. The relationship between the cantilever's dimensions and spring constant, k, is defined by the equation [124]:

$$k = \frac{Ewt^3}{4L^3} \tag{2.28}$$

where w is the cantilever width, t the cantilever thickness, L the cantilever length, and E Young's modulus of the cantilever material.

The scanner is in charge of moving the sample so that the probe can palpate the entire required surface. The AFM used in the scope of this thesis used a concept where the cantilever and laser system are fixed in position while the sample is moved up/down and side to side by the piezo scanner. The laser beam is reflected on the backside of the cantilever. The reflected laser beam is tracked by a position-sensitive photodetector (PSPD) that picks up the probe's vertical motion. These detectors' deflection sensitivity has to be calibrated in terms of how many nanometers of movement corresponds to a unit of voltage measured on the detector. In this way, the height differences of the sample are converted into vertical deflections of the cantilever.

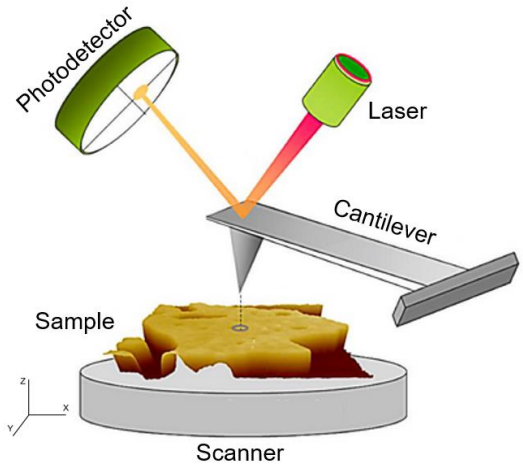

Figure 2.18 Outline of an AFM. The cantilever is kept in contact with the sample's surface, which moves with great precision in the XYZ axis thanks to a piezoelectric scanner. The cantilever's deflection is followed by a laser reflected on a photodetector, which allows its vertical movements to be detected with subnanometric precision [123].

The electronic feedback system is used to define a setpoint to maintain a particular force between the cantilever and the sample with the help of the piezo actuation. There are plenty of different AFM operation modes, but two of them are used more frequently than the others. The first one is the static mode (contact mode), where the cantilever is dragged across the sample's surface. Here the feedback parameter is the cantilever deflection (Figure 2.19a). The second mode is the dynamic mode (tapping mode), where the cantilever oscillates close to its resonance frequency. Here, the cantilever oscillation amplitude is used as a feedback parameter (Figure 2.19b). The feedback uses the detector signal to adjust it to a constant setpoint value, thus keeping the separation between the sample and the tip constant via the piezo element and compensating the sample topography. The voltage applied to the piezo to compensate the topography is used as height information to calculate the topography image [123,124].

Once the line-by-line image has been acquired, the software allows obtaining very accurate information at the metrological level. The maps obtained can be analyzed to extract information on object dimension, their distribution, and coverage, as well as the surface roughness. Although AFM cannot easily measure the thicknesses of films covering homogeneously the surface, since it is a surface topography method, it can determine the differences in heights, image profiles, distances between points, and many more at molecular resolution [123].

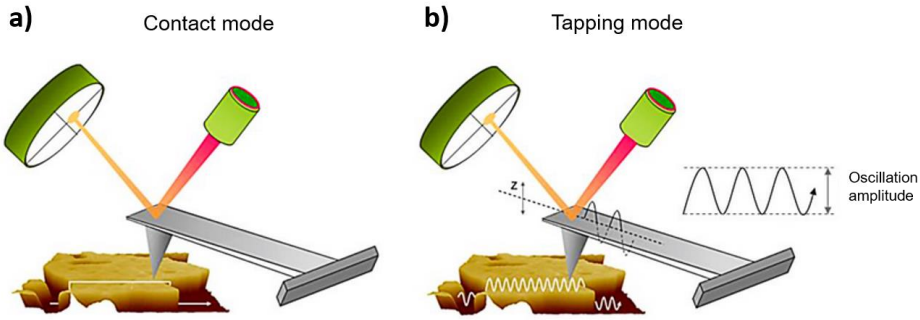

Figure 2.19 The two basic topographic modes of AFM. a) Contact mode, the probe follows the sample's surface in intimate contact while the feedback loop keeps the deflection of the cantilever constant. b) Tapping mode, the probe oscillates sinusoidally on the Z-axis and only contacts the sample sporadically. In this case, the feedback loop acts, not on the cantilever's deflection but on the amplitude of the oscillation of it. The photodetector also registers this magnitude by monitoring the laser's movement on it [123].

Chapter 3

Materials, equipments, and methods

In this chapter, chemicals, setups, and methods used for the electrochemical malaria aptasensor realization are described. Similarly, the fabrication and cleaning procedures for the devices used as detection platforms are described in detail. Finally, the implemented biofunctionalization steps and the different target detection as well as control experiments, performed in human serum or blood samples, are explained.

3.1 Materials

All the malaria single-stranded DNA (ssDNA) aptamer sequences and the control random ssDNA sequences used in this work were synthesized by Friz Biochem GmbH (Neuried, Germany), which are shown in Table 3.1. The control pyrene-terminated prostate-specific antigen (PSA) aptamer was purchased from Sigma-Aldrich Chemie GmbH (Germany). The recombinant *Plasmodium falciparum* lactate dehydrogenase (PfLDH), *Plasmodium vivax* lactate dehydrogenase (PvLDH), histidine-rich protein 2 (HRP-2), and human lactate dehydrogenase B (hLDHB) were obtained from bacterial expression as part of a collaboration with the group of Dr. J. Tanner from Honk Kong University. The whole blood samples with spiked *Plasmodium falciparum* parasites, *Plasmodium falciparum* parasites cultures, and control uninfected blood samples were obtained as part of a collaboration from the Institute of Tropical Medicine, Tübingen University. 25 mM Tris-HCl buffer (NaCl 0.1 M, Tris 25 mM, HCl 25 mM, pH 7.5), 10 mM phosphate-buffered saline (PBS, 10 mM sodium phosphate, NaCl 0.1 M, KCl 3 mM, pH 7.5), lysis buffer (25 mM Tris-HCl buffer with 0.5% Triton X-100), high salt concentration phosphate-buffered saline (PBS, 10 mM sodium phosphate with 1.0 M NaCl and 1 mM Mg^{2+}, pH 7.5), 0.1 M NaOH solution, and 0.05 M H_2SO_4 solution were prepared. All aqueous solutions were mixed using ultra-pure deionized water (18.2 MΩ cm, Milli-Q, Millipore, Merck, Darmstadt, Germany). Monofunctional methoxy-polyethylene glycol thiol (PEG, 2kDa) was purchased from Creative PEGWorks (New York, USA).

Table 3.1 Receptor aptamer sequences used for the multi-target flex-MEA aptasensor

Aptamer	Sequence
2008s	5'-HO-$(CH_2)_6$-S-S-$(CH_2)_6$-O- CTG GGC GGT AGA ACC ATA GTG ACC CAG CCG TCT AC-3'
Pyrene-modified 2008s	5'-Pyrene-$(CH_2)_4$- CTG GGC GGT AGA ACC ATA GTG ACC CAG CCG TCT AC-3'
pL1	5'-HO-$(CH_2)_6$-S-S-$(CH_2)_6$-O- GTT CGA TTG GAT TGT GCC GGA AGT GCT GGC TCG AAC-3'
LDHp11	5'-HO-$(CH_2)_6$-S-S-$(CH_2)_6$-O- CTA CTG TTG ATA TGA GTG ATA GGG CGG CGC GCT TAT CTG TAT TGT G -3'
2106s	5'-HO-$(CH_2)_6$-S-S-$(CH_2)_6$-O- GCT TAT CCG ATG CAG ACC CCT TCG GTC CTG CCC TC -3'
Random ssDNA 1	5'-HO-$(CH_2)_6$-S-S-$(CH_2)_6$-O- GGG CCC GTC CGT ATG GTG GGT GTG CTG GCC -3'
Random ssDNA 2	5'-HO-$(CH_2)_6$-S-S-$(CH_2)_6$-O- TTT TTT TTT TTT TTG CGG AGG AAG GT -3
PSA	5'- Pyrene-$(CH_2)_4$- TTT TTA ATT AAA GCT CGC CAT CAA ATA GCT TT-3'

Tris (2-carboxyethyl) phosphine hydrochloride (TCEP), potassium ferricyanide ($K_3[Fe(CN)_6]$), potassium ferrocyanide ($K_4[Fe(CN)_6]$) trihydrate, human serum albumin (HSA), and human serum from human male AB plasma were purchased from Sigma-Aldrich Chemie GmbH (Germany). Bovine serum albumin (BSA) was obtained from Gibco (Germany). Acetone, isopropanol, and ethanol were purchased from Merck (Darmstadt, Germany).

3.2 Electrode preparation

3.2.1 Gold rod electrode cleaning

Gold rod electrodes (GRE, 2 mm in diameter, Gaos Union Co, Wuhan, China) were intensively cleaned before aptamer modification (Figure 3.1) [125]. Briefly, the gold electrodes were consecutively polished with aqueous slurries of alumina powder of 0.3 and 0.05 μm on a micro cloth. Afterwards, the electrodes were sonicated in ethanol, isopropanol, and Milli-Q water for 5 min each and dried in a nitrogen stream.

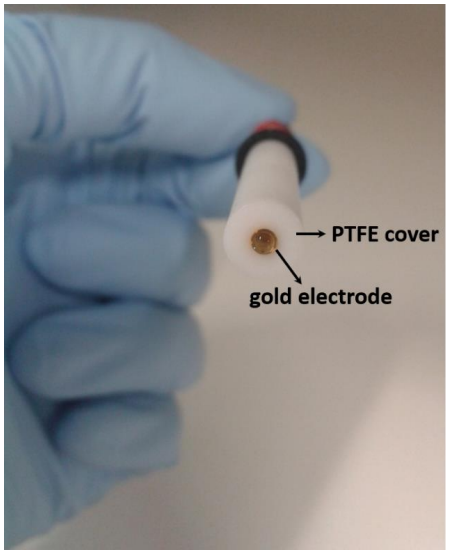

Figure 3.1 Picture of one GRE showing the gold electrode surrounded by a protective cover of PTFE material. The PTFE cover allows controlling the electrode's surface area when immersed in the solutions for the aptasensor fabrication and detection.

Then, they were activated with electrochemical cleaning by performing cyclic voltammetry (CV) with Autolab potentiostat/galvanostat PGSTAT302 (Eco Chemie, Netherlands) in a solution of 0.1 M NaOH and consecutively 0.05 M H_2SO_4. Finally, the electrochemical surface area (ESA) was determined by a CV in 0.05 M H_2SO_4 (see section 3.4.3) [126].

3.2.2 Flexible microelectrode arrays fabrication and cleaning

Flexible multielectrode arrays (flex-MEAs) were produced in collaboration with Song Chen, a master student of the same institute IBI-3, in an ISO 1-3 cleanroom on a polyethylene terephthalate (PET, DuPont Teijin Films Ltd) foil with a thickness of 100 µm and a diameter of 100 mm used as the flexible substrate (Figure 3.2a). A physical vapor deposition (PVD) process was performed to obtain a 5 nm titanium (Ti) adhesion layer and the 50 nm gold for the electrode's fabrication (Pfeiffer PLS 570, Pfeiffer Vacuum, Asslar, Germany). The feedlines and the 20 patterned electrodes were defined via standard photolithography using the Mask aligner (MA4, Süss MicroTec). Afterwards, a wet chemical etching procedure was performed to remove the excess of gold using gold etchant (TechniEtch ACl2, Microchemicals, Ulm, Germany), followed by wet chemical etching also to remove the extra Ti, using titanium etchant (TechniEtch TC, Ulm, Germany). The photoresist layer was then removed by immersing the

PET substrate with the patterned electrodes in acetone for 10 min, followed by isopropanol and DI-water rinsing.

To fabricate the passivation layer with Parylene-C, the polymer tape ELEP HOLDER BT-150E (Nitto, Japan) was used to fabricate the stencil utilizing a laser cutting machine (Glowforge basic, Seattle, USA). Then the stencil was adhered to the PET substrate with the patterned electrodes. Afterwards, the deposition of Parylene-C was performed by low-pressure chemical vapor deposition (LPCVD) with the next parameters: Vacuum PLA1 20, SP 25, and Vaporizor PhA1 160 (SCS Labcoater (PDS 2010), KISCO, Indianapolis, USA). Finally, the stencil was peeled off carefully from the PET substrate (Figure 3.2b). The obtained flexible polymer chips had a size of 10.5 mm × 21.5 mm, with 20 individually addressable electrodes.

For final cleaning before usage, the new flex-MEA chips were immersed in acetone, and isopropanol for 5 minutes each, followed by Milli-Q water rinsing and drying with a nitrogen flow. The chemically cleaned electrodes were connected to a printed circuit board (PCB, Würth Electronic GmbH & Co. KG) with a zero-insertion force (ZIF) connector that allowed the enlace to the potentiostat (Figure 3.3). The electrochemical cleaning of the flex-MEA chip was performed by CV with a multichannel CHI1030B potentiostat (Austin, USA) in 0.1 M NaOH and subsequently scanning in 0.05 M H_2SO_4. The electrochemical surface area (ESA) was determined by CV in 0.05 M H_2SO_4. A detailed description of the electrochemical procedures is described in section 3.4.3.

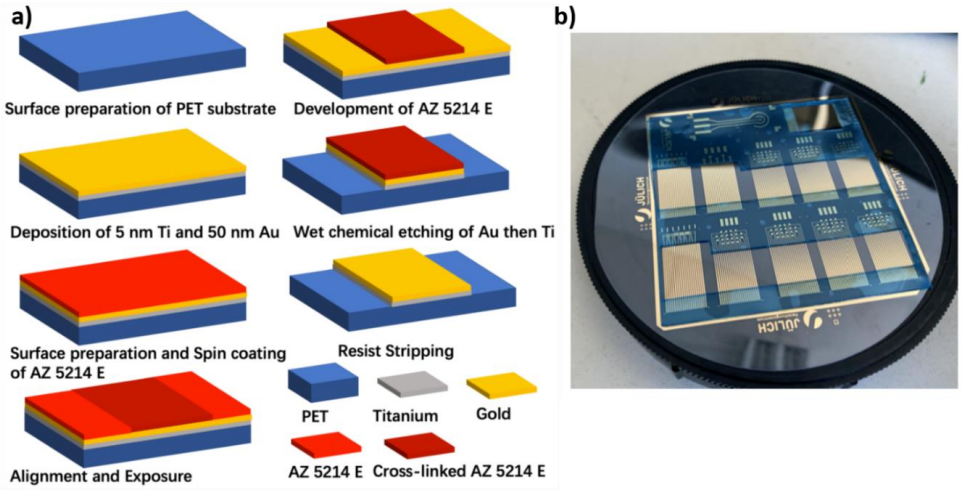

Figure 3.2 a) flex-MEA fabrication and b) stencil passivation with Parylene-C. (Extracted from Song Chen Master's Thesis).

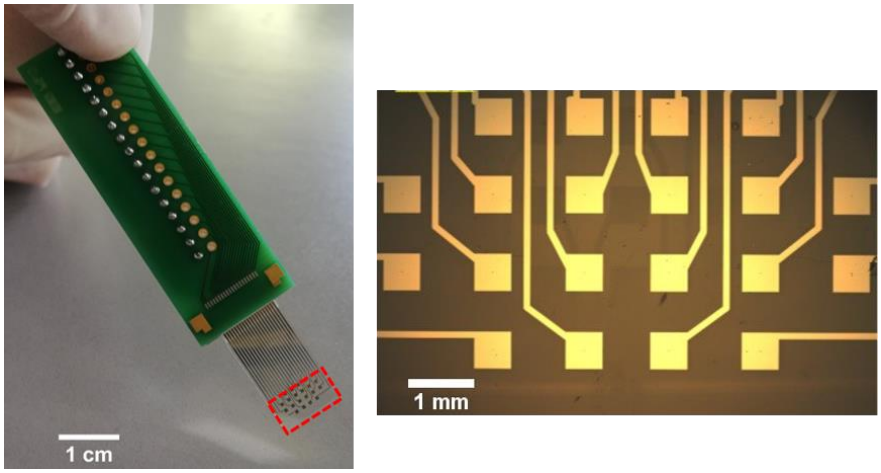

Figure 3.3 Flex-MEA electrode connected to a printed circuit board (PCB) carrier with a zero-insertion force (ZIF) connector (left). Light microscopy image of the 20 electrodes (right)

3.2.3 Preparation of GO flakes and fabrication of rGO-FET devices

The rGO-FETs were obtained as part of a collaboration with the group of Prof. Dr. S. Ingebrandt from IWE1, RWTH Aachen University. High-quality GO solution was produced from graphite powder (43209 Graphite flake, Alfa Aesar, Thermo Fisher GmbH, Germany) by implementing an optimized and low-temperature exfoliation and desalination (LTEDS) previously reported protocol [50]. Briefly, the graphite powder was oxidized and exfoliated in a reflux condenser with a mixture of H_2SO_4, H_3PO_4, and $KMnO_4$, followed by sedimentation, several low-speed centrifugations, and dialysis steps. Those steps are needed to eliminate resulting ionic products (Mn^{2+}, SO_4^{2-}, PO_4^{3-} and K^+) from the use of oxidants out of the dispersion. The final resulting graphene oxide solution was evacuated for two days inside a desiccator to dry it. The lateral sizes of the resulting flakes ranged from 300 nm to 20 µm. The dispersion was centrifuged again to obtain lateral mono-and multi-layer GO flakes until a final pH value of 2.9 was reached. The resulting GO material was water-soluble and could be applied in the next steps as a spin-coating solution to form ultra-thin GO films.

A Si/SiO_2 wafer, with previously photolithography, fabricated gold interdigitated electrodes (IDEs) was used for further processing (Figure 3.4). The characteristics of the IDEs were 5 µm width, 100 µm length, and 5 µm distance between electrodes, with a gold layer thickness of 750 nm and a 45 nm Ti adhesion layer. The 4 in. wafer was first amino-silanized in a well-controlled, gas-phase silanization procedure. GO thin films were then realized by standard spin-coating resulting in highly homogeneous, covalently bound layers of thicknesses 3–7 nm.

The reduction via intense thermal annealing at 720 °C for 4 s was performed to obtain the final conductive rGO-FET devices. This intense thermal annealing was carried out to reduce most of the graphene oxide back to graphene to permit the pyrene-modified aptamer's immobilization by pi-pi stacking. Overall, the 4-inch wafer design included 130 chips with a size of 7x7 mm^2. The rGO-FETs, with 10 IDE, have an effective gate width of $W = 900$ µm and a gate length of $L = 5$ µm (Figure 3.5a). Finally, the rGO chips were wire bonded onto specially designed printed circuit boards (PCB) and integrated with a PDMS open reservoir on top (Figure 3.5b). The rGO-FET chips were always cleaned, previous to aptamer immobilization, with acetone, followed by isopropanol and Milli-Q water rinsing. Finally, they were dried using nitrogen flow.

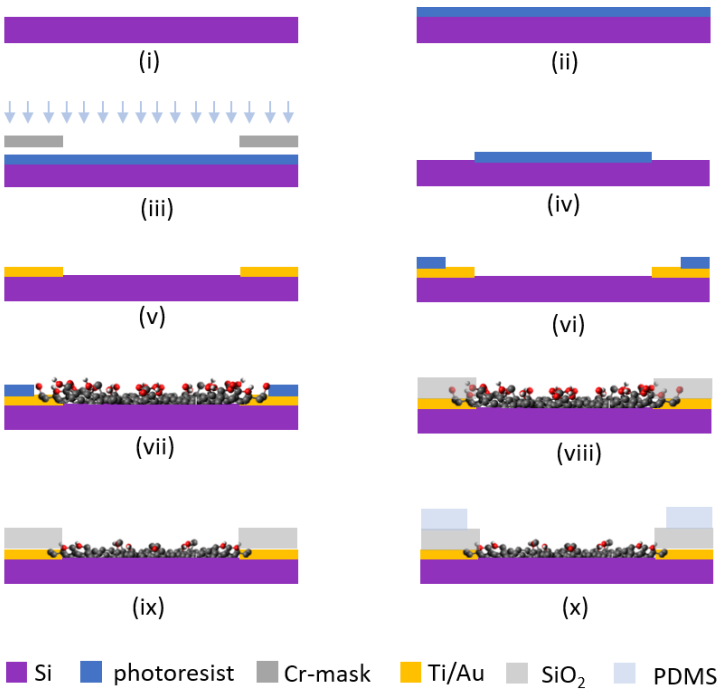

Figure 3.4 Fabrication procedure of the gold IDE for the rGO-FET devices [127].

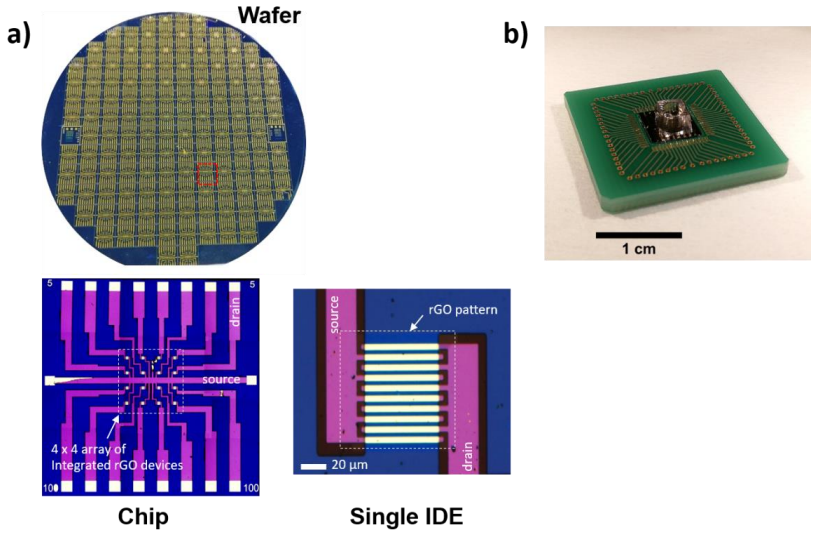

Figure 3.5 rGO-FET devices. a) Image showing the 4-inch wafer from which one of the single chips is shown with a closeup into 1 out of the 16 IDE electrodes. b) Picture of one rGO-FET chip connected to a PCB carrier and with its PDMS open reservoir.

3.3 Aptasensor biofunctionalization and target detection

3.3.1 Stepwise preparation of the aptamer/PEG receptor layer for GRE and flex-MEA

The aptamers concentrations were determined by measuring the absorbance at 260 nm with the UV/Vis/NIR spectrometer Lambda 900 (Perkin Elmer, USA). The ssDNA aptamers' optimized used concentrations were 0.5 µM for 2008s, pL1, and 2106s, and 0.03 µM for LDHp11. The thiol-terminated aptamers were always treated with 10 mM TCEP for 1 h at room temperature to reduce the disulfide-protecting bond before incubation, enabling the direct binding of the terminal thiol group of the aptamer to the gold surface. After the pre-treatment, the aptamers were diluted in 10 mM high salt concentration PBS buffer to a final volume of 250 µL. Then, the cleaned GRE and the flex-MEA, this last partially cut in four parallel stripe-like sections (Figure 3.6), were incubated overnight in the dark with each respective aptamer solution. Afterwards, the aptamer-modified electrodes were rinsed with Tris buffer and consecutively with Milli-Q water to remove unspecifically adsorbed aptamer molecules. Subsequently, the gold electrodes were incubated with an aqueous solution containing 5 mg/mL PEG during the indicated time. Last, a rinsing step with Tris buffer was performed to remove excess unspecifically adsorbed PEG blocking molecules.

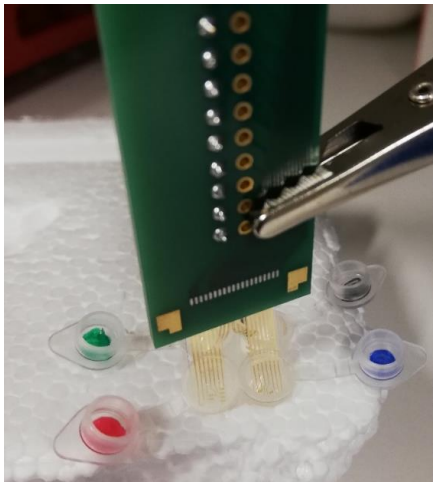

Figure 3.6 flex-MEA inserted in the different aptamer solutions: LDHp11 aptamer (Red), 2008s aptamer (green), pL1 aptamer (black) and 2106s aptamer (blue) for the multi-target aptasensor fabrication.

Once the aptasensors were ready, the different target proteins (PfLDH, PvLDH, and HRP-2) were detected by spiking them in the corresponding buffer or the biological sample. Similarly, the BSA, HSA, and hLDHB control proteins used for the selectivity test were investigated.

3.3.2 *In situ* and *ex situ* PfLDH detections in human serum by fabricated aptasensor on gold rod electrode

The impedance measurements were performed 45 min after addition of the respective concentration of protein (7.14 µM stock solution) in 1 mL volume of 1:1 ratio human serum to 25 mM Tris-HCl buffer solution at 7.5 pH containing 5 mM $[Fe(CN)_6]^{3-/4-}$ for *in situ* measurements. For *ex situ* measurements, the sensor was incubated for 45 min in whole human serum with the correspondingly added protein, posteriorly rinsed with buffer, and measured in a protein-free 5 mM $[Fe(CN)_6]^{3-/4-}$ solution of 25 mM Tris-HCl buffer.

3.3.3 flex-MEA multi-target aptasensor detection in spiked analyte blood samples and *Plasmodium falciparum* parasitized blood samples

The detection of the spiked target proteins, PfLDH, and HRP-2, was performed by immersing the flex-MEA aptasensor in 2 mL 1:100 diluted blood samples in 25 mM Tris buffer with the respective protein concentration (1 fM to 100 nM) for 45 min. Then, the sensor was rinsed and

subsequently immersed in 5 mM $[Fe(CN)_6]^{3-/4-}$ in Tris buffer solution to record differential pulse voltammetry (DPV) curves.

In the case of the parasitized blood samples, the frozen samples were thawed at room temperature and mixed 1:1 with lysis buffer. After 15 min incubation with the buffer, the resulting lysed parasitized blood was diluted 1:100 in Tris buffer. The multi-target aptasensor detection was performed in the same way as previously described by DPV measurements of spiked blood. For details of the DPV measurements, see section 3.4.2.

3.3.4 Biofunctionalization of rGO-FETs with aptamer receptor layer and PfLDH detection in buffer and human serum, and control experiments with human LDH and PSA aptamer

The pyrene-modified 2008s aptamer concentration was determined by measuring the absorbance at 260 nm with the UV/Vis/NIR spectrometer Lambda 900 (Perkin Elmer, USA). A concentration of 1 µM aptamer was used in all the experiments for the immobilization. The 2008s aptamer was diluted in 10 mM high salt concentration PBS buffer to a final volume of 30 µL that was added on the chip and incubated at 4 °C overnight. Afterwards, the aptamer-modified electrode was rinsed with 10 mM PBS buffer to remove excess aptamer molecules non-immobilized by pi-pi stacking. Different PfLDH protein concentrations (1 fM – 100 nM) in 10 mM PBS (115 mM ionic strength) solutions were incubated with the rGO-FET aptasensor for their detection. The PfLDH detection was also proved in a complex matrix such as human serum (HS). For that purpose, the measurements were carried out in 10 % HS with the spiked PfLDH concentrations of 10 fM, 10 pM, 10 nM, and 100 nM. The found concentration was determined from the calibration curve, and the percentage of recovery was calculated.

The control experiments were performed in two ways. On the one hand, the selectivity of the 2008s aptamer was proved versus human LDH B (hLDHB) at low (100 fM), medium (10 pM), and high (10 nM) concentration of protein. On the other hand, a second control experiment was carried out by replacing the 2008s aptamer for the prostate-specific antigen (PSA) aptamer to test the non-selective detection of PfLDH protein at 100 fM, 10 pM, 10 nM, and 100 nM. For this experiment, the aptamer immobilization and measurements were performed in the same way as for the 2008s aptamer. The concentration of PSA aptamer used was also 1 µM.

3.4 Electrochemical measurements

3.4.1 Electrochemical impedance spectroscopy

Electrochemical impedance spectroscopy (EIS) measurements were performed with an Autolab potentiostat/galvanostat PGSTAT302 (Figure 3.7a, Eco Chemie, Netherlands) consisting of a three-electrode system. Therefore, a platinum wire was utilized as the counter electrode (CE), an Ag/AgCl electrode (DriRef2, WPI, Germany) as the reference electrode (RE), and the GRE with the immobilized aptamer/PEG mixed monolayer as the working electrode (WE) (Figure 3.7b). All potentials in this work are noted with respect to a saturated Ag/AgCl reference electrode. The EIS measurements were recorded in 5 mM $[Fe(CN)_6]^{3-/4-}$ in 25 mM Tris-HCl buffer solution, at an applied bias potential to the electrode of 0.22 V, superimposed by an alternating voltage in a frequency range from 10 kHz to 1 Hz with an amplitude of 0.01 V. The NOVA 2.1 software was used for fitting EIS data according to the electrical equivalent circuit in order to obtain the fit-component parameter values.

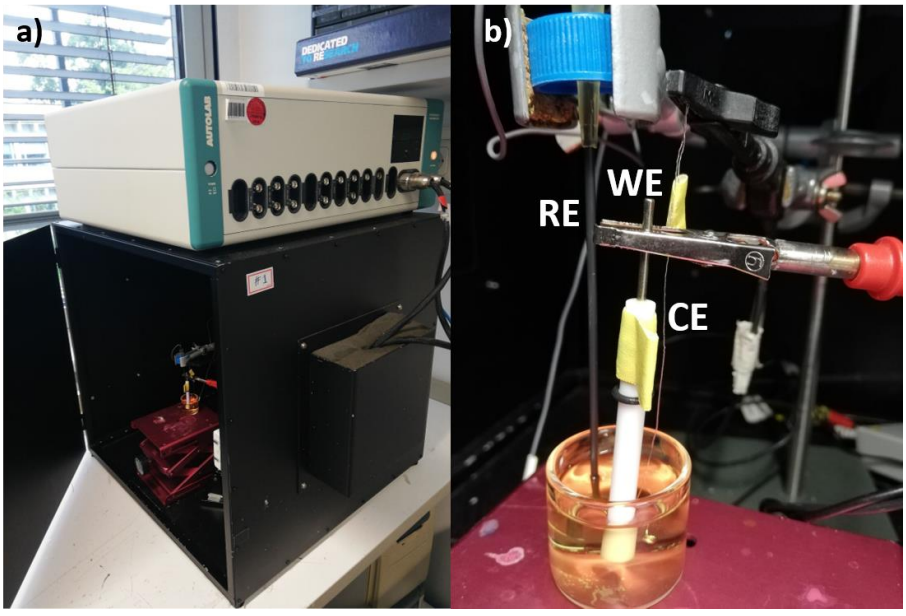

Figure 3.7 a) Autolab potentiostat with b) gold rod electrode (GRE) connected as working electrode (WE), the platinum wire as counter electrode (CE), and the Ag/AgCl electrode as reference electrode (RE).

3.4.2 Differential pulse voltammetry

The differential pulse voltammetry (DPV) measurements were carried out with a multichannel CHI1030B potentiostat (Figure 3.8a, Austin, USA) with a similar three-electrode system, as previously described in section 3.4.1. In this case, the flex-MEA multi-target aptasensor served as the working electrode (WE) (Figure 3.8b). DPV measurements were carried out at a potential window ranging from 0 to 0.7 V with a step potential of 0.005 V, modulation amplitude 0.025 V, equilibration time of 2 s, pulse width 0.05 s, and sampling width 0.025 s in 5 mM $[Fe(CN)_6]^{3-/4-}$ in 25 mM Tris-HCl buffer solution. The peak current change and statistical analysis were performed using the Origin Lab 2020 software.

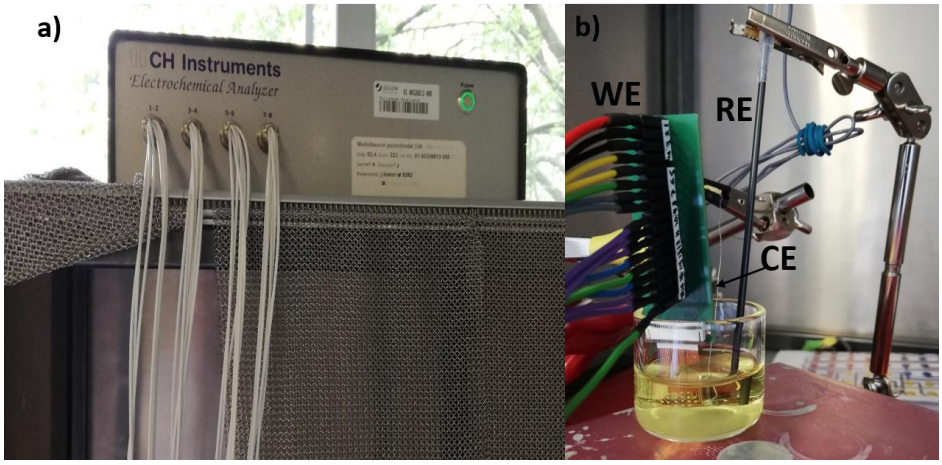

Figure 3.8 a) CHI potentiostat with its 8 single addressable sensing channels. b) flex-MEA chip connected as working electrode (WE), the platinum wire as counter electrode (CE), and the Ag/AgCl electrode as reference electrode (RE).

3.4.3 Cyclic voltammetry

Cyclic voltammetry (CV) measurements were conducted using or the Autolab potentiostat previously described for the GRE electrode or the multichannel CHI potentiostat for the flex-MEA electrode with the three-electrode system. CV for electrochemical cleaning was carried out in 0.1 M NaOH with voltage sweeps from −1.35 V to −0.35 V, at a scan rate of 2 V/s with 500 scans for GRE, and 10 scans for flex-MEA. The last cleaning step, to obtain the final clean and activated gold surface, consisted of CV in 0.05 M H_2SO_4 with voltage sweeps from 0 V to 1.5 V, at a scan rate of 1 V/s with 100 scans for GRE and 20 scans for flex-MEA. The electrochemical surface area (ESA) of the electrode was determined by running a CV cycle in a new 0.05 M H_2SO_4 solution from 0 V to 1.5 V at a scan rate of 0.1 V/s [132]. The obtained

ESA from the CV of the gold surface is based on the principle that by cycling the potential in 0.05 M H_2SO_4, the oxidation of gold is achieved (forward scan) followed by its reduction (backward scan). The charge transmitted over the interface during the reduction is proportional to the reduction peak amplitude allowing the estimation of the electrochemical surface area (Figure 3.9), which can be calculated with the following formula [128]:

$$ESA = \frac{Intensity\ of\ Reduction\ Peak}{Scan\ Rate \times Amount\ of\ the\ charge\ needed\ to\ reduce\ layer\ (386\ \mu C/cm^2)} \quad (3.1)$$

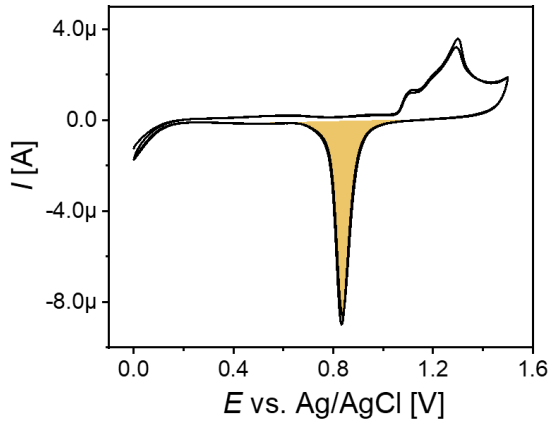

Figure 3.9 Cyclic voltammogram of the gold oxidation and its reduction (yellow peak) in 0.05 M H_2SO_4 solution to calculate the electrochemical surface area for each gold electrode.

3.4.4 Chronocoulometry for receptor density calculation

The surface aptamer density was quantified using a chronocoulometric (CC) technique measured with a CHI1030B potentiostat (Austin, USA) (see section 2.3.4.3). The measurement was performed according to a previously reported protocol [105]. First, 3 mL of 10 mM Tris buffer was added into a glass cell and purged with nitrogen for 10 min. Then, the aptamer/PEG modified gold electrode was immersed in the purged solution, and the CC measurement was conducted to obtain the double-layer charge (Q_{dl}), with the settings: initial potential of 0.2 V and final potential of −0.5 V, two number of steps, pulse width of 0.25 s, sample interval of 0.002 s, and sensitivity of 1×10^{-5} A/V. Posteriorly, 15 µL of 10 mM $[Ru(NH_3)_6]^{3+}$ solution were added into the nitrogen-purged buffer. Then, the CC measurement was again performed to obtain the total charge (Q_{total}), which comprises both Faradaic (redox) and non-Faradaic (capacitive) charges (Figure 3.10).

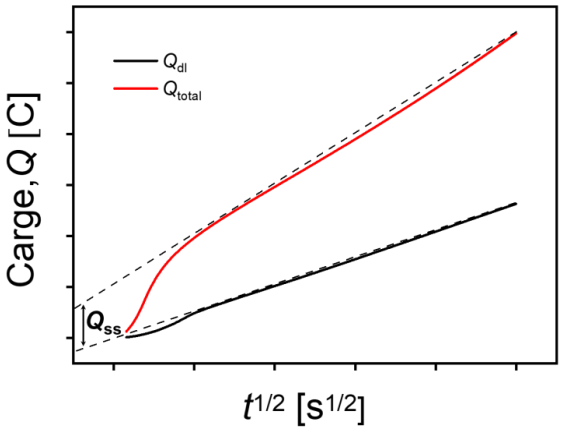

Figure 3.10 Surface aptamer density calculation by chronocoulometric technique. Q_{dl}: double-layer charge; Q_{total}: total charge from Faradaic and non-Faradaic processes; Q_{ss}: surface-confined ssDNA.

Then, the charge corresponding to RuHex electrostatically bound to surface-confined ssDNA (Q_{ss}) was obtained as $Q_{ss} = Q_{total} - Q_{dl}$. Finally, the aptamer modified surface density (Γ_{ss}) was calculated with the following formula:

$$\Gamma_{ss} = \left(\frac{Q_{ss}\mathrm{N_A}}{nFA}\right)\left(\frac{z}{m}\right) \tag{3.2}$$

where n is the number of electrons in the reaction, A is the area of the working electrode, m is the number of nucleotides in the aptamer sequence, z is the charge of the redox molecules, $\mathrm{N_A}$ is Avogadro's constant, and F the Faraday constant.

3.5 Field-effect behavior measurements of rGO-FET aptasensor

The characterization of the rGO-FET chips and the field-effect aptasensing detection measurements were carried out on a Keithley semiconductor parameter analyzer model 4200 SCS and a 590 CV analyzer. One common terminal of the gold IDEs with five-finger electrodes was connected as *source* (S), and the second terminal with the same number of finger electrodes worked as *drain* (D), an Ag/AgCl reference electrode (DriRef2, WPI Germany) served as a *gate* (G) electrode (Figure 3.11).

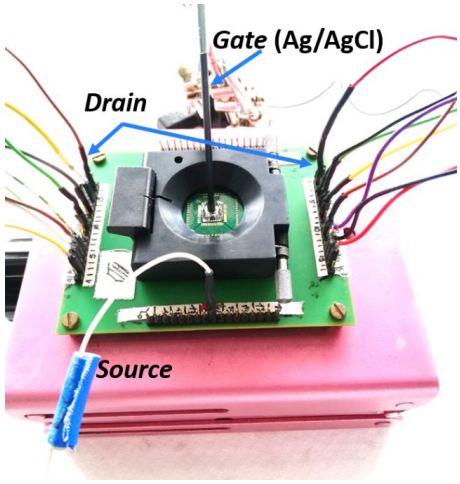

Figure 3.11 rGO-FET device connected to probe-station by a common *source* (S) and individually addressable *drain* (D) connections with an Ag/AgCl reference electrode as *gate* (G) electrode.

For the field-effect measurements, a bias voltage potential (V_D) between S and D connection of 0.1 V, with a sweep G voltage (V_G) of ±0.7 V was applied. For the time-transient measurements, a constant V_D of 0.1 V and V_G of −0.4 V were held during a measuring period of 2000 s.

3.6 Physicochemical characterization methods

3.6.1 QCM-D measurements

The Quartz Crystal Microbalance with Dissipation monitoring (QCM-D) equipped with a fluidic system from Q-sense Biolin Scientific (Västra Frölunda, Schweden) was used to analyze the mass change and the associated viscoelastic properties of the system for various immobilization steps including receptor, backfill molecule, and analyte (see section 2.5.1). First, the QCM-D components and gold sensors were cleaned according to recommendations from the supplier. The gold QCM chips used for the thiol-terminated aptamer immobilization were cleaned in an oxygen plasma oven for 3 min at 50% power and 0.5 mbar. Later, they were left in ethanol for 30 min to reduce the formed gold oxide to metallic Au. Once everything was cleaned and ready, the cell was assembled, and the corresponding sensor was placed on the module (Figure 3.12).

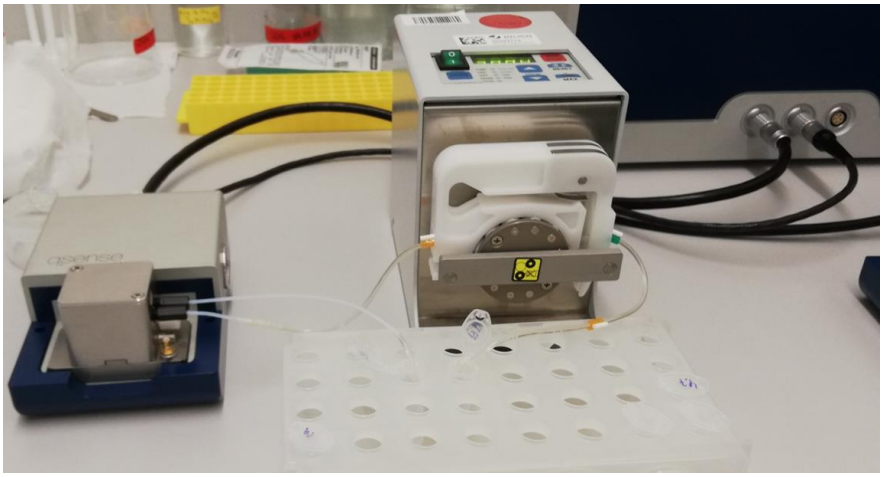

Figure 3.12 QCM-D flow system (left), with the peristaltic pump used to control the flow of solution molecules (right).

The buffer solution was pumped through the cell and left running until stabilization of the sensor signal was achieved (frequency shift below 0.2 Hz in 10 min). Subsequently, the experiment was started by consecutively flushing molecule solutions and rinsing with Tris buffer, when required, through the QCM-D fluidic cell. The flow rate was controlled to 20 µL/min for all the steps using a peristaltic pump (Reglo Digital ISM596, Cole-Parmer, Germany). The mass associated with the number of molecules immobilized on the surface of the electrode was calculated with the Sauerbrey equation (Equation 2.24). The viscoelastic parameters were obtained by the QSense Dfind software provided with the QCM-D system.

3.6.2 XPS analysis

The chemical sample analysis for corroboration of aptamer and PEG immobilization by X-ray photoelectron spectroscopy (XPS) was conducted with the instrument Phi5000 Versa Probe II (ULVAC-Phi Inc., USA). The monochromatic Al K-alpha line ($h\nu$ = 1.486 keV) was used as a source with the following power: 50 W at 15 kV, 200 µm spot size, 187.5 eV pass energy, 0.8 eV step, 100 ms/step.

3.6.3 Contact angle

The contact angle measurements were carried out with the instrument Dataphysics OCA 20. The contact angle pictures were analyzed with the software SCA20 provided with the instrument.

3.6.4 AFM analysis

Atomic force microscopy (AFM) imaging for aptamer/PEG monolayer investigation was performed using a Nanoscope Multimode 8 microscope (Bruker, Netherlands) equipped with a piezoelectric E-series scanner and aluminum-coated Si cantilever from Bruker (RTESPA-150) with a resonant frequency of 150 kHz and spring constant 5 N/m. The images were acquired in tapping mode with the following parameters: scan rate 1 Hz, scan size 0.5 µm, and aspect ratio 1:1. The (111) plane of a gold single crystal disk was used as a model electrode surface. The activation and cleaning of the single crystal were done by thoroughly rinsing it in ethanol, isopropanol, and Milli-Q water. After drying, the crystal was annealed for 10 min in a hydrogen flame (orange glowing) and cooled down to room temperature in an argon stream. The subsequent aptamer modification and PEG blocking were done as described in section 3.3.1.

In the case of AFM investigation for aptamer immobilization on rGO surface, the images were also acquired in tapping mode with the following parameters: scan rate 1 Hz, scan size 1 µm, and aspect ratio 1:1. One chip was analyzed before and after the aptamer immobilization and subsequently after protein detection.

Chapter 4

Polyethylene glycol time-dependent blocking modulates the performance of an electrochemical malaria aptasensor

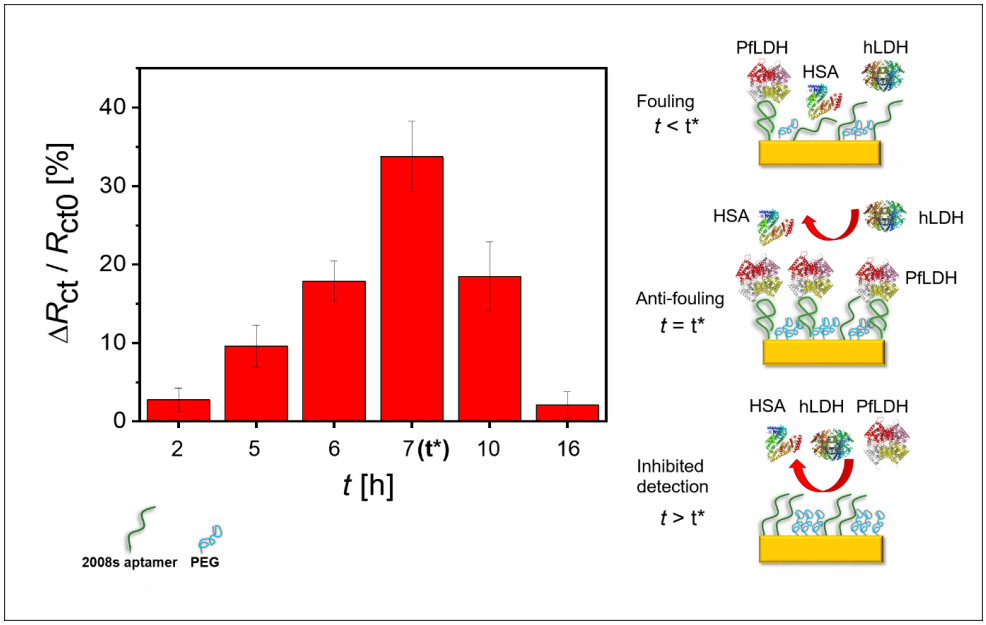

The following chapter was adapted from an article published in Bioelectrochemistry journal, entitled "Polyethylene glycol-mediated blocking and monolayer morphology of an electrochemical aptasensor for malaria biomarker detection in human serum" DOI: 10.1016/j.bioelechem.2020.107589. The chapter was reproduced with permission from Gabriela Figueroa-Miranda, Changtong Wu, Yuting Zhang, Lena Nörbel, Young Lo, Julian A. Tanner, Lothar Elling, Andreas Offenhäusser, and Dirk Mayer [24].

The detection of biomarkers by electrochemical aptamer-based biosensors in biological fluids like human serum or blood remains a challenge due to undesired unspecific adsorption of matrix species on the surface of the transducer [15,129,130]. During aptasensor characterization, measurements are performed as *ex situ* or as *in situ* detection. The so-called *ex situ* measurements are done by incubating the biosensor in fully lysed blood or human serum without the need for dilution steps since the final measurement is then conducted in a buffer medium, in this way avoiding the undesired biofouling effect [131–135]. However, problems emerge when tests are conducted in an *in situ* way. *In situ* measurements, as their name suggests, perform the detection of the analyte and the actual measurement in the same complex medium (human serum or blood). Here, the interference of serum-born components may affect the selectivity and sensitivity of the biosensor by the unspecific biofouling [29,136–138]. Much recent research has been focused on implementing biosensors as point-of-care diagnostic tools [139–144]. The point-of-care testing requires the ability to detect the biomarker directly in the biological fluid, which demands the implementation of *in situ* detection.

Consequently, biosensors have been modified with blocking molecules to reduce such interfering biofouling. However, the effectiveness relies on the chemical composition and morphology of the blocking film. Numerous antifouling compounds have been proposed, such as zwitterionic molecules [145], peptides [146], alkanethiols [147,148], and polyethylene glycols [149]. They can generally be classified into hydrophobic and hydrophilic materials. Hydrophobicity can be beneficial for suppressing cell adhesion and increasing the charge transfer resistance during impedimetric sensing. 1-undecanethiol (UDT) is a commonly used hydrophobic blocking substance, which, however, shows unspecific interaction to hydrophobic domains of proteins [148,150]. 6-mercapto-1-hexanol (MCH) is less hydrophobic but is also widely employed as a blocking molecule due to its short length, which leaves aptamer/target interactions unaltered [29,125,148,151]. However, testing in biological fluids such as human serum often challenges the blocking capability of MCH [15,29]. Among hydrophilic materials, polyethylene glycol (PEG) has been widely used in biomedical devices as an antifouling coating since it possesses low interfacial energy in an aqueous medium. Thus, proteins or cells closer to this material face thermodynamically unfavorable interactions that lead to their repulsion [30–32]. Owing to these antifouling properties, PEG has gained attention as a blocking molecule for biosensors [33–39,41–44,152].

An aptamer-based electrochemical biosensor for the detection of *Plasmodium falciparum* LDH, main malaria biomarker, by using the 2008s aptamer [14] and mercapto-hexanol (MCH) as a blocking molecule was previously developed [29]. Electrochemical impedance spectroscopy (EIS) was implemented to follow the stepwise aptasensor fabrication and PfLDH detection (Figure 4.1a) (see section 2.3.3 EIS). A characteristic increment of impedance in buffer solution was observed after immobilization of molecules, except for the protein detection. At the physiological 7.5 pH of the used buffer, this protein has a positive net-charge due to its isoelectric point (pI = 8.0 for PfLDH). This positively-charged protein binds to the small negatively-charged aptamers causing a shielding effect of the aptamer backbone. Thus, the positive protein electrostatically attracts the used negatively charged redox probes from the solution phase and allows them to reach the surface of the electrode, causing in this way the observed decrement of the impedance measurement (Figure 4.1b and Appendix B, S1). However, challenges for this aptasensor were faced when trying to detect PfLDH directly in full or highly concentrated biological fluids. In this section, the implementation of polyethylene glycol (PEG) as blocking film is reported to suppress unspecific binding from human serum by optimized immobilization conditions on the electrochemical malaria aptasensor.

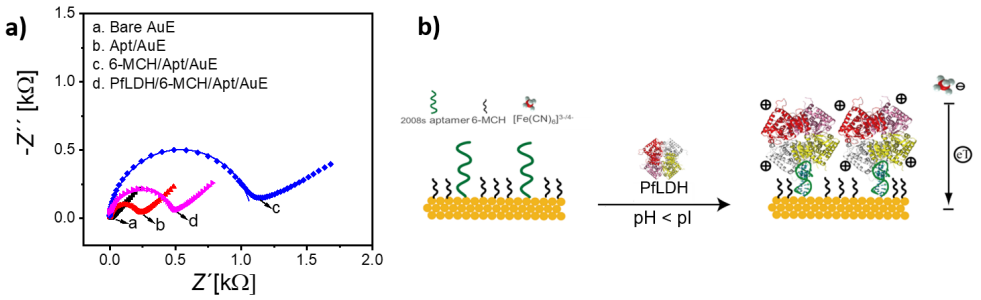

Figure 4.1 a) EIS measurements of step-by-step aptasensor preparation and PfLDH detection in 5 mM $[Fe(CN)_6]^{3-/4-}$ solution at pH 7.5: (a) bare gold electrode (BareAuE), (b) 2008s aptamer immobilized step (Apt/AuE), (c) 6-mercapto-1-hexanol-treated step (6-MCH/Apt/AuE) and (d) 1 nM PfLDH binding step (PfLDH/6-MCH/Apt/AuE). The symbol corresponds to the experimental measurements and solid line to the fit data. b) Schematic representation of positively-charged PfLDH detection at physiological pH (7.5) with the attraction of the negatively charged redox probes ($[Fe(CN)_6]^{3-/4-}$. Adapted from [29].

A detailed study of the variation of the chemical and morphological composition of the aptamer/polyethylene glycol mixed monolayer as a function of incubation time was conducted by quartz crystal microbalance with dissipation, X-ray photoelectron spectroscopy, contact

angle, and atomic force microscopy. The comparison of the electrochemical aptasensor detection performance by using MCH or PEG as a blocking coating was also discussed.

4.1 Reduction of non-specific adsorption

In a previous study [29], noticeable non-specific binding of PfLDH in human serum on a receptor-free gold surface covered only with MCH blocking molecules was observed, which caused an appreciated semicircular impedance increment of 33.9±2.4 % in the Nyquist plot representation (Fig. 4.2a). In contrast, a distinctly smaller non-specific binding corresponding to only 8.8±1.2 % impedance change was observed in this study for a PEG-modified (2 kDa) receptor-free sensor surface after exposure to 50 nM PfLDH in human serum (Fig. 4.2b). A shorter PEG molecule (400 Da) was also tested for PfLDH detection in human serum. However, a lower antifouling capability was observed compared to the longer PEG (2 kDa) blocking molecule (See appendix B, Figure S2). The mechanism behind the protein repulsion by PEG has been reported to be a consequence of the low gain of adhesion enthalpy and the associated loss of entropy due to steric repulsion during the interaction process. That means that the steric repulsion is related to restrictions of configurational freedom and concomitant desolvation of PEG when the protein tries to attach to the surface, making it a thermodynamically unfavorable interaction [30,31,153,154]. Noteworthy, also recent publications have demonstrated PEG antifouling capabilities for aptamer/PEGylated surfaces in complex matrices like serum or blood [41,44,155]. However, systematic studies on the correlation of ssDNA aptamer/PEG-film composition and antifouling properties for enhanced target detection have not been reported so far. Zhang *et al.* reported that an increase in the concentration of a zwitterion-bifunctionalized poly (ethylene glycol) decreases the signal of the ATP analyte [44]. What remains unknown so far is how the signal changes for low and high PEG surface density, how the morphology of the mixed aptamer/PEG monolayer alters for different incubation times of thiolated PEG molecules, and how these changes influence the sensor performance.

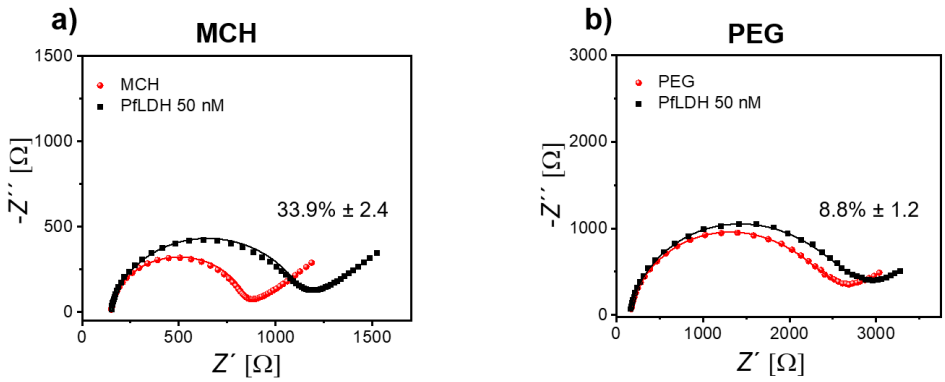

Figure 4.2 EIS Nyquist plots of Au electrodes demonstrating the non-specific adsorption on a receptor-free surface covered with a) MCH and b) PEG tested with 50 nM PfLDH in human serum.

4.2 Physicochemical characterization of the stepwise aptasensor fabrication with different PEG blocking times

4.2.1 Monitoring stepwise molecule adsorption by QCM-D

Firstly, the stepwise immobilization of aptamer, PEG, and PfLDH detection was monitored by Quartz Crystal Microbalance with Dissipation (QCM-D). This method facilitated the determination of changes in mass and the viscoelastic properties of the mixed receptor layer during its assembling (see section 2.5.1).

After the cleaning preparation of the gold (Au) sensor and QCM-D components, described in section 3.6.1, the flow of 0.5 µM of aptamer solution and subsequent Tris rinsing caused a decrement in the frequency (Δf = 21.1 Hz) associated with the immobilization of the aptamer receptor on the sensor (Fig. 4.3a, and b). The corresponding calculated mass was 2.50 ng/mm^2 corroborating the aptamer film formation [156]. The increase in the dissipation (ΔD = 1.55 ppm) is correlated with the soft and elastic nature of ssDNA aptamers and corroborated by elastic modulus (E) and viscosity (μ) reported in the literature (Table 4.1) [157,158]. After the addition of PEG blocking molecules (7 h incubation) and rinsing with Tris buffer, a further frequency shift of 2.9 Hz was observed due to the binding of these molecules to the aptamer-free electrode spaces (Fig. 4.3c). The associated mass change was 0.16 ng/mm^2. The relatively small change of the frequency after PEG addition compared to aptamer incubation indicates that aptamer receptors already occupied the majority of the sensor surface.

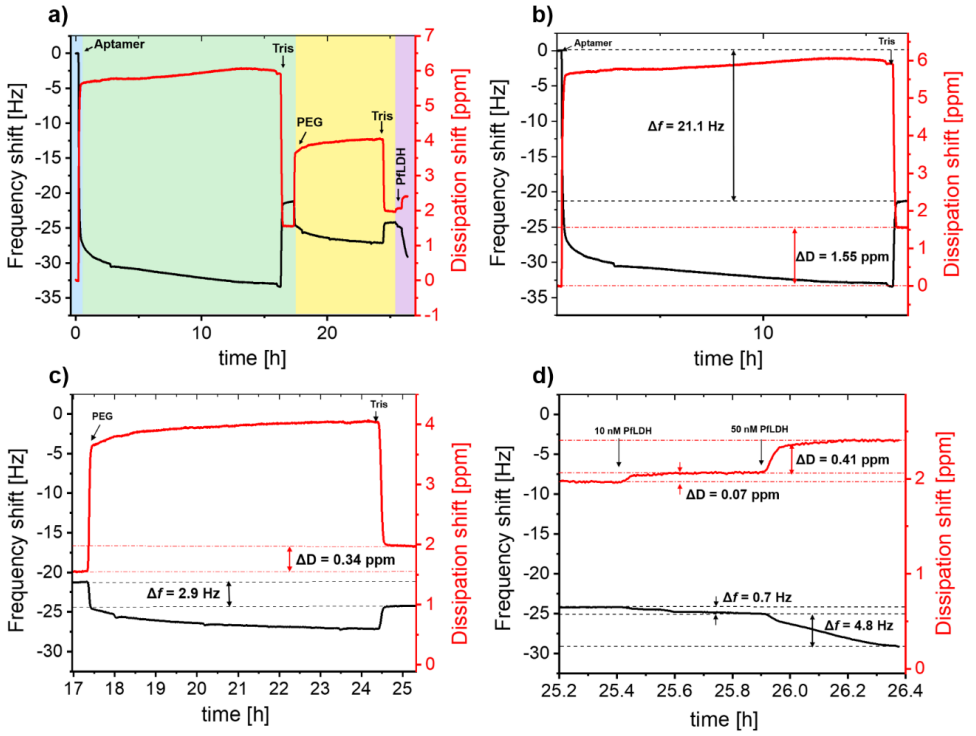

Figure 4.3 a) Complete QCM-D plot for aptamer and PEG immobilization and PfLDH detection. Frequency shift (Δf) and dissipation shift (ΔD) after b) aptamer immobilization, c) PEG blocking, and d) 10 and 50 nM PfLDH detection, respectively.

The dissipation increase (0.34 ppm) is correlated to the soft and hydrated nature of the PEG in agreement with previously reported values for elastic modulus and viscosity [159,160]. Further frequency changes of Δf = 0.7 Hz (0.12 ng/mm^2) and 4.8 Hz (0.84 ng/mm^2) were registered after the addition of 10 nM and 50 nM of PfLDH, respectively, as well as a slight dissipation change of ΔD = 0.07 and 0.41 ppm, which are assigned to the protein binding via aptamer receptors (Fig. 4.3d). The small mass change associated with the protein detection might be related to the fact that the proteins are not directly bound to the electrode surface but via the aptamer, which limits the detection capabilities of this method [115]. According to the QCM-D experiments, there was no significant frequency and dissipation change for different PEG incubation times, suggesting that the PEG density did not change noticeably during extended incubation (Fig. 4.4). Also, E and μ for 2 and 16 h did not indicate any significant change for different PEG incubation times, as shown in Table 4.1.

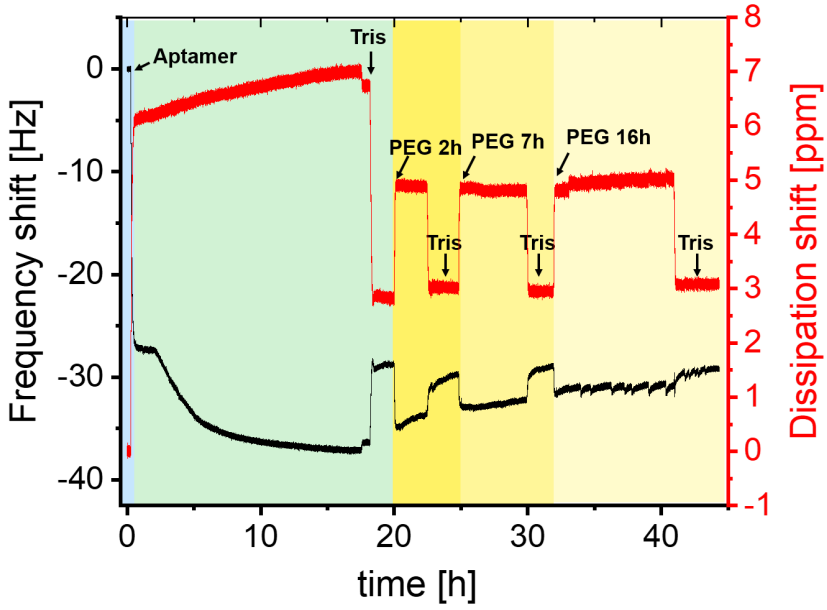

Figure 4.4 QCM-D measurement for aptamer immobilization and PEG blocking at different times. Practically no change in frequency (Δf = 0.92, 0.94 and 0.92 Hz) and dissipation (ΔD = 0.13, 0.15 and 0.15 ppm) were observed for the different incubation times of PEG at 2, 7, and 16 h, respectively.

The high thicknesses obtained by this method might be associated with the hydration of the molecules contrary to AFM measurements, which were done at ambient conditions. However, a minor increment of the thickness after 16 h incubation of PEG was also corroborated as observed for AFM (Fig 4.7i).

Table 4.1 QCM-D viscoelastic parameters for different PEG incubation times.

	Thickness (nm)	**Elastic modulus (kPa)**	**Viscosity (mPa s)**
2008s aptamer	4.05 ± 0.61	5.40 ± 0.50	1.30 ± 0.04
PEG 2 h	5.38 ± 0.15	5.15 ± 1.10	1.30 ± 0.02
PEG 7 h	5.32 ± 0.10	5.80 ± 1.20	1.30 ± 0.02
PEG 16 h	5.45 ± 0.22	5.25 ± 0.30	1.20 ± 0.05

4.2.2 XPS investigations

The chemical composition of the bare gold electrode, the electrode after modification with aptamer, and the complete aptamer/PEG receptor layer were investigated by x-ray photoelectron spectroscopy (XPS). Fig. 4.5 depicts the survey spectra of the different samples, which are mainly dominated by the peaks of the Au substrate. Compared with the bare gold (blue spectrum), a decrement of the gold signal (Au 4f) was observed after aptamer and PEG adsorption due to the formation of a mixed SAM on top of Au. An increment of the carbon (C 1s) content, the appearance of oxygen (O 1s), nitrogen (N 1s), and phosphorus (P 2p) peaks confirmed the aptamer immobilization since those are the main elements of ssDNA (red spectrum). Further increments of carbon and oxygen were observed together with a decrease of Au 4f, and N 1s after the long-chain PEG (2 kDa) was immobilized. The sulfur (S 2p) peak was caused by the thiol-terminal group that anchors aptamer and PEG to the gold surface [154,161]. The height of this peak was relatively small since each molecule possesses one sulfur atom, which was buried by the entire chain of the molecule.

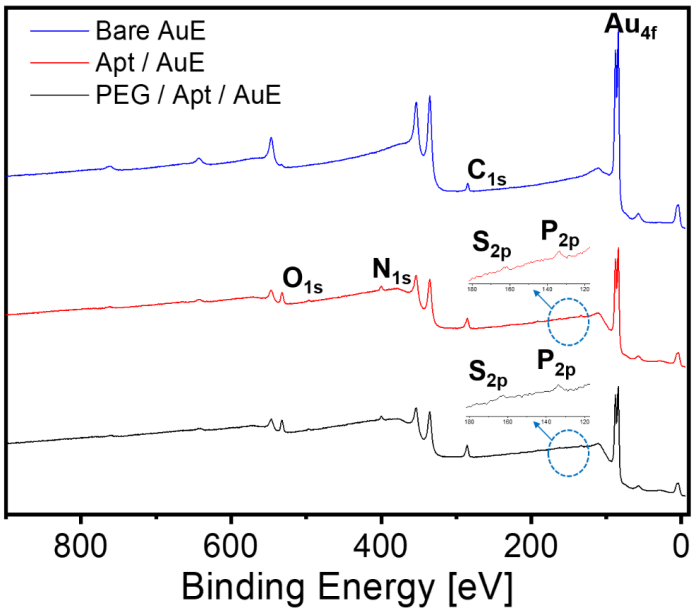

Figure 4.5 XPS analysis of a bare gold chip (blue line), gold chip modified with aptamer (red line), and aptamer/PEG-modified gold chip (black line). Gold (Au 4f) and traces of carbon (C 1s) photoelectron peaks at 84 and 285 eV, respectively, for a bare gold electrode (Bare AuE). After immobilization of aptamer/ and PEG, the appearance of the oxygen (O 1s, 533 eV), nitrogen (N 1s, 400 eV), phosphorous (P 2p, 134 eV), and sulfur (S 2p, 164 eV) peaks were evident.

The extension of the PEG immobilization time did not lead to an apparent change of the C1s or O1s signals similar to QCM-D data indicating that the coverage increase was beyond the accuracy of used measurement methods, Table 4.2.

Table 4.2 Detection of element composition of the electrode surface by XPS analysis after aptamer immobilization and PEG blocking compared with the bare gold surface. The result of the chemical composition percentage is the average of three independent measurements.

	Au 4f	C 1s	O 1s	P 2p	N 1s	S 2p
Gold	46.3±13.1	49.8 ± 7.6	--	--	--	--
Aptamer	20.3 ± 0.1	51.0 ± 4.4	17.4 ± 1.1	2.2 ± 0.4	8.0 ± 2.6	0.9 ± 0.3
PEG 2 h	17.1 ± 1.1	53.3 ± 5.1	19.9 ± 1.0	1.9 ± 0.6	6.2 ± 2.4	0.9 ± 0.2
PEG 7 h	17.1 ± 3.4	53.8 ± 6.0	19.2 ± 1.4	2.1 ± 0.5	6.4 ± 2.3	0.8 ± 0.3
PEG 16 h	16.9 ± 3.3	54.4 ± 7.3	19.8 ± 0.2	1.8 ± 0.5	5.6 ± 2.5	1.1 ± 0.2

4.2.3 Contact angle investigations

A cleaned bare gold electrode was used as a reference for comparison with other gold electrodes after PEG, aptamer, and aptamer/PEG modification. Contact angle experiments corroborated the immobilization of aptamer and PEG molecules via decreasing contact angles from 84.2° for the bare gold to 27.6° for only PEG and approximately 16.0° for aptamer alone as well as aptamer/PEG mixed monolayers. In the control case, when only PEG was immobilized, a higher contact angle was obtained as compared with aptamer samples, which agrees with values reported in the literature for PEGylated surfaces [162]. These contact angle variations indicate enhanced hydrophilicity for the surface after aptamer, PEG, and aptamer/PEG layer formation (Fig. 4.6). The high hydrophilicity of aptamer-decorated surfaces can presumably be assigned to the polyanionic character of the DNA phosphate backbone.

An analysis of the contact angle was also done for aptamer modified gold samples with different PEG immobilization times. The contact angle remained similar or slightly smaller than those of the PEG-free aptamer electrode and distinctly smaller than those of PEG/AuE, which confirms the dominating influence of the aptamer on the composition and surface energy of the mixed aptamer/PEG receptor layer (Table 4.3).

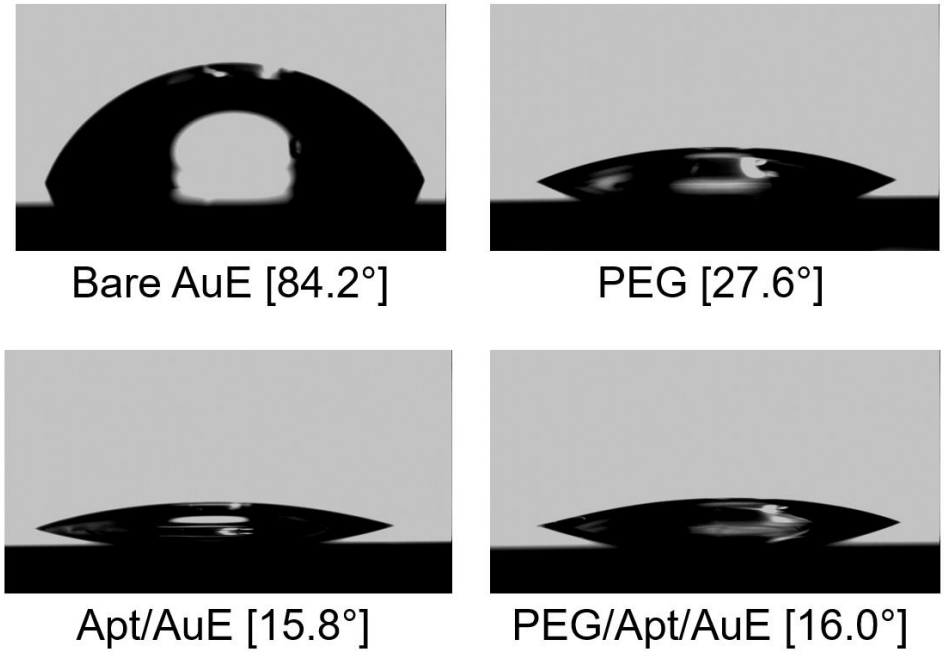

Figure 4.6 Contact angle analysis exhibited increment hydrophilicity (surface energy) after PEG, aptamer (Apt), and Apt/PEG immobilization compared with a bare gold surface (Bare AuE).

Table 4.3 Contact angle measurements at different times of PEG blocking molecule incubation.

Condition	Contact angle (°)
Bare AuE	84.2 ± 1.4
PEG 16 h	27.6 ± 1.7
Apt/AuE	15.8 ± 1.5
PEG 2 h /Apt /AuE	15.2 ± 2.5
PEG 7 h /Apt /AuE	16.0 ± 2.7
PEG 16 h /Apt /AuE	13.7 ± 1.7

4.2.4 AFM investigations

The topographical characterization of the surface morphology after aptamer immobilization and different PEG incubation times was carried out by AFM analysis. The preparation started from an atomically flat gold (111) single crystal surface, which had an RMS surface roughness of

0.07±0.01 nm (Fig 4.7a, and b). After aptamer immobilization, the overall surface roughness increased to 0.20±0.02 nm. Spherical objects were homogeneously distributed over the surface and possessed a topographical height of 0.83±0.10 nm (Fig 4.7c, and d). It can be assumed that the aptamer molecules adsorbed to the surface in islands and did not form a dense monolayer. This assumption is based on the one hand on the AFM data since a dense monolayer would result in smaller surface roughness [163]. On the other hand, the aptamer surface density was estimated by chronocoulometry (see section 3.4.4, Figure 3.10), which was $(1.29\pm0.01)\times10^{12}$ molecules/cm^2 and corresponded to a low-density coverage, according to Zhang *et al.* [105]. After the incubation of PEG for 2h, the roughness further increased to 0.32±0.03 nm with feature heights of 1.07±0.16 nm, suggesting that also these molecules bind to the gold surface (Fig. 4.7e and f). However, aptamer and blocking molecules did not form a homogeneously mixed monolayer but seemingly separated into domains, which appeared as elevated islands in the AFM images. Systematic analysis of the surface roughness, island height, and island diameter for two different aptamer concentrations showed in both cases for different PEG incubation times an increase in all, roughness, island height, and island diameter (Table 4.4 and Appendix B Figure S3).

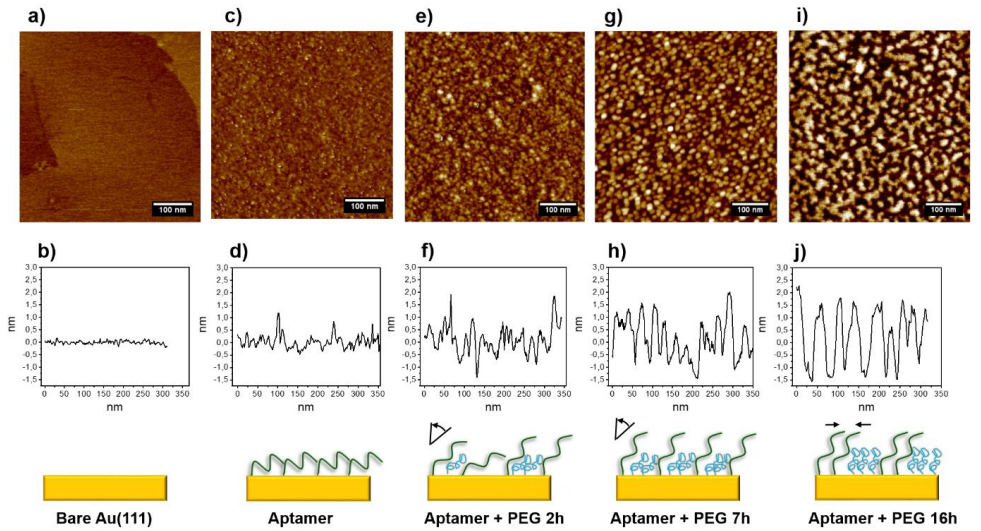

Figure 4.7 Tapping mode AFM image and line cross-section for a bare single-crystal gold (111) surface (a, b), after aptamer immobilization (c, d), and additional PEG binding for 2 h (e, f), 7 h PEG (g, h); and 16 h PEG (i, j) with aptamer concentration of 0.5 µM. The bottom schematics depict the change of the composition of the mixed aptamer/PEG receptor layer for the corresponding preparation conditions. The color scale of a) goes from -1.2 nm to 1.2 nm; the color scales from c) – i) go from -2 to 2 nm.

Noteworthy, the increase in these parameters was more significant for high aptamer densities. In particular, the number of high islands was less for 2 h PEG incubation as compared with 7 h for both aptamer densities. This, together with the increase in surface roughness, indicated that the aptamer molecules tethered to the electrode surface initially not only via thiol-gold bonds but also via weak nitrogen-gold and van der Waals interactions [83,161]. After the addition of PEG, these molecules bound to free gold areas via strong Au-thiol bonds, disrupting the weak ssDNA chain-Au interactions. Thus, pushing aptamer molecules upright that were previously lying on the surface. This event was seemingly not so significant for short PEG immobilization times (2 h) (Fig. 4.7e) but increased after 7 h and 16 h PEG incubation, which lifts ssDNA aptamers and increased the number of high islands (Fig 4.7g and i).

Table 4.4 AFM analysis of surface roughness, island height, and island diameter after aptamer immobilization and PEG blocking at 2, 7, and 16 h.

	Roughness 500nm / nm	**Island height (§m) / nm**	**Island height / nm**	**Island diameter / nm**
Bare	0.07±0.01	--	--	--
***Aptamer high**	0.29±0.03	1.15±0.23	0.98±0.80	5.7±2.0
Aptamer high/ 2h PEG	0.48±0.04	1.86±0.46	1.10±0.33	7.5±3.7
Aptamer high/ 7h PEG	0.60±0.06	2.52±0.73	1.40±0.30	10.1±3.1
Aptamer high/ 16h PEG	1.04±0.10	2.80±0.30	1.80±0.30	20.4±10.2
****Aptamer low**	0.20±0.02	0.83±0.10	--	--
Aptamer low/ 2h PEG	0.32±0.03	1.07±0.16	0.34±0.14	12.3±5.7
Aptamer low/ 7h PEG	0.43±0.04	1.76±0.36	0.80±0.30	10.6±3.1
Aptamer low/ 16h PEG	0.47±0.01	1.93±0.28	0.96±0.28	16.7±5.5

*Aptamer high refers to the concentration of 0.5 μM; **aptamer low refers to the concentration of 0.1 μM. § m: manually determined from the cross-section.

Although the PEG surface coverage did not change significantly for 7 and 16 h, as corroborated by QCM-D and XPS measurements, there was a distinct surface rearrangement

between aptamer and PEG for different incubation times. For 16 h incubation, a distinct increase in the island diameter was observed, indicating that a ripening process occurred where the aptamer islands merged to connected domains resulting in phase-separated arrangements (Fig. 4.7i). The island formation indicates that short ssDNA and PEG molecules were subjected to phase separation and instead behaved like ssDNA/alkanethiol SAM [85,164,165]. The different chain lengths connected to the respective thiol group of ssDNA and PEG might contribute to this observation.

4.3 PEG blocking time optimization

The composition of the mixed receptor layer is crucial for sensor performance. On the one hand, the aptamer receptor (here 2008s) requires a particular space on the transducer surface for 3-D conformational adaptation when binding with its target (PfLDH). On the other hand, those electrode surface areas that are not covered by aptamers should be blocked by PEG to reduce the non-specific binding of components present in human serum. Therefore, impedance measurements for the detection of PfLDH at different incubation times of PEG were conducted to identify the optimal blocking conditions (Fig 4.8). At short PEG incubation time (< 5 h), the target detection signal, which represents the change of the charge transfer resistance induced by target binding divided by initial charge transfer resistance, $\Delta R_{ct}/R_{ct0}$, was low due to the low density of the blocking molecules. The ssDNA molecules partially interacted with the Au electrode surface, which competed with the analyte binding, corroborated by AFM analysis (Fig 4.7e). The detection signal rose with increasing incubation times since ssDNA-chain/Au interactions were disrupted by PEG binding until the PfLDH signal reached its maximum at 7 hours.

Interestingly, as the incubation time increased (>8 h), a highly compact PEG monolayer was obtained, which led to a decrement of the signal by inhibiting the interaction between the aptamer and its target, also corroborated by AFM analysis (Fig 4.7i). Both high aptamer and PEG densities may contribute to his observation. As mentioned before, an aptamer requires conformational freedom to adapt to its target. If their densities are too high, the analyte binding capability vanishes. Furthermore, it has been reported that densely packed PEGylated surfaces with brush-like configuration do not effectively prevent protein adsorption. Only less packed crystalline helical amorphous forms, mushroom configuration, are resistant to adsorption of proteins. The different configurations are correlated with the incubation time.

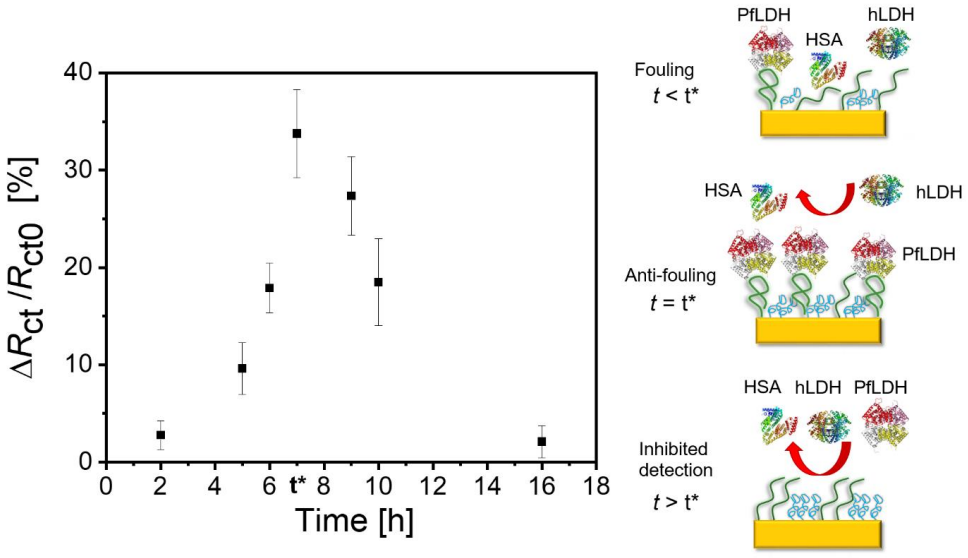

Figure 4.8 Optimization time of PEG blocking plot with schematic representation of the varying aptamer/PEG morphologies on a gold surface at different PEG incubation times for optimized PfLDH (10 nM) detection in human serum. All experiments were conducted in triplicate.

Densely packed assemblies were reported for times exceeding overnight incubation, while short incubation times (≤2 h) were not enough to immobilize PEG to avoid protein adsorption effectively [31,154,166]. The phase separation observed in the AFM study (Fig. 4.7i) was accompanied by an increase of molecule packing within its respective domain. These effects could explain the signal reduction for the impedance measurements since the phase separation, which enhances the island formation, increases the local aptamer density making them not accessible for the interaction with the target PfLDH. For the further aptasensor characterization, 7 hours were used for blocking the surface with PEG.

4.4 Concentration dependence of sensor signal

The sensitivity is doubtless an important parameter for biosensors, which should cover the entire pathologically relevant concentration range, including healthy and disease-related biomarker levels. A calibration curve was recorded to determine the lowest confidence detection value by calculating the limit of detection (LOD), the dynamic range of detection, and sensor sensitivity. The obtained equation from the logarithmic presentation of the PfLDH

concentration versus relative charge transfer resistance change for the aptamer/MCH modified sensor was $\Delta R_{ct}/R_{ct0}$ (%) = 8.3 lg$C$ + 16.0 with a correlation coefficient of 0.99. Such aptamer/MCH modified sensor showed a LOD of 1.3±0.1 pM and a dynamic detection range from 10 pM to 10 nM in 10% HS (Fig 4.9a). It is worth mentioning that only in 10% human serum it was possible to detect the target protein, in a serum concentration of 50%, or higher, no detectable signal change was observed. The sensor's sensitivity (S) can be extracted from the slope of the semi-logarithmic equation being S = 8.3 ± 0.1/decade. The obtained equation for the aptamer/PEG receptor layer was $\Delta R_{ct}/R_{ct0}$ (%) = 7.9 lg$C$ + 33.9 with a correlation coefficient of 1.00. This aptamer/PEG sensor exhibited a lower LOD of 0.8 pM and a wider dynamic concentration range that goes from 2.3 pM to 100 nM in significantly higher serum concentration (50% HS), Fig 4.9b. The Nyquist plot with the different PfLDH concentrations tested is shown in Fig S1 (Appendix B). Interestingly, the sensor sensitivity was not considerably affected (S = 7.9±0.1/decade), indicating that the receptor's analyte binding capability remains unaltered by the choice of the blocking molecule. PEG implementation as a blocking molecule significantly enhanced the tolerance for the detection of spiked PfLDH in highly concentrated human serum. Plus, it allowed the detection of PfLDH in a wide range of concentrations, covering the clinically relevant detection range. The reported clinical concentration of PfLDH is found between a few pM to hundreds of nM, which correlates with the percentage of the parasitemia infection [8,167,168].

The *ex situ* detection for the PEG containing sensor was also tested, and the obtained equation, in this case, was $\Delta R_{ct}/R_{ct0}$ (%) = 7.2 lg$C$ + 51.1 with a correlation coefficient of 0.98. The calculated LOD was similar to the Aptamer/MCH sensor (1.5 pM), although, the aptasensor was incubated in whole human serum and subsequently measured in Tris buffer. The dynamic detection range (4.5 pM to 100 nM) and the sensitivity (S = 7.2/decade) were similar to *in situ* experiments (Fig 4.9c). That also indicates that the sensor's sensitivity is mainly independent of the implementation of the measurement (*in situ* or *ex situ*), but rather, the blocking molecule enhances the matrix tolerance, the LOD, and the detectable dynamic detection range. Table 4.5 summarizes the aptasensor parameters of PfLDH detection, including literature and the present work for *in situ* and *ex situ* detection.

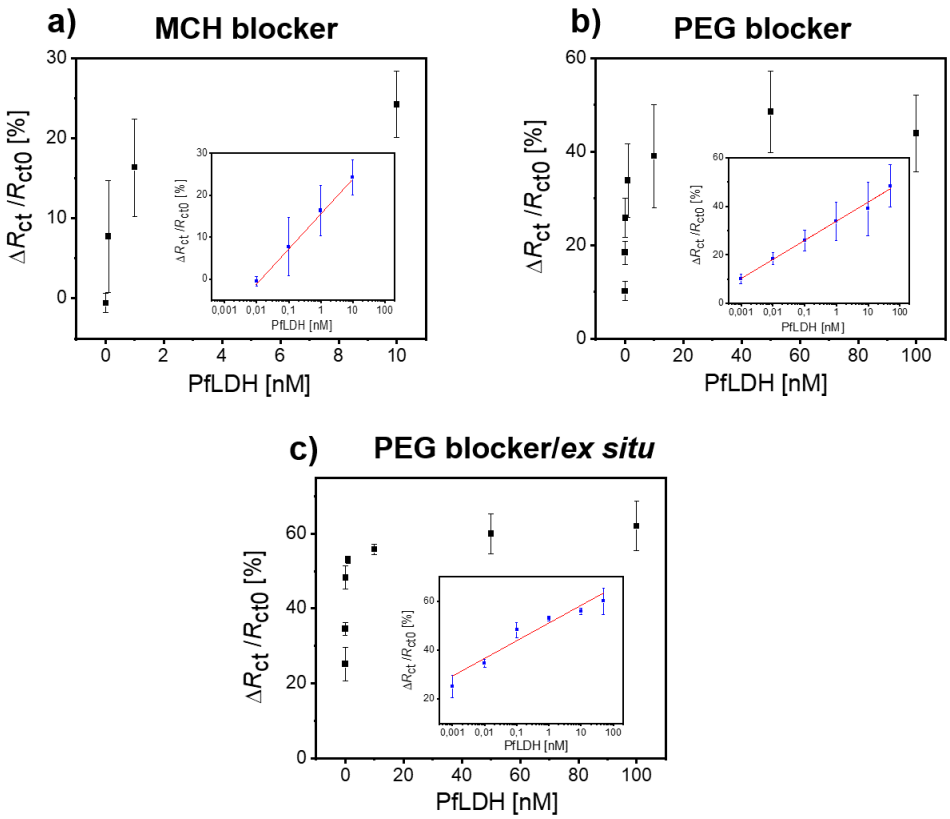

Figure 4.9 Calibration curves of PfLDH detection in human serum using a) MCH or b) PEG blocking molecules in *in situ* measurements, and c) PEG blocking molecule in *ex situ* measurements. All experiments were tested in triplicate.

Compared with previously reported characteristics, the new aptasensor developed with PEG as a blocking molecule possessed the lowest LOD and the most extensive dynamic range of detection for *in situ* measurements. Besides, this new aptasensor allowed PfLDH detection in less diluted (50%) human serum while previous works, including own previous work, using MCH as blocking molecule facilitated the detection only in highly diluted serum (10%). In the case of *ex situ* measurements, this easy to operate electrochemical aptasensor exhibited similar performance to state-of-the-art optical biosensors in whole human serum.

Table 4.5 Comparison of the performance of different aptasensors using varying blocking molecules for *in situ* and *ex situ* PfLDH detection.

		Receptor/ Blocker	Concentration of the medium used for target detection	Limit of detection	Dynamic range of detection	Reference
In situ	Electochem (EIS)	Aptamer/MCH	33% lysed-blood sample	1 parasite/uL	1 -3000 parasite/uL	[15]
	Electrochem (DPV)	Aptamer/no blocking	5% lysed-blood sample	----	-----	[169]
	Colorimetric	Aptamer/no blocking	10% human serum	13.54 pM	10 pM – 10 nM	[170]
	Electrochem (EIS)	Aptamer/MCH	10% human serum	1.3 pM	10 pM – 10 nM	[29]
	Electrochem (EIS)	Aptamer/PEG	50 % human serum	0.77 pM	2.3 pM – 100 nM	**Present work**
Ex situ	APTEC (colorimetric)	Aptamer/BSA	whole human serum, measured in PBS buffer	35.7 pM	35.7 pM – 35.7 nM	[132]
	Instrument-based Fluorescence spectroscopy	Aptamer/commercial blocking buffer (protein formulation)	whole human serum, measured in PBS buffer	1.72 pM	1 pM – 100 nM	[133]
	Electrochem (EIS)	Aptamer/PEG	whole human serum, measured in Tris buffer	1.49 pM	4.5 pM – 100 nM	**Present work**

EIS: electrochemical impedance spectroscopy; DPV: differential pulse voltammetry; APTEC: Aptamer-Tethered Enzyme Capture.

4.5 Sensor selectivity

The blocking film has an impact also on selectivity, which is an important parameter not only for clinical but also for point-of-care detection since elaborated pretreatments cannot be implemented in such applications. Therefore, the aptasensor response was challenged versus other serum components such as human serum albumin (HSA) and human lactate dehydrogenase B (hLDHB). HSA is the most abundant protein in human blood plasma, while hLDHB is the analyte's human analog with many structural correlations to PfLDH. Both can considerably interfere with the detection of PfLDH. For these experiments, the control proteins were spiked independently in the corresponding 50% human serum sample.

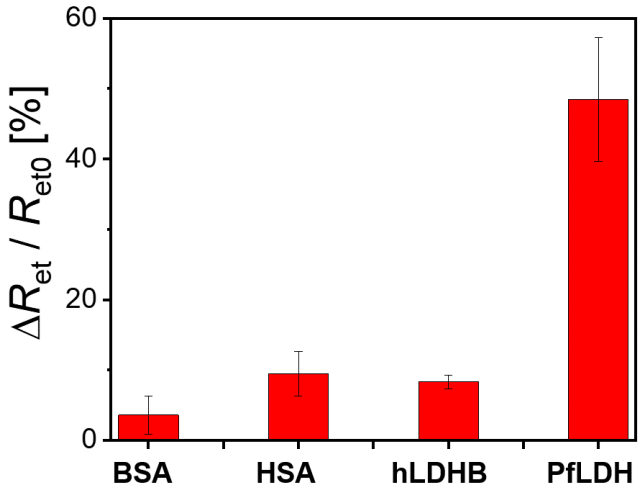

Figure 4.10 Selectivity of PfLDH detection vs. analogous proteins in human serum at 50 nM concentration for all proteins. All experiments were conducted in triplicate.

The malaria aptasensor exhibited a more significant impedance change for PfLDH compared to those compounds. Bovine serum albumin (BSA), HSA, and hLDHB caused only a marginally impedance change, although they were added at comparable high concentrations of PfLDH (Fig 4.10). The selectivity versus human LDHB was established already during the SELEX process by a counter target selection of the aptamer, indicating that the PEG blocking does not impair the selectivity of the aptamer receptor [14]. Furthermore, the long-term repulsion of serum protein was evaluated by impedance measurements at different incubation times in human serum. Only nonsystematic variations of the charge transfer resistance over time were observed, demonstrating the short-term stability of the PEG-modified aptasensor (Fig. 4.11a). However, at the long-term storage of the aptasensor, a considerable degradation of the signal was detected (Fig 4.11b). That might be associated with the continuous phase separation of the molecules since a single thiol anchoring group apparently cannot prevent the molecule phase separation over time effectively. Consequently, the possible implementation of aptamer molecules with multiple anchoring thiol groups might prevent such a phenomenon [171].

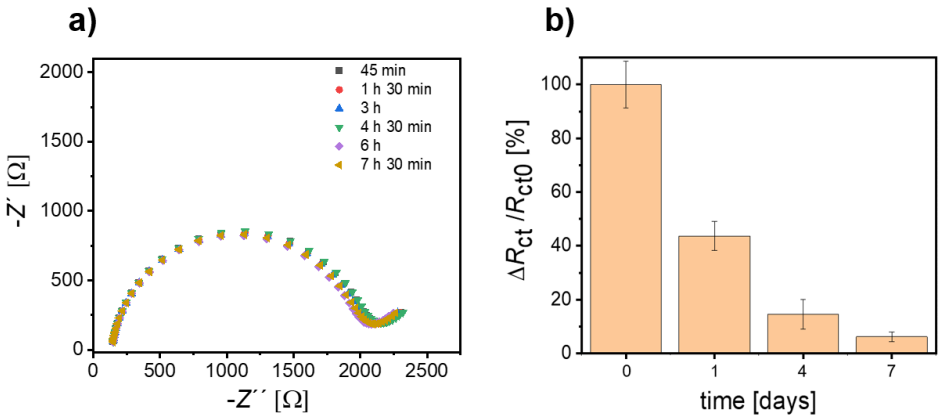

Figure 4.11 a) Impedance measurements at different times demonstrating the short-term stability of aptasensor incubation in human serum. b) Long-term storage depicting the degradation of the signal measured as the storing days increased.

Chapter 5

Flexible multielectrode array aptasensor for electrochemical multi-target detection in malaria parasite blood samples

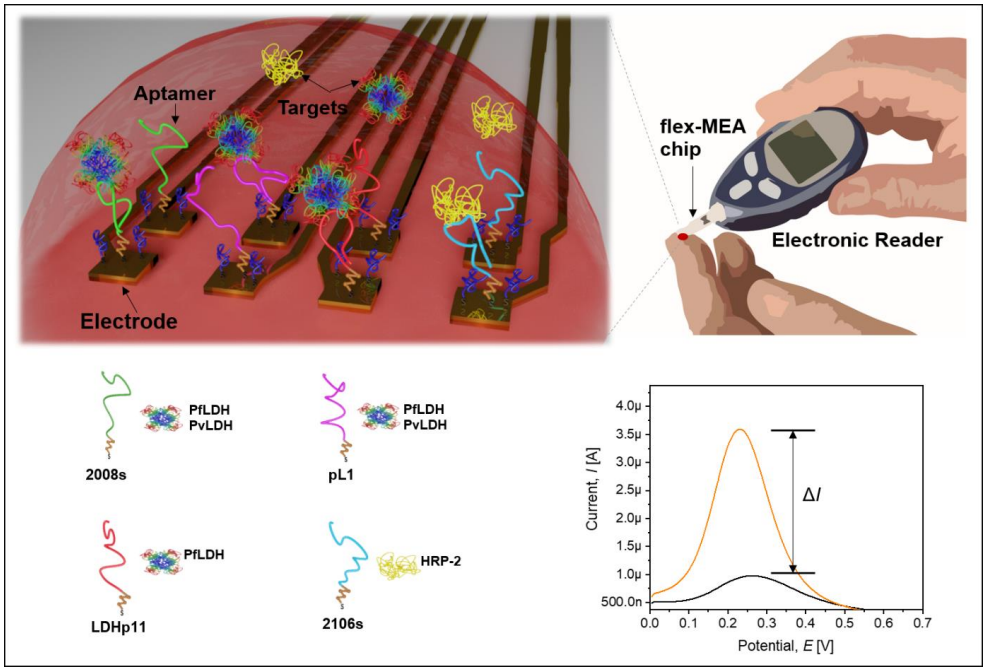

The following chapter was adapted in part from the following work:
G. Figueroa-Miranda, S. Chen, M. Neis, L. Zhou, Y. Zhang, Y. Lo, J. A. Tanner, A. Kreidenweiss, A. Offenhäusser, D. Mayer, "Multi-target electrochemical malaria aptasensor on flexible multielectrode arrays for detection in malaria parasite blood samples", Sensors and Acutators B: Chemical, 349, 130812, 2021 [172].

The multielectrode array (MEA) combine the advantages of a large detection area, by several electrodes, and low-noise recordings. The recording of several simultaneous signals from the different electrodes has significant benefits compared to traditional single-electrode systems since it permits the analysis of redundant signals and an averaging of the signals from multiple channels. Besides, the MEA allows immobilization of different aptamers on the different electrode sites for the simultaneous detection of multiple malaria biomarkers via individually addressable aptasensors. For some decades, the MEA approach has been used mainly to detect the physiological activity of electrogenic cells and their networks [173–181] or for nanoparticle impact detection [182,183]. Most recently, MEAs have become an exciting approach for multi-target electrochemical biosensing [45–47]. Liu *et al.* reported an electrode array aptasensor for the detection of two different secreted cytokines [46]. In this report, the authors used a hard quartz substrate for the fabrication of their electrodes, and they realized the double detection by labeling the aptamers with two different redox reporters. Recently, Zhang *et al*. has reported on the generation of a dual-aptamer biosensor for the detection of neuronal biomarkers ATP and amyloid-beta oligomers indicating the progression of Alzheimer's disease [47]. In this report, the hard, silicon-based substrate used was for the fabrication of their electrodes. The multi-target detection was realized by implementing electrochemical lithography to remove some previously immobilized aptamers and subsequent immobilization of the second aptamer receptor. The development of MEA on a flexible substrate, as reported by Adly *et at.*, Liang *et al.*, and Schnitker *et al.* [68,184,185], is of great advantage for low cost and easy realization of multi-target biosensors. In this chapter, the work regarding the fabrication of a flexible multielectrode array (flex-MEA) is presented. As describes in section 3.2.2, the flexible multielectrode arrays were fabricated on a polyethylene terephthalate polymer substrate by means of photolithography, wet chemical etching, and stencil vapor phase deposition. The as-prepared flex-MEAs were firstly characterized regarding their mechanical properties (extracted from Song Chen Mater's Thesis). The low cost and robust fabricated flex-MEA allowed the incubation of different sets of electrodes in four different aptamer solutions, in this way, providing the possibility to discriminate between the *Plasmodium falciparum* and *Plasmodium vivax* parasitic infection by the generation of a multi-target aptasensor. The detection of the generated flex-MEA multi-target aptasensor in blood samples with the spiked target proteins was analyzed. Posteriorly, the excellent flex-MEA multi-target aptasensor performance was demonstrated in whole blood samples with spiked *P. falciparum* parasites and *P. falciparum* parasite cultures. Finally, a cost analysis of this fabricated electrochemical flex-

MEA multi-target aptasensor is reported to evaluate their appropriateness for possible application as affordable point-of-care biosensor.

5.1 flex-MEA mechanical characterization demonstrates its robustness

The fabricated gold multielectrode arrays on a flexible polyethylene terephthalate (PET) substrate demonstrate to be quite robust, withstanding multiple bending cycles without apparent changes in its electrochemical performance. In order to conduct the mechanical bending test, the flex-MEA was fixed to the upper and bottom clamps of a tailor-made linear translation stage (Figure 5.1a).

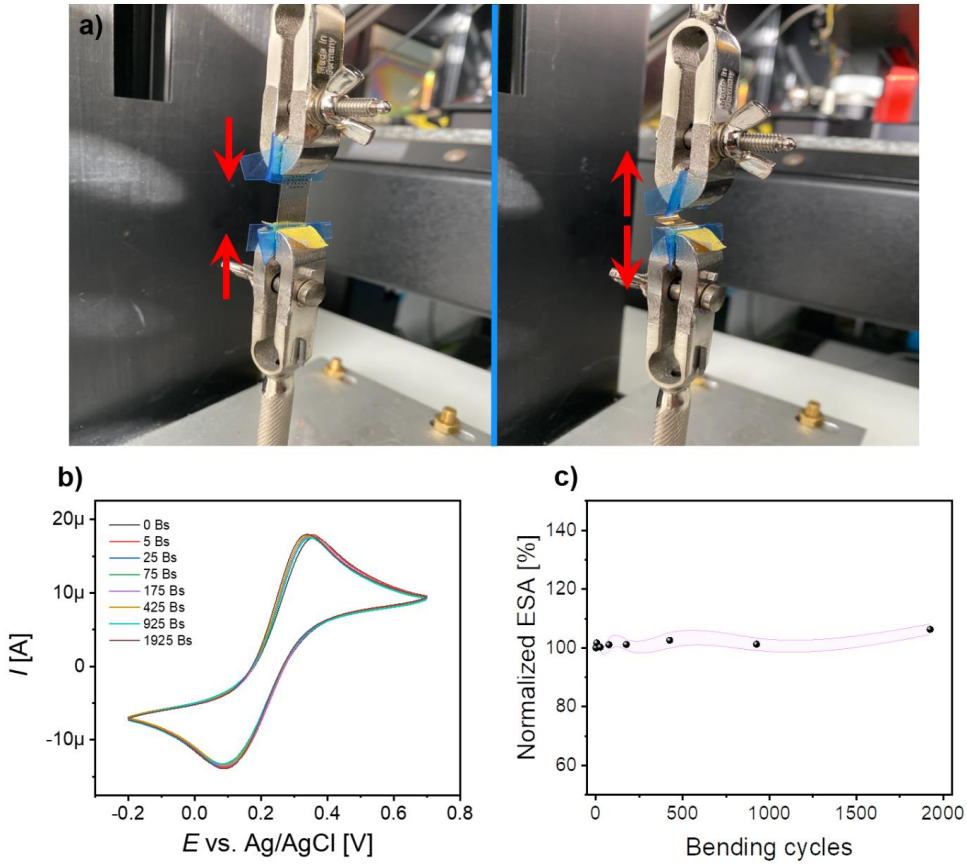

Figure 5.1 a) Mechanical bending test for flex-MEA. b) Characterization of the electrodes before (0 Bs) and after several bending repetitions (5, 25, 75, 175, 425, 925, and 1925 Bs) by cyclic voltammetry in 5 mM $[Fe(CN)_6]^{3-/4-}$ solution at pH 7.5. c) Normalized calculated electrochemical surface area (ESA) after the several bending cycles. (Extracted from Song Chen Master's Thesis)

Only the upper clamp was moved downwards with a 150 mm/min speed and retracted back to its original position, counting this movement as each bending cycle. After finalizing each set of specified amounts of bending cycles (5, 25, 75, 175, 425, 925, and 1925), the electrochemical performance of the electrodes was checked. As shown in Figure 5.1b, the cyclic voltammogram in 5 mM $[Fe(CN)_6]^{3-/4-}$ solution remained almost unaltered with less than 5 % of the peak current deviation. The calculated electroactive surface area (ESA) proved the sensor stability with a calculated value quite close to its original 100% after 925 bending repetitions (Figure 5.1c). Only, after 1925 bending cycles, a slight increment of the area was obtained (106.3 ± 1.8 %). That might be a consequence of possible cracks forming, contributing to the electrochemical signal. However, with this high number of withstood bending cycles on the flex-MEA electrodes, they proved to be very resistant to a harsh continuous bending treatment.

The implemented stencil passivation with Parylene-C polymer (Figure 3.2b) gives an extra advantage in the production cost over the commonly used lithographic cleanroom passivation, which required the utilization of several additional steps and reagents as compared in Table 5.1. The price of this stencil passivation fabrication is 58 % less compared to the lithographic passivation price. Even the flexible PET gives a lower cost fabrication cost advantage over silicon (Si) or quartz substrates (Table 5.2).

Table 5.1 Comparison of the fabrication costs by conventional lithography and by stencil passivation procedures.

Materials used	Lithography passivation per wafer (12 chips) / price USD	Stencil passivation per wafer (12 chips) / price USD
AZ 10XT	0.5	---
Parylene-C	0.9	0.9
AZ 400K (development)	0.8	---
AZ-100 (stripping)	0.5	---
PDMS	0.9	---
Tape Line-up ELEP HOLDER (Stencil)	---	0.10
Total	**3.6**	**1.5**

Table 5.2 Comparison of the fabrication costs per chip on different substrates.

Fabrication steps	flex-MEA fabrication per chip/ price USD			
	PET		Si	Quartz
	Lithography passivation	Stencil Passivation		
Electrodes	0.4	0.4	1.9	4.1
Passivation	0.3	0.1	0.3	0.3
Total	**0.7**	**0.5**	**2.2**	**4.4**

5.2 flex-MEA multi-target aptasensor characterization for the detection of spiked analytes in blood

The here implemented flexible PET polymer substrate allowed to divide the 20 electrodes of the flex-MEA chip into four sets of electrodes (see layout Appendix B Figure S4). That allows incubating different electrode sets in four different aptamer solutions (Figure 3.6) to realize a label-free multi-target aptasensor (Figure 5.2). The first implemented aptamer was the 2008s (green), previous electrochemically characterized, for detecting *Plasmodium falciparum* lactate dehydrogenase (PfLDH) biomarker [24,29]. The second used aptamer is pL1 (purple), which can detect both PfLDH and *Plasmodium vivax* LDH (PvLDH) proteins [15]. The third implemented aptamer is the so-called LDHp11 (red), highly selective for PfLDH [16]. The final fourth used receptor is the 2106s aptamer (blue), which selectively detects HRP-2 protein [49].

Differential pulse voltammetry (DPV) was the implemented method here for the detection of the aptamer-target binding (see section 2.3.4.1). Calibration curves were generated for each aptasensor to characterize the response for their respective target detection in a concentration range from 100 fM to 100 nM (Figure 5.3). The Langmuir-Freundlich adsorption isotherm formula (Eq. 2.1) was used to fit the obtained calibration curves and to describe quantitatively the detection with the different aptamers (see section 2.2.2). The obtained measured signal represents the coverage by the detected protein, θ, which is linearly proportional to the signal change of DPV. Therefore, it can be represented here as the relative peak current change due to target detection, $\frac{\Delta I}{I_0}$.

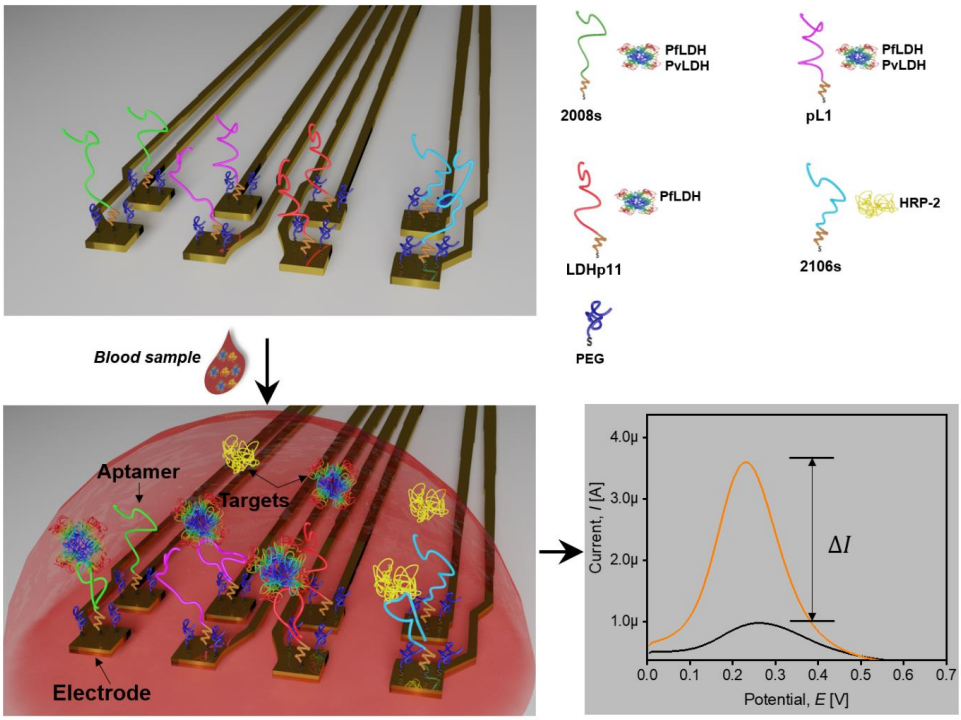

Figure 5.2 Schematic representation of the flex-MEA biofunctionalized with the four different aptamers: 2008s (green), pL1 (purple), LDHp11 (red), and 2106s (blue) (upper), and after target PfLDH and HRP-2 detection in blood (bottom). The plot depicts the peak current change (ΔI) after target detection obtained from the DPV measurements.

I_0 stands for the peak current measured before protein administration and ΔI the change of peak current after protein addition. Thus, the maximum possible signal obtained is represented as $\left(\frac{\Delta I}{I_0}\right)_{max}$. The calculated limit of detection (LOD) and other obtained performance factors are summarized in Table 5.3 for each aptamer. The aptamer surface densities were optimized in advance for each step to obtain an optimal signal for the detection of the respective analytes (See appendix B, Fig. S5).

The first characterized aptamer was the 2008s (Figure 5.3a, Table 5.3), which targets PfLDH, with a calculated LOD value of 7.25 fM. The maximum signal obtained $\left(\frac{\Delta I}{I_0}\right)_{max}$ from the fitting to the experimental data was 12.1, correlating with the observed saturation reached at 100 nM for PfLDH detection. Thus, the aptasensor showed a semi-logarithmic dynamic

detection range lasting from 7.25 pM to 10 nM. This flex-MEA aptasensor demonstrated an improved LOD of two orders of magnitude compared with a previously reported system on a single gold rod electrode tested in human serum samples [24]. However, the sensitivity here obtained was smaller, which might be associated with the almost five-times smaller area of flex-MEA electrodes compared with the single gold rod electrode (Appendix B, Table S1). The crosselectivity observed for the 2008s aptamer versus the analog PvLDH can be a consequence of the high analogy with the PfLDH target protein and the consequence of the non-specific binding of the aptamer the histidine residues (required for protein purification) from the contained tag in this recombinant protein. The last explanation also applies to the unspecific HRP-2 observed detection (Figure 5.4a). The analysis of the crystal structure of the complex 2008s aptamer-PfLDH has been demonstrated to bind to histidine amino acids of the protein [14]. The second characterized aptamer was the pL1 (Figure 5.3b), which also targets PfLDH and PvLDH [15]. This system had calculated LOD of 22.30 fM and a similar sensitivity like the 2008s aptamer (Table 5.3). Its $\left(\frac{\Delta I}{I_0}\right)_{max}$ was 15.0, which correlated with the observed saturation at 100 nM PfLDH concentration. The semi-logarithmic dynamic detection range for this aptamer was from 22.30 fM to 100 nM. Although this aptamer is reported to target also PvLDH, in the crosselectivity results (Figure 5.4b), there was a smaller signal response for this protein (LOD = 138 pM). That might be because, in the original work that reports on the PvLDH detection, the used working pH conditions were different (pH 8) [48]. In the scope of this work, the physiological pH conditions of 7.5 were used. Besides, similar crosselectivity for HRP-2 was also observed (Figure 5.4b). The third characterized aptamer was the LDHp11 (Figure 5.3c), which is reported as exclusively targeting PfLDH. Such selective detection for PfLDH was demonstrated versus PvLDH and HRP-2 proteins (Figure 5.4c). This sensor had a calculated smaller LOD = 1.80 fM compared with the previous aptamers, and with similar sensitivity S = 2.5 ± 0.1 / decade and with a $\left(\frac{\Delta I}{I_0}\right)_{max}$ = 17.2, correlating with the signal measured with the highes (100 nM) PfLDH concentration tested. For this aptamer, the semi-logarithmic concentration-dependence was in the range from 1.80 fM to 100 nM. In general, the LODs and dynamic detection ranges of these three aptamers targeting PfLDH, with different selectivities over PvLDH, complement each other giving an excellent sensitivity similar to reported state-of-the-art sensors in biological samples [10,23] and with a broad dynamic detection range for this target protein (1.80 fM to 100 nM). Moreover, the immobilization of different aptamers that target different plasmodium epitopes of the same dehydrogenase provides a more accurate

analysis of the sample composition compared to single target detection, avoiding the uncertainty of detection because of cross-selectivity.

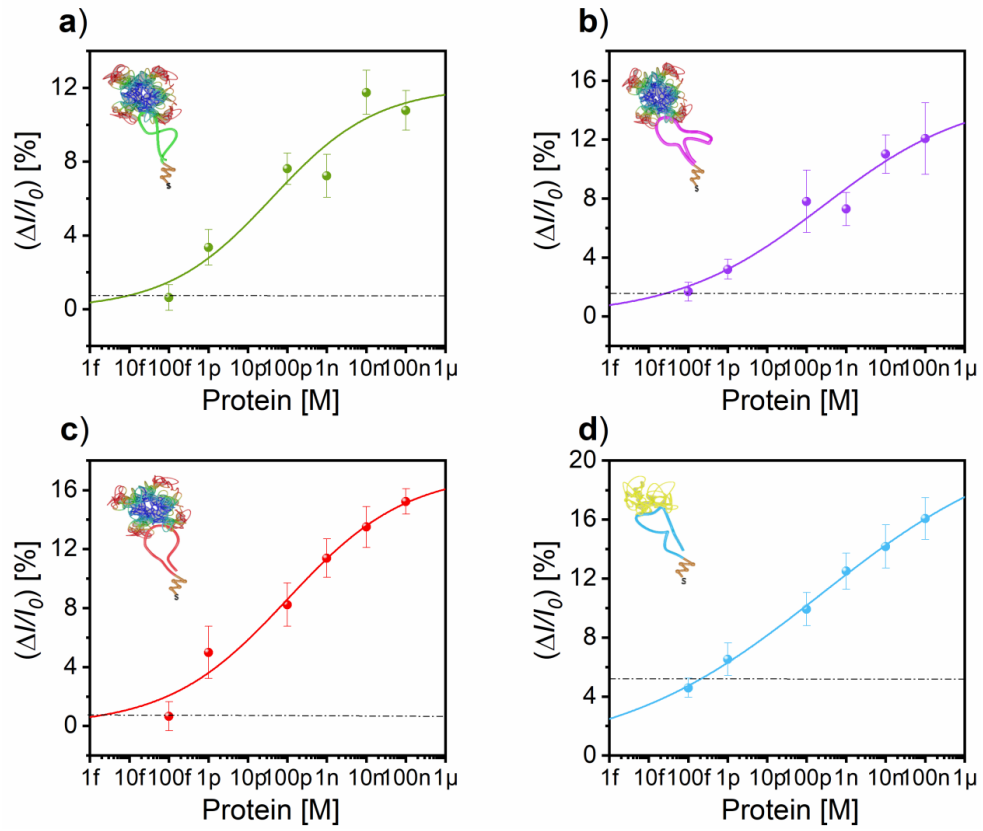

Figure 5.3 Calibration curves with spiked target analyte in blood samples. The PfLDH target protein was detected by a) 2008s aptamer, b) pL1 aptamer, and c) LDHp11 aptamer. HRP-2 protein was detected by d) 2106s aptamer. All proteins were sensed in a range from 100 fM to 100 nM.

The fourth characterized receptor was the 2106s aptamer (Figure 5.3d), which detects the HRP-2 protein exclusively produced by the Plasmodium falciparum parasite. Its calculated detection performance in blood samples was also excellent, with a low LOD of 0.15 pM and a high sensitivity (see Table 5.3). The maximum calculated signal $\left(\frac{\Delta I}{I_0}\right)_{max}$ was 21.9, which was obtained without reaching a full saturation at 100 nM. The obtained semi-logarithmic dynamic detection range with this aptamer was from 0.15 pM to 100 nM. This aptamer demonstrated an excellent detection performance as other reported state-of-the-art electrochemical aptasensors

targeting also HRP-2 [10,12,23]. It also proved its outstanding selectivity for its target protein vs. PfLDH and PvLDH (Figure 5.4d). All aptamers were checked for cross-reactivity towards the human lactate dehydrogenase B (hLDHB) protein that is intrinsically present in human blood samples (Figure 5.4). The flex-MEA multi-target aptasensor showed a smaller unspecific signal with hLDHB as compared with its specific targets.

A recent study reported by Jimenez *et al*. calculated the analytical detection limits of the classified best-in-class malaria RDTs, according to WHO, by comparison with quantitative ELISA tests [9]. In that work, detection limits reported for pLDH and HRP-2 were 25 ng/mL (178 pM) and 0.8 ng/mL (26 pM), respectively. Those values are five and two orders of magnitude higher than the here reported detection limit values for PfLDH and HRP-2 with this multi-target flex-MEA aptasensor, respectively.

Not only specific detections associated with single target detection but also selective detections, related to several different detected targets, were observed for the different aptamers [186]. Summarizing the specific or selective detection observed in Figure 5.4, 2008s aptamer demonstrated to have selectivity to detect PfLDH, PvLDH (due to analogy to PfLDH) and HRP-2 (due to histidine tag residues). pL1 aptamer showed to be selective for PfLDH and HRP-2 (due to histidine tag residues) and slightly selective for PvLDH. LDHp11 aptamer demonstrated its specificity for PfLDH at lower concentrations, at higher than 1 nM it showed small crosselectivity with the other proteins. 2106s also demonstrated its specificity for HRP-2 versus the other proteins with a slight increment in the signal for high concentration of PfLDH.

Table 5.3 Obtained performance factor for target detection in blood samples by the multi-target flex-MEA aptasensor.

Aptamer/ target protein	Limit of detection (LOD)	Sensitivity (S)	Dynamic range of detection
2008s / PfLDH	7.25 fM	1.9 ± 0.2 / decade	7.25 fM - 10 nM
2008s / PvLDH	0.42 pM	1.4 ± 0.3 / decade	0.42 pM - 100 nM
pL1 / PfLDH	22.30 fM	2.1 ± 0.2 / decade	22.30 fM - 10 nM
pL1 / PvLDH	138 pM	2.1 ± 0.2 / decade	138 pM - 10 nM
LDHp11 / PfLDH	1.80 fM	2.5 ± 0.1 / decade	1.80 fM - 100 nM
2106s / HRP-2	0.15 pM	2.0 / decade	0.15 pM - 100 nM

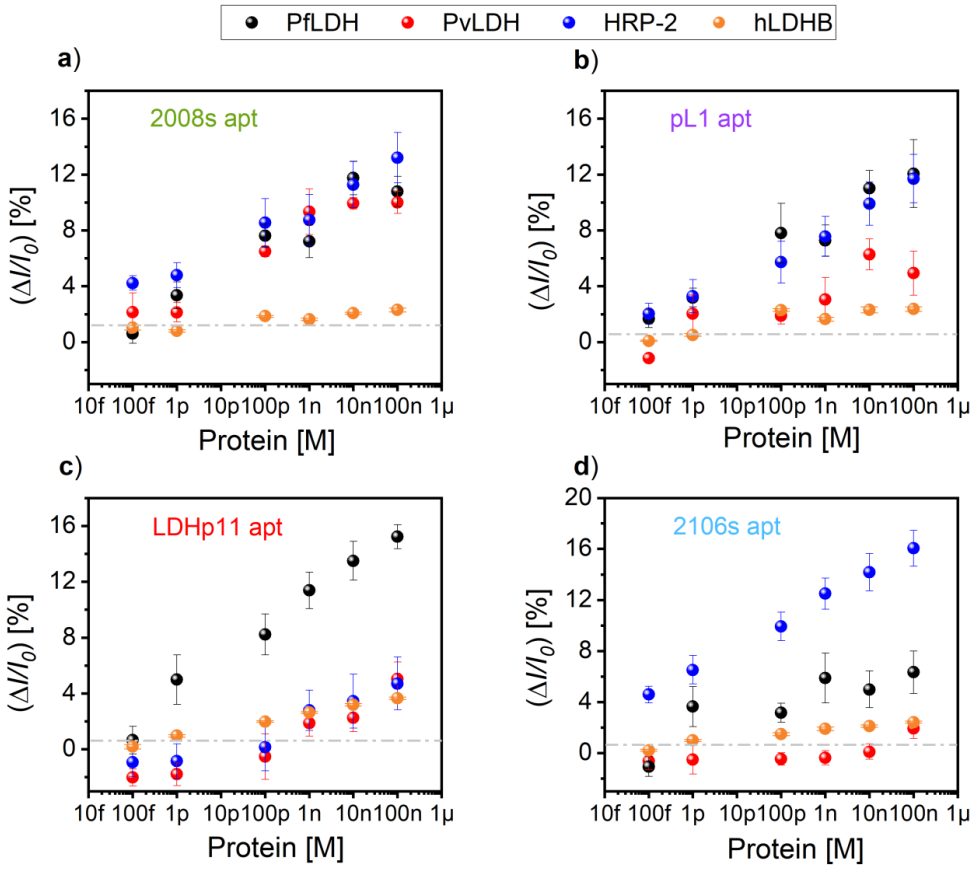

Figure 5.4 Crosselectivity of aptamers versus target proteins. Aptasensors a) 2008s, b) pL1, c) LDHp11, and d) 2106s were tested for binding to individual blood samples spiked with either PfLDH, PvLDH, or HRP-2, or versus control human LDH B (hLDHB).

In order to take advantage of the different signal outputs from different aptamer receptors, a combination of the different outputs can be operated as logic gates, which correlate with the input coming from the sample (Table 5.4). The signal is considered as being 0 or 1 if the measured current is below or above the LOD threshold (Figure 5.4). The output significance denotes whether or not the combination of respective Inputs is meaningful (PfLDH and HRP-2 have to be co-expressed) for the diagnosis. The output of the respective sensors delivers many unclear sensor outputs, so it is impossible to charge on the infection for many scenarios by considering the output of only one sensor.

Table 5.4 Input and output table for the different biomarker detections by sensors with respective aptamers.

Aptamer	Inp 1 (PfLDH)	Inp 2 (PvLDH)	Inp 3 (HRP-2)	Output	Output significance
2008s	0	0	0	0	Clear
	1	0	0	1	Unclear
	0	1	0	1	Clear
	1	1	0	1	Unclear
	0	0	1	1	Unclear
	1	0	1	1	Clear
	0	1	1	1	Unclear
	1	1	1	1	Clear
pL1	0	0	0	0	Clear
	1	0	0	1	Unclear
	0	1	0	1	Clear
	1	1	0	1	Unclear
	0	0	1	1	Unclear
	1	0	1	1	Clear
	0	1	1	1	Unclear
	1	1	1	1	Clear
LDHp11	0	0	0	0	Clear
	1	0	0	1	Clear
	0	1	0	0	Clear
	1	1	0	1	Unclear
	0	0	1	0	Unclear
	1	0	1	1	Clear
	0	1	1	0	Unclear
	1	1	1	1	Unclear
2106s	0	0	0	0	Clear
	1	0	0	0	Unclear
	0	1	0	0	Clear
	1	1	0	0	Unclear
	0	0	1	1	Unclear
	1	0	1	1	Clear
	0	1	1	1	Unclear
	1	1	1	1	Unclear

In order to set the outputs to “clear” and to facilitate a selective and unambiguous detection of the biomarker and a corresponding diagnose, logic operations are performed, which are comprised in input and output tables (Table 5.5, 5.7, and 5.9). There, the different outputs of the electrodes on a chip are combined. Therefore, the outputs for the respective sensors (Table 5.4) are used as input for logic gates, and corresponding truth tables are derived for specific parasitic infection scenarios that can be checked by the sensor (Table 5.6, 5.8, and 5.10). The combination of the several aptamer outputs and processing these sensor outputs by logic gate operations permits unambiguous detection of malaria infections, discrimination between

different malaria parasites, confirm the result by redundant sensor analysis, as well as discard the possibility of a false-positive result, like in Table 5.10. Besides, all electrodes of an electrode set are modified with the same aptamer receptor, therefore, the signals coming from several electrodes are averaged. The averaging of the data recorded in parallel increases the reliability of the measurement information. In the following three examples, logic operations are reported, but various other logic operations of multiple levels could be executed.

Example I: *Plasmodium falciparum*

Table 5.5 Input and output table for sensors modified with LDHp11 aptamer and 2106s aptamer for the detection of different combinations of biomarkers. The output is 1 only if both *P. falciparum* biomarkers (PfLDH + HRP2) are detected. A coinfection with *P. vivax* is not excluded. We get a 1 only if both aptasensors give a signal above their respective threshold.

	Inp 1 LDHp11	**Inp 2 2106s**	**Output *P. falciparum***
0	0	0	0
PfLDH	1	0	0
PvLDH	0	0	0
PfLDH + PvLDH	1	0	0
HRP-2	0	1	0
PfLDH + HRP-2	1	1	1
PvLDH + HRP-2	0	1	0
PvLDH +PfLDH + HRP2	1	1	1

Table 5.6 Truth table of combination from LDHp11 and 2106s for *P. falciparum* infection via AND gate. Logic diagram: output=$Inp1 * Inp2$

Inp 1 LDHp11	**Inp 2 2106s**	**Output *P. falciparum***
0	0	0
1	0	0
0	1	0
1	1	1

1: indicates an unambiguous positive response according to the addressed task (here: infection with *P. falciparum*).

0: indicates ambiguous test outcome due to cross selectivity of the aptamer receptors or no infection.

Example II: Only *Plasmodium vivax* infection

Table 5.7 Input and output table for the combination of detection from 2008s, LDHp11, and 2106s aptamers for only *P. vivax* detection. A coinfection with *P. falciparum* is excluded. We get a 1 only when 2008s aptasensor gives a positive signal.

	Inp 1 2008s	**Inp 2 LDHp11**	**Inp 3 2106s**	**Output Only *P. vivax***
0	0	0	0	0
PfLDH	1	1	0	0
PvLDH	1	0	0	1
PfLDH + PvLDH	1	1	0	0
HRP-2	1	0	1	0
PfLDH + HRP-2	1	1	1	0
PvLDH + HRP-2	1	0	1	0
PvLDH +PfLDH + HRP2	1	1	1	0

Table 5.8 Truth table of combination from 2008s, LDHp11, and 2106s for only *P. vivax* infection via NOT/NOR - NOT/NOR gate. Logic diagram: output= $\overline{\overline{\overline{Inp1} + \overline{Inp2}} + Inp3}$.

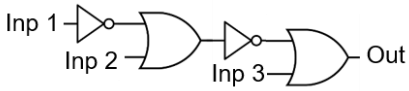

Inp 1 2008s	**Inp 2 LDHp11**	**Output 1**	**Inp 3 2106s**	**Output 2 *P. vivax***
0	0	0	0	0
1	0	1	0	1
0	1	0	0	0
1	1	0	0	0
0	0	0	1	0
1	0	1	1	0
0	1	0	1	0
1	1	0	1	0

Example III: Detection corroboration by redundant sensor signals

Table 5.9 Input and output table for the combination of detection from 2008s and pL1 aptamers for P. falciparum, P. vivax, or co-infection, giving a redundant signal for discarding a false-positive result. We get a 1 only if both aptasensors give a signal above their respective threshold.

	Inp 1 2008s	**Inp 2 pL1**	**Output *P. falciparum* and *P. vivax***
0	0	0	0
PfLDH	1	1	1
PvLDH	1	1	1
PfLDH + PvLDH	1	1	1
HRP-2	1	1	1
PfLDH + HRP-2	1	1	1
PvLDH + HRP-2	1	1	1
PvLDH +PfLDH + HRP2	1	1	1

Table 5.10 Truth table of combination from 2008s and pL1 modified sensors for the redundant corroboration of a *P. falciparum* and *P. vivax* co-infection detection via AND gate. Logic diagram: output=$Inp1 * Inp2$

Inp 1 2008s	**Inp 2 pL1**	**Output *P. falciparum* and *P. vivax***
0	0	0
1	0	0
0	1	0
1	1	1

The short-termed stability of the multi-target aptasensor was tested and demonstrated over a monitored time from 45 min to 7.5 h (Figure 5.5a). Only small non-systematic signal alterations (< 10 %) for the aptamers were registered during this time. However, at long-term storage (> 1 day) in buffer solution at 4 °C, a considerable degradation of the signal was observed (Figure 5.5b), similar to previously reported for 2008s aptamer [24]. This degradation has been associated with a phase separation observed over time between the aptamer and the PEG blocking molecules. However, this can be overcome by implementing aptamers with multiple anchoring thiol groups, which can help to reduce the surface diffusion of adsorbed molecules and thus enhance the long-term stability of this multi-target aptasensor performance [171].

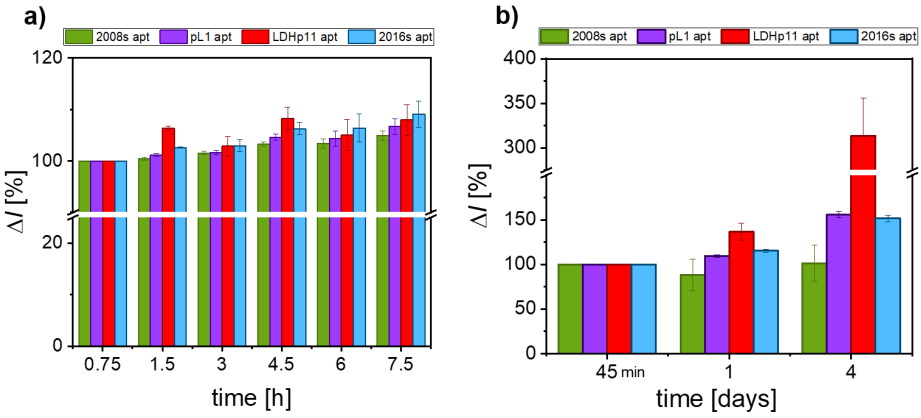

Figure 5.5 a) Short-term stability in hours for 2008s, pL1, LDHp11, and 2106s aptamers. b) Long-term stability over days for 2008s, pL1, LDHp11, and 2106s aptamers.

5.3 Measurement of *Plasmodium falciparum* parasitemia in blood samples by flex-MEA multi-target aptasensor

Two kinds of parasitized samples were used to determine the parasitemia in real samples: blood spiked with *Plasmodium falciparum* parasites (Figure 5.6) and *Plasmodium falciparum* culture (Figure 5.7). In both cases, the samples were compared versus a negative blood control (uninfected blood, uRBC) and tested in a range from 0.0001 to 5 % of parasitemia counted as the number of infected red blood cells (iRBC) (<50 – 270000 parasites/µL) [187].

Figure 5.6 indicates the normalized peak current response in blood samples with spiked *Plasmodium falciparum* parasite at different percentages of parasitemia and uninfected blood (control) samples. The signal response for every single electrode of the flex-MEA was considered positive (threshold value) when it was higher than the mean control response + 3σ.

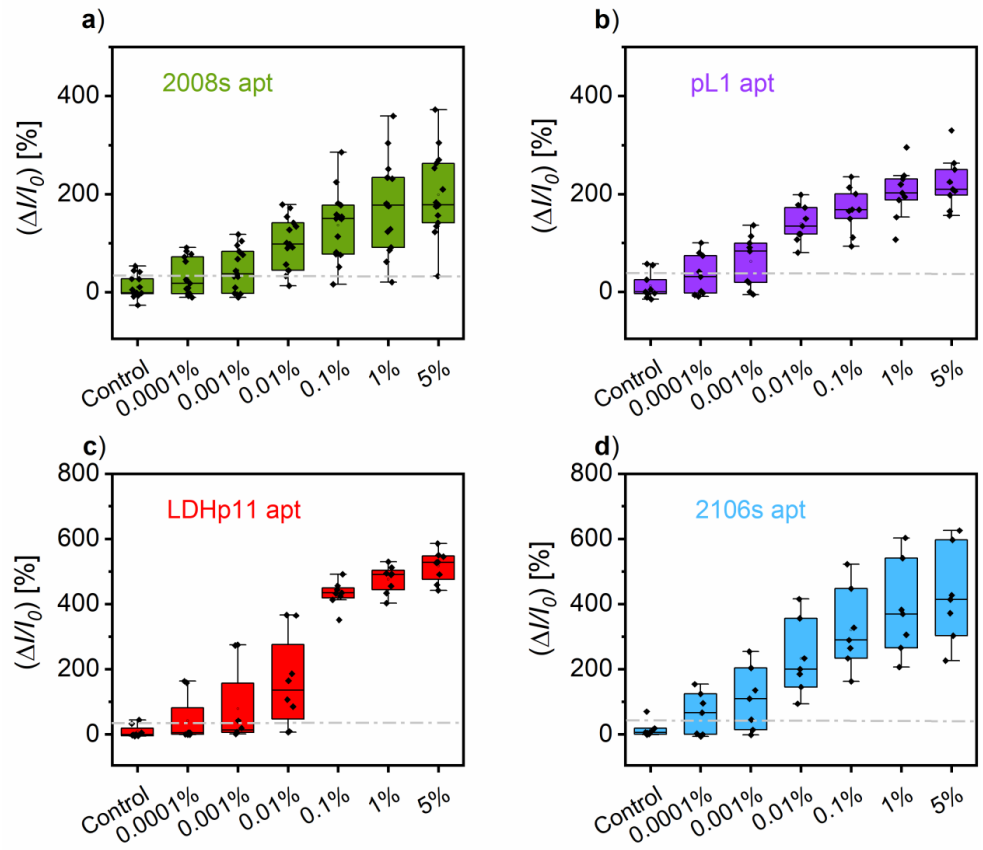

Figure 5.6 Detection of specific biomarkers in whole blood samples with spiked *Plasmodium falciparum* parasites. a) 2008 aptamer (green), b) pL1 aptamer (purple), c) LDHp11 aptamer (red) and d) 2106s aptamer (blue). The % represents the percent of parasitemia.

The sensitivity of the parasitemia detection for each aptamer was calculated as the number of positive signal responses among the total number of positive samples. The specificity, which is defined as the number of negative signals among the total number of negative control samples, was also calculated. In the case of the 2008s aptamer (threshold value of $(\Delta I/I_0) = 28.2$), a sensitivity of 93.3 % for a parasitemia of 0.01 % was obtained (Figure 5.6a and Table 5.11). For lower density parasitemia, the sensitivity was smaller than 75 %. For the pL1 aptamer (threshold value of $(\Delta I/I_0) = 39.8$), the response was higher with a sensitivity of 100 % as low as 0.01 % (Figure 5.6b). The LDHp11 (threshold value of $(\Delta I/I_0) = 28.6$) showed a sensitivity of 100 % for 0.1 % parasitemia (Figure 5.6c). The 2106s aptamer (threshold value of $(\Delta I/I_0) = 43.8$) demonstrated also 100 % sensitivity for 0.01 % parasitemia (Figure 5.6d). Thus, in the case of the 2008s, pL1, and 2106s aptamers for *P. falciparum*-positive blood

samples, the detection limit (>75 %) is considered at 0.01% parasitemia (500 parasites/µL) with 93.3 %, 100 %, and 100 % sensitivities, respectively. For the LDHp11 aptamer, a higher detection limit of 0.1 % parasitemia (5000 parasites/µL) was obtained with 100 % sensitivity. The sensitivities found here (>90 % for 0.01% parasitemia) were even higher than sensitivities reported for commercial RDTs (< 90 %) with the same percentage of parasitemia for PfLDH detection [168,187]. In the case of HRP-2 detection with commercial RDTs, higher sensitivities (≈98 %) were reported for the same percentage of parasitemia, similar to the detections obtained in this work with 100 % sensitivity [11,168]. This might be associated with the fact that such copious protein is also produced during the parasite life cycle, but it has a longer half-life than PfLDH since HRP-2 tests have been reported to show positive results even months after the parasite clearance [11]. Another advantage that this multi-target aptasensor offers is that, apart from discriminating, it can corroborate a real infection by detecting different biomarkers as illustrated before with the logic gate output signals. This detection redundancy is important since, in some malaria-endemic areas, like in South America, HRP-2 is not expressed by the parasite [13].

The specificities of pL1 and LDHp11 aptamers were around 75 % (see Table 5.11). For the 2008s and 2106s aptamers, their specificities were higher, with 80.0 % and 85.7 %, respectively. Although these are still not the desired specificities indicated by the WHO regulations (>90 %), this multi-target aptasensor proved higher specificities than the reported for commercial RDTs like Paracheck-Pf with 68 %, SD Bioline 39 %, and First response malaria 42 % [11,188].

Table 5.11 Performance of multi-target flex-MEA aptasensor on whole blood samples with spiked *Plasmodium falciparum* parasites.

Parasitemia (%)	**2008s apt**		**pL1 apt**		**LDHp11 apt**		**2106s apt**	
	Sensitivity (%)	**Specificity (%)**	**Sensitivity (%)**	**Specificity (%)**	**Sensitivity (%)**	**Specificity (%)**	**Sensitivity (%)**	**Specificity (%)**
5	100	---	100	---	100	---	100	---
1	93.3	---	100	---	100	---	100	---
0.1	93.3	---	100	---	100	---	100	---
0.01	93.3	---	100	---	37.5	---	100	---
0.001	66.7	---	55.6	---	25.0	---	71.4	---
0.0001	33.3	---	44.4	---	25.0	---	57.1	---
Negative Control	---	80.0	---	77.8	---	75.0	---	85.7

Even more, this aptasensor demonstrated specificities in a similar range, like sensitive ELISA tests (88 %) [2]. The specificity is one of the characteristics of RDTs from which they suffer the most, even among different lot numbers of production [13,189]. Nonetheless, this parameter, according to the WHO, does not represent a critical performance factor as the sensitivity does, as stated by WHO: “sometimes it may be more important to have very high sensitivity even at the expense of high specificity, as a missed parasitemia may lead to the death of a patient" [190].

In the case of the *Plasmodium falciparum* parasite cultures, the obtained sensitivities were higher for all the tested aptamers. For 2008s aptamer (threshold value of ($\Delta I/I_0$) = 60.0) 83.3 % for 0.001 % parasitemia (Figure 5.7a and Table 5.12), for pL1 aptamer (threshold value of ($\Delta I/I_0$) = 56.6) 80 % for 0.001 % parasitemia (Figure 5.7b), for LDHp11 (threshold value of ($\Delta I/I_0$) = 139.3) 80 % for 0.0001% parasitemia (Figure 5.7c) and 2106s aptamer (threshold value of ($\Delta I/I_0$) = 66.0) 83.3 % for 0.001 % parasitemia (Figure 5.7d). Therefore, the considered limit of detection is at 0.001 % parasitemia (50 parasites/µL) for 2008s, pL1 and 2106s aptamers with this samples demonstrating >75 % sensitivity. For LDHp11 the detection limit was even smaller at 0.0001 % (<50 parasites/µL) with 100 % sensitivity. This multi-target aptasensor developed here fulfills and even surpasses the standard required by the WHO of minimum detection of 75 % at 200 parasites/ µL [13].

In the strict sense, the actual specificities obtained for the 2008s aptamer of 83.3 %, for pL1 aptamer of 70 %, for LDHp11 aptamer of 100 %, and 83.3 % for 2106s aptamer were higher as compared with the spiked parasite blood samples (Table 5.11). Such differences in sensitivity and specificity between the different kinds of samples might be a consequence of the different amounts of target proteins present. On the one hand, the samples can contain infected red blood cells (iRBC) with parasites at different stages of the infection, which produced a different amount of the target proteins [11]. On the other hand, some target proteins like HRP-2 are secreted in the medium by the parasite [11,27], which this biosensor can detect.

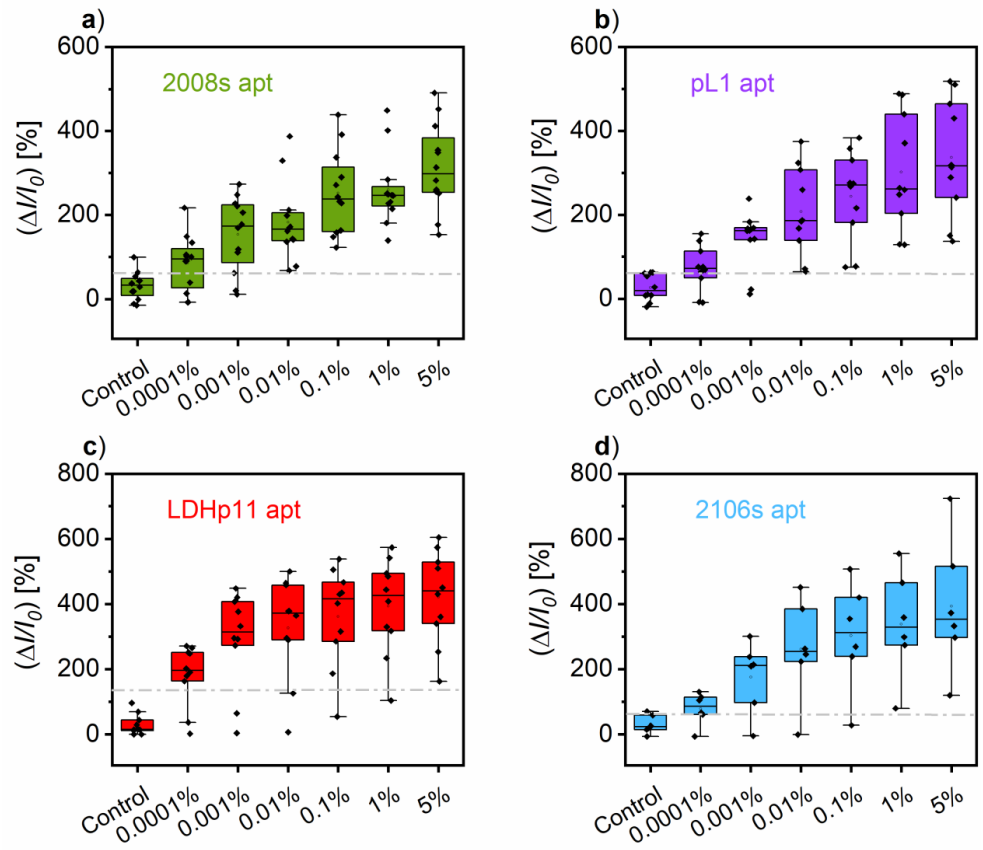

Figure 5.7 Detection of specific biomarkers in samples of *Plasmodium falciparum* parasite culture. a) 2008 aptamer (green), b) pL1 aptamer (purple), c) LDHp11 aptamer (red) and d) 2106s aptamer (blue). The % represents the percent of parasitemia.

Additionally, control experiments demonstrated that the specific aptamer sequences obtained higher signals as compared with random ssDNA sequences in both parasitized blood and cultured *Plasmodium falciparum* samples (Appendix B, Figure S6, and S7). Even an extra control with receptor-free electrode surfaces blocked only with PEG was performed (Figure 5.8) with only a smaller fouling effect (≈15 %) compared with the specific aptamer-target signals obtained in the blood samples (Figure 5.6 and S6).

Table 5.12 Performance of multi-target flex-MEA aptasensor on samples of *Plasmodium falciparum* parasite cultures.

Parasitemia (%)	2008s apt		pL1 apt		LDHp11 apt		2106s apt	
	Sensitivity (%)	Specificity (%)	Sensitivity (%)	Specificity (%)	Sensitivity (%)	Specificity (%)	Sensitivity (%)	Specificity (%)
5	100	---	100	---	100	---	100	---
1	100	---	100	---	90.0	---	100	---
0.1	100	---	100	---	90.0	---	83.3	---
0.01	100	---	100	---	80.0	---	83.3	---
0.001	83.3	---	80.0	---	80.0	---	83.3	---
0.0001	66.7	---	70.0	---	80.0	---	16.7	---
Negative Control	---	83.3	---	70.0	---	100.0	---	83.3

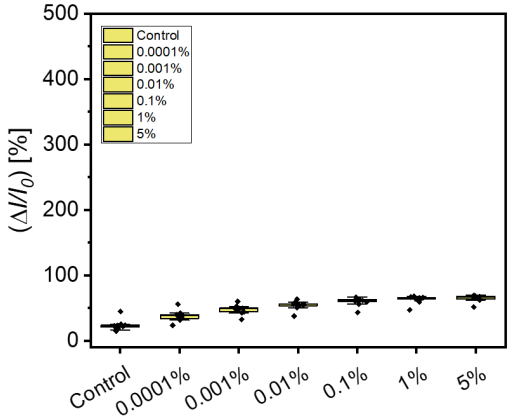

Figure 5.8 Small fouling effect in a receptor-free surface, blocked with PEG. This sensor was challenged in blood samples with spiked *Plasmodium falciparum* parasites. The % represents the percent of parasitemia. The y axis scales up to 500 to corroborate with the smallest signal scale for one of the specific aptamer detections shown in Figure 5.6.

5.4 flex-MEA multi-target aptasensor cost analysis

As know, malaria is prevalent in tropical and developing countries, so it is essential to fabricate a biosensor for malaria detection with as low as possible fabrication costs. The analysis regarding the possible cost of a flex-MEA multi-target aptasensor used for point-of-care detection was estimated, and this was compared with reported prices for commercial RDTs and other reported developed technologies (Table 5.13).

Table 5.13 Cost analysis for the developed multi-target flex-MEA aptasensor compared with commercial RDTs and other reported detection methods.

Components	**Price (USD)**				
	Multi-target flex-MEA aptasensor (electrochem.)	**AnyMDx (fluorescence) (Choi et al. 2016)**	**APTEC syringe test (colorimetric) (Dirkzwager et al. 2016)**	**uMED (electrochem.) (Nemiroski et al. 2014)**	**Antibody-based RDT (colorimetric) (Albertini et al. 2012, Hansen et al. 2017)**
Electronic module/ prototype	25	176	0.10	25	---
Chip+carrier/ sampler	2.11	1.14	---	N.R.	---
Aptamers+ Reagents	1.44	---	1.66	N.R.	---
Price per test	**3.55**	**1.14**	**1.66**	**N.R.**	**1-17**
Total	≈30	177.14	1.76	≈30	1-17

N.R.: not reported

As shown in Table 5.13, the price per test of this fabricated multi-target flex-MEA aptasensor is around the price for the commercial qualitative RDTs and cheaper for some of the other proposed technologies. The electronic module, which is the costly part of this sensor, needs to be purchased one time, and it can be used for a large number of tests. Besides, this highly sensitive electrochemical aptasensor possesses the advantage of detecting quantitatively different biomarkers on several electrodes in a highly redundant manner, facilitating high reliability of the malaria test discarding false-positive results. Furthermore, it provides the capability to discriminate between *Plasmodium falciparum* and *Plasmodium vivax* parasitic infection, helping in correctly guiding the patient's treatment.

Chapter 6

Ultrasensitive graphene-based field-effect transistor aptasensor for malaria detection in human serum

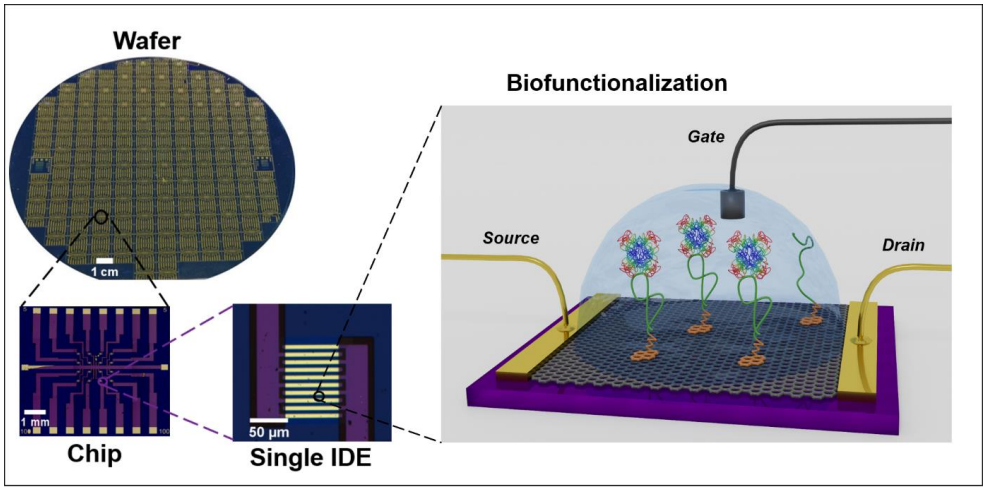

The following chapter was adapted in part from the following work:
G. Figueroa-Miranda, Y. Liang, M. Suranglikar, M. Stadler, N. Samane, M. Tintelott, Y. Lo, J. A. Tanner, X. T. Vu, J. Knoch, S. Ingebrandt, A. Offenhäusser, V. Pachauri, D. Mayer, "Delineating charge and capacitance transduction in system-integrated graphene-based BioFETs used as aptasensors for malaria detection ", manuscript submitted for publication, 2021.

Graphene-based field-effect transistor biosensors (G-FET) are another miniaturized detection platform with excellent performance and the possibility of multiplexing. Those are highly sensitive devices, use label-free detection, provide a fast signal response, have easy operation, require small sample volume, and possess low-cost mass production of nanoscale device dimensions [50]. Among the conventional methods for graphene production, reduced graphene oxide (rGO) is one of the most employed due to its extensively optimized procedure for high-quality production [50] resulting in a similar electrical performance like pristine graphene but with lower production costs [90]. Because of the characteristics mentioned above, reduced graphene oxide field-effect transistors (rGO-FETs) are suitable for portable point-of-care applications. Furthermore, aptamer receptors modified with a pyrene terminal group can be easily immobilized on these transducers. Due to the aptamer's short length, the receptor-analyte binding occurs within the Debye length of the rGO-FET. Thus, the resulting interactional conformational changes after target binding are adequately sensed by graphene [90,191].

This chapter introduces the rGO-FET-based detection of malaria using the 2008s aptamer as a bioreceptor for PfLDH detection. This aptamer was modified with a pyrene terminal group that allowed its easy immobilization on the transducer by pi-pi staking on the rGO. The enhanced electrical properties of rGO-FET devices by implementing an intense thermal annealing step are demonstrated. The optimization of aptamer immobilization and signal detection together with an AFM and QCM analysis of the surface morphology for each immobilization step, are shown. Finally, the characteristic performance of the generated rGO-FET aptasensor in both PBS buffer and human serum is reported, along with a detailed discussion about the biomolecular sensing mechanism for this rGO-FET aptasensor.

6.1 Field-effect characterization of rGO-FET devices in liquid gate configuration

In section 3.2.3, Figure 3.5 shows an individual chip and a device, respectively. One sensor chip contains 16 sensor positions, and each device has 10 interdigitated electrodes (IDEs) with an effective channel width of $W = 900$ µm and length of $L = 5$ µm. Figure 6.1a depicts the output characteristics (drain current I_D vs. drain voltage V_D) of the reduced graphene oxide FET at ten different gate voltages (V_G). The device demonstrated a clear Ohmic contact from the quilted layer of many tiny rGO flakes in a gate voltage range from -0.6 V to 0.6 V. Figure 6.1b shows the leakage current of the rGO-FET. For signal detection, only changes occurring on the left side of the I_D/V_G plot were considered for following the PfLDH detection since higher leakage

was observed on the right side. Figure 6.1c depicts characteristic transconductance (g) of these devices used later to calculate the carrier mobility. The rGO-FETs stability was evaluated by a long-term stability test recording the signal over 1800 s (Figure 6.1d). The devices were tested in PBS buffer with ionic strength of 115 mM.

Rapid thermal annealing (RTA) was chosen to reduce the GO because of its potential in processing larger areas and efficient reduction in a controlled environment compatible with lithography process-flows [192,193]. Besides, implemented extreme thermal annealing conditions (750 °C for 4 s) allowed to obtain devices that perform more like pristine graphene, showing ambipolar characteristics (Figure 6.2a). Their Dirac point (V_{Dirac}) was with 0.1 V, very close to the ideal 0 V and even closer than the V_{Dirac} of FET reported devices utilizing chemical-vapor deposited graphene (CVD) and exfoliated graphene [194–196].

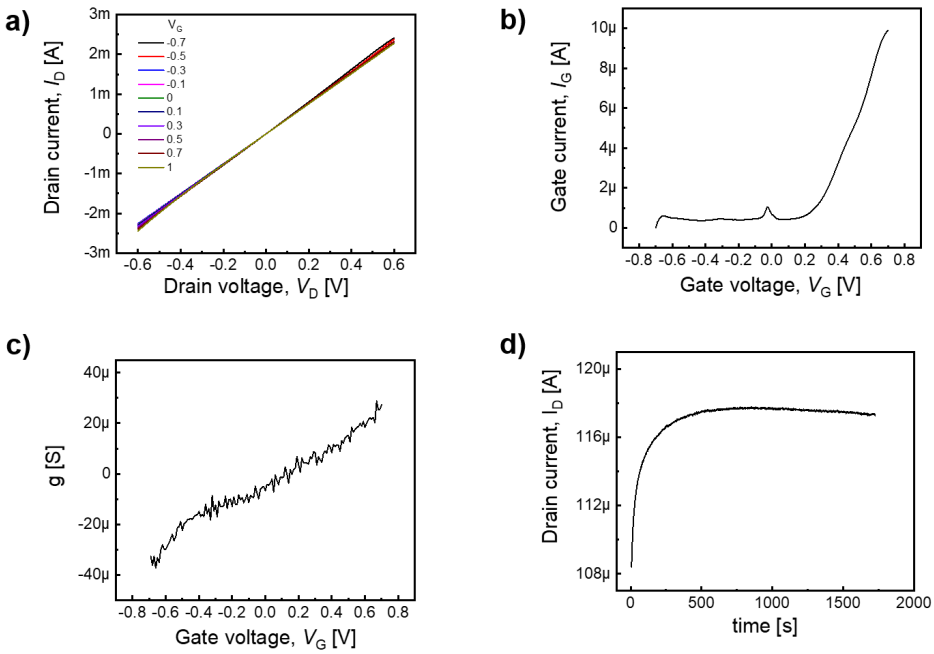

Figure 6.1 rGO-FET output characteristics. a) Ohmic output of the transistor device under different applied gate voltages, b) leakage current, c) transconductance (g), and d) time-trace stability.

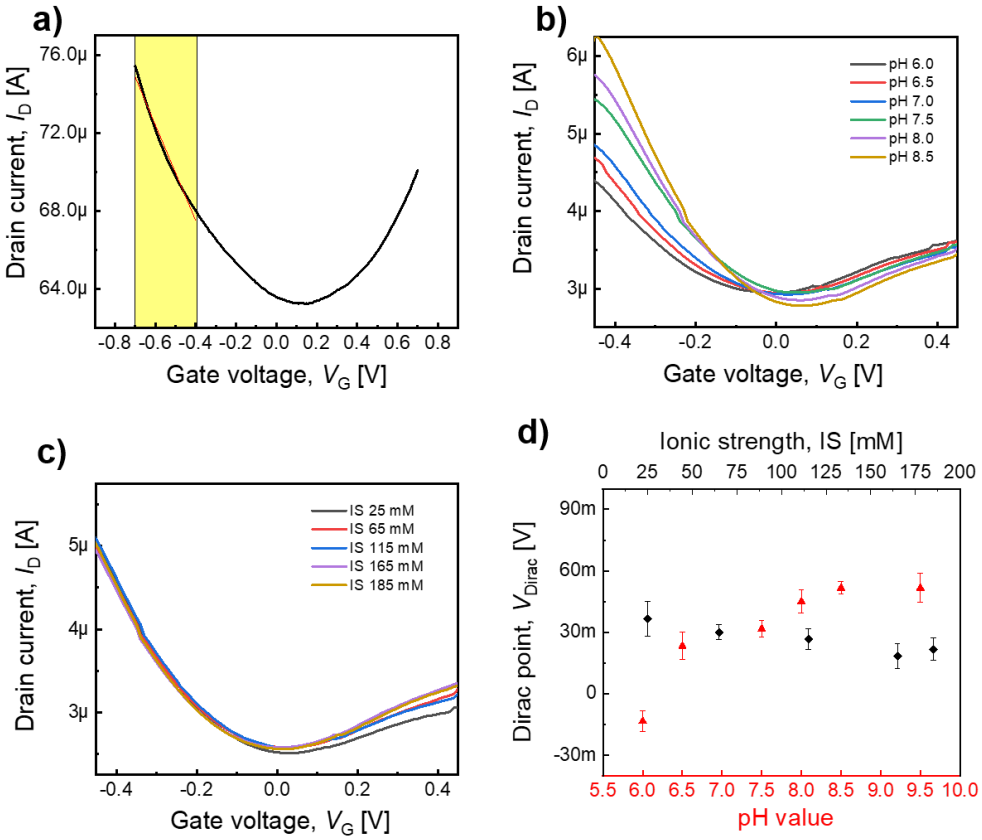

Figure 6.2 a) Field-effect behavior of an rGO-FET in a range of ± 0.7 V_G and a bias drain voltage (V_D) of 0.1 V. b) The graph depicts the pH-dependent field-effect behaviour, recorded for a typical device with a bias drain voltage (V_D) of 0.1 V while gate voltage (V_G) at the reference electrode is swept between ± 0.6 V. The graph shows the pH behaviour of the sensor, where the Dirac point shifts towards positive gate voltages with an increase of buffer pH. b) Ionic strength dependent behaviour of a typical rGO-FET device with a buffer solution of ionic strength ranging from 25 mM up to 185 mM with the same drain-source bias and V_G settings. c) The movement in the Dirac point against different pH and ionic strength solutions.

Moreover, their transconductance (g) and carrier mobility (µ) have been improved three orders of magnitude compared with previously fabricated rGO-FET devices with less intense RTA treatment [50]. The g for electrons and holes were determined from the first derivative of the field-effect transport curves at 0.6 V (Figure 6.2a). The obtained transconductance for hole and electron were g_h = 30.0±1.6 µS and g_e = 18.4±0.8 µS. The field-effect electron and hole mobilities were calculated from the electron and hole dominant transport regions using Equation 2.18. The effective length of the channel was 5 µm, the drain-source bias (V_D) in this case was 0.1 V, and the calculated electrical double-layer capacitance (C_{edl}, Eq. 2.19) was

700.0 μF from an also calculated dielectric constant (λ_D, Eq. 2.20) of 0.89 nm in 115 mM ionic strength electrolyte. Hence, the obtained hole and electron mobilities were μ_h = 213.4 $cm^2\ V^{-1}\ s^{-1}$ and μ_e = 131.0 $cm^2\ V^{-1}\ s^{-1}$.

Figure 6.2b depicts the device response, according to the Dirac point voltage, under different pH solutions. The Dirac point was obtained from the minimum of the quadratic function fit to the experimental data. The Dirac point moves towards positive voltages by increasing the pH from 6 to 8.5. Similar behaviour for other rGO-FET devices at different pH solutions was reported in the literature [86,110,197,198]. This shift indicates that the transistor can be sensitive to charged molecules that approach the rGO surface, which is essential for detecting biomolecules. The change in the Dirac-minimum corresponded to a linear dependence on the pH value and changed in the pH window from 6 to 8.5 by 23 mV/pH, a similar value as reported in other works [86,198]. The Dirac point voltage at different ionic strengths suggests a much smaller variation in a range from 25 mM to 184 mM (Figure 6.3c and 6.3d), corroborating other reports [110,197,199]. That indicates that the electrostatic gating is not strongly affected by changes of the ionic strength present in the solution but instead to charged molecules as observed for pH. These characteristic results were even similar to studies based on CVD graphene devices [112,200]. Figure 2.12 of section 2.4 depicts the schematic model representation of the electrostatic potential at the rGO-electrolyte interface. Such model explains the effect of the electrolyte pH and the ionic strength on the field-effect characteristics of the rGO devices. The model also includes the composition (such as permittivity and thickness) of the biofunctional layers on rGO-FETs. Based on this model, the effect of electrolyte pH and ionic strength on the rGO devices can be evaluated and later related to the biosensor operation for DNA-target binding experiments.

6.2 rGO-FET aptasensor performance for PfLDH detection

Figure 6.3a shows the configuration in a classical field-effect transistor (FET) used to characterize the aptasensor performance. Before the characterization of the rGO-FET aptasensor performance, the immobilization time of the pyrene-modified aptamer on the surface of the rGO was optimized. The optimization of the aptamer density on the transducer is not only essential to assure a high signal response of the biosensor by providing a sufficient number of receptors, but also to avoid an excess of molecules on the rGO-FET surface that could inhibit the analyte binding by steric and electrostatic repulsion. Thus, different incubation times of 1 μM pyrene-terminated aptamer were tested (Figure 6.3b). In the graph, the drain current

change is plotted versus the different concentrations of PfLDH. As can be observed, the 72 h incubation did not show any response due to the possible high-density of aptamer molecules. Even at some point, some electrodes' gating effect was lost, and it was impossible to measure anything. When reducing to 24 h of immobilization, the drain current signal was improved, and with 16 h (overnight) incubation, the signal was even further increased. Thus, the overnight incubation was selected to perform the further aptasensor characterization. According to the time-trace stability test, the signal acquisition reached a stability plateau after 5 min of protein addition (Figure 6.3c). Thus, this resting time after analyte addition was selected for further aptasensor characterization.

The aptamer immobilization and protein detection were also characterized by AFM measurements (Figure 6.4). One silicon (Si) chip covered with rGO on top was analyzed before (Figure 6.4a), and after the aptamer immobilization (Figure 6.4b), and subsequently after protein binding (Figure 6.4c). Only minor differences in RMS surface roughness (0.48±0.03 nm) and topographical height (1.03±0.01 nm) were detected after aptamer immobilization due to the intrinsic roughness (0.38±0.03 nm) and topographical height (1.01±0.01 nm) characteristics of the bare chip. This indicates that the aptamer receptors form a relatively homogeneous and compact film, following the topography of the underlying substrate. However, significant morphological changes were observed after the protein addition. This apparent change resulted from the fact that the protein has a bigger size than the aptamer. The calculated surface roughness was 0.94±0.01 nm, and the topographical height was 4.14±0.47 nm (Table 6.2).

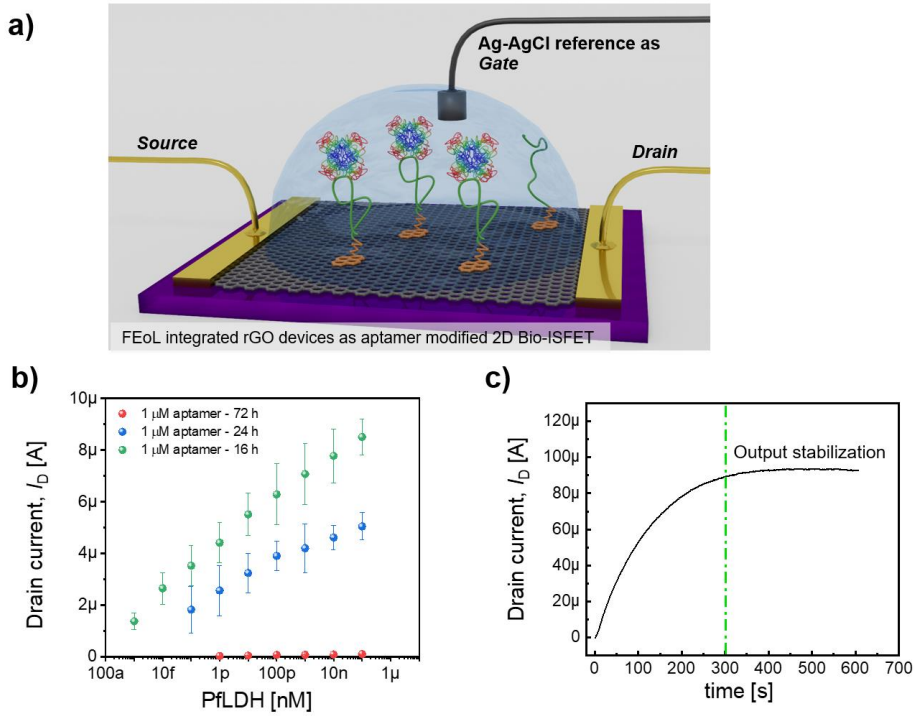

Figure 6.3 a) Bio-FET configuration of an rGOFET aptasensor. b) Optimization of the time immobilization of pyrene-terminated aptamer on the rGO surface. c) Time-trace stability test of rGO-FET aptasensor after 10 nM PfLDH addition.

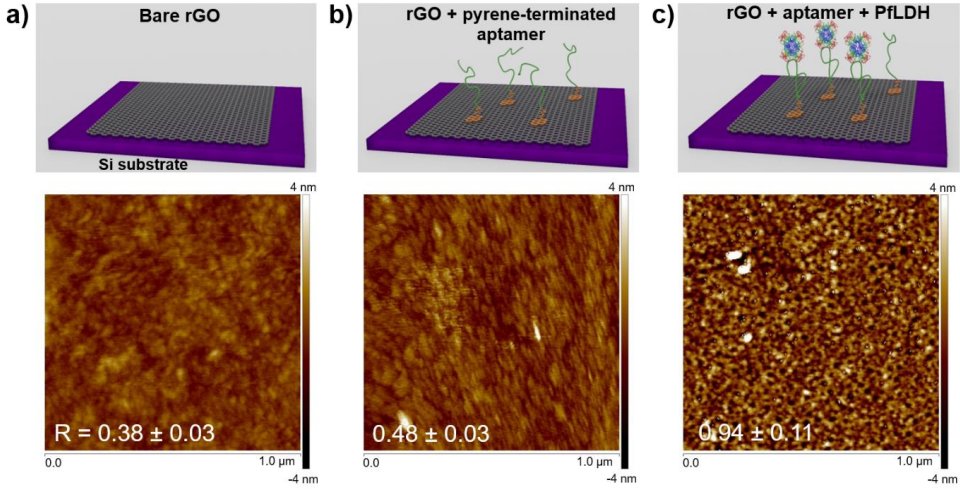

Figure 6.4 AFM characterization of the stepwise rGO-FET aptasensor preparation and protein detection. a) Bare rGO, b) surface after pyrene-terminated aptamer immobilization, and c) after PfLDH target binding. R: RMS roughness.

Table 6.1 Analysis of surface characterization by AFM for stepwise rGO-FET aptasensor preparation and target detection.

	Roughness 1µm / nm	Height ([§]m) / nm	Height / nm
Bare rGO	0.38±0.03	1.02±0.05	1.01±0.01
Aptamer	0.48±0.03	1.05±0.06	1.03±0.01
PfLDH protein	0.94±0.11	4.45±0.80	4.14±0.47

[§] m: manually determined from the cross-section.

A second characterization method for stepwise aptasensor preparation and target detection was done by QCM-D (see section 2.5.1). First, the immobilization of the pyrene-terminated aptamer was investigated (Figure 6.5). Interestingly, the immobilization of the aptamer was only possible using high salt PBS buffer (1 M NaCl) when the aptamer was contained in low salt concentration PBS buffer (0.1 M NaCl) no apparent immobilization was observed (Appendix B, Figure S8). That could be explained due to the high repulsion between the negatively charged DNA aptamer strands, thus, the high salt concentration buffer can effectively screen those charges making possible the immobilization by pi-pi interaction of the pyrene group with the graphene. The obtained frequency change (Δf) due to aptamer immobilization was 7.86 Hz, and the associated shift in dissipation (ΔD) was 0.8. Subsequently, the electrode was blocked with BSA with a further high Δf = 9.92 Hz and ΔD = 0.05 because of the size of such blocking protein. The PfLDH detection was followed with a smaller Δf = 0.82 Hz and ΔD = 0.19 for 10 nM concentration, but with further higher Δf = 4.93 Hz and ΔD = 0.52 for 50 nM PfLDH.

Figure 6.6a shows the decrement recorded of the I_D current versus the swept V_G potential at ±0.7 V and a V_D bias of 0.1 V with a concentration range from 1 fM to 100 nM of PfLDH. It is worth mentioning that only after the addition of protein, a decrement of I_D was observed. Figure 6.6a depicts the stability of the sensor by a recorded field-effect curve after aptamer immobilization (apt) and a second measurement after 20 min (apt + 20 min). The original and repeatedly measured curves perfectly matched.

The calibration curve obtained as a percentage of the relative drain current change ($\frac{\Delta I_D}{I_{D0}}$) by a change in the protein concentration was determined at -0.6 V_G (Figure 6.6b). The mean values were obtained from 3 different chips and at least eight different rGO-FET devices from each chip (n = 24). The obtained plot was fit by a Langmuir-Freundlich adsorption isotherm (Eq. 2.1) to describe this aptasensor performance quantitatively.

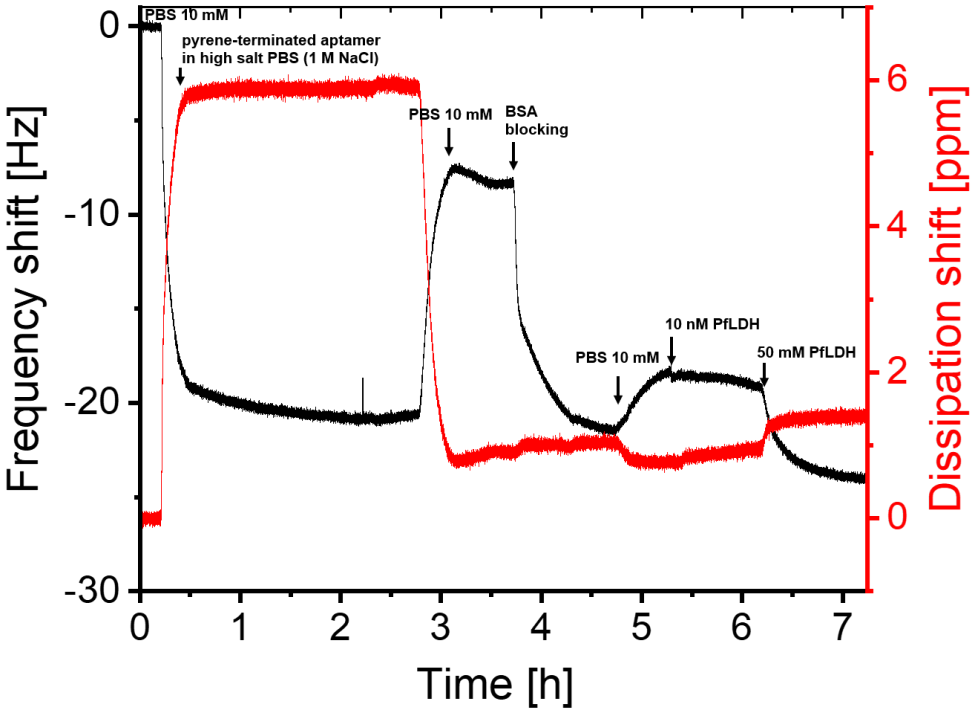

Figure 6.5 QCM-D measurement for pyrene-terminal aptamer immobilization on graphene and PfLDH detection at 10 and 50 nM concentration.

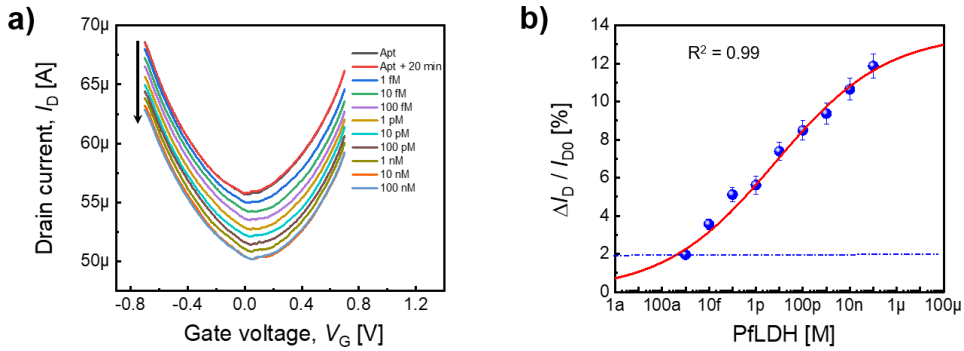

Figure 6.6 a) Concentration-dependent transfer characteristics of the rGO-FET after aptamer immobilization (apt), 20 min resting time (apt + 20 min), and for the target PfLDH protein detection in a concentrations range between 1 fM and 100 nM. The potential of -0.6 V was used to calculate the change of the current signal I_D as a function of the increment of PfLDH concentration. b) Calibration curve obtained as the relative percentage of the change in the drain current ($\Delta I_D/I_{D0}$).

The fit to the experimental data resulted in the following parameter values of the maximum signal at $(\frac{\Delta I_D}{I_{D0}})_{max}$ = 13.6 % in good agreement with the value observed with the maximum concentration tested here (100 nM) closer to such saturation value; k_D = 3.6 pM, and n = 0.22. ($\frac{\Delta I_D}{I_{D0}}$) was linearly proportional to the log concentration of PfLDH in a dynamic range from 1 fM to 100 nM (Figure 6.6b). The obtained sensitivity (S) was smaller (1.3/decade) as compared with the previously developed impedimetric biosensors implementing this 2008s aptamer (8.3/decade) [24,29]. However, the calculated limit of detection (LOD) was the smallest (0.78 fM) for this rGO-FET sensing platform as compared to the previously developed ones. This enhanced detection performance might be a result of the high-quality GO solution obtained [50] and the extreme thermal annealing implementation, which improved the properties of the rGO, as previously discussed. This improvement of the rGO performance facilitated the detection of the PfLDH concentration at the subfemtomolar level, which has been possible only in fM range for other developed optical and electrochemical aptasensors utilizing exclusively the 2008s aptamer as receptor molecule (Table 6.3).

Table 6.2 Comparison of the performance of different aptasensors based on 2008s aptamer as receptor for PfLDH detection in biological samples.

Detection platform	Blocker	Limit of detection	Sensitivity	Dynamic range of detection	Reference
APTEC (colorimetric)	BSA	35.7 pM	---	35.7 pM – 35.7 nM	[201]
Plasmon-enhanced fluorescence	BSA	18 fM	---	10 fM – 1 nM	[202]
Gold rod (EIS)	MCH	1.3 pM	8.3/decade	10 pM – 10 nM	[29]
Gold rod (EIS)	PEG	800 fM	7.9/decade	1 pM – 100 nM	[24]
hAu (EIS/SPP)	MCH	1.4 pM 23.5 nM	2.4/decade 2.2/decade	1 pM – 100 nM 23.5 nM – >1 μM	[203]
flex-MEA (DPV)	PEG	7.3 fM	1.9/decade	7.3 fM – 10 nM	**Chapter 5 work**
rGOFET (FET)	BSA	0.8 fM	1.3/decade	1 fM –100 nM	**Present work**

EIS: electrochemical impedance spectroscopy; DPV: differential pulse voltammetry; APTEC: Aptamer-Tethered Enzyme Capture.

The reported detected concentration of PfLDH had been found between a few pM to hundreds of nM corresponding to a parasitemia ranging from 0.0001 % to 0.1 % [8,167,168]. Hence, this highly sensitive and easily handled biosensor gives a significant advantage for detecting even lower-density parasitemia in communities with endemic *P. falciparum* infections and asymptomatic cases, discarding the possibility of false-negative results.

The sensing mechanism for most FET-based biosensors (BioFET) involves changes due to the intrinsic net charges of the target biomolecules, which alter the FET-electrolyte electrochemical interface (see section 2.4 and Figure 6.7a). Therefore, another analysis that can be done is the investigation of the Dirac point change (Figure 6.7b). A negative shift of the Dirac point after aptamer immobilization was observed. This shift was associated with the negative charges on the DNA aptamer strands, which induce an electrostatic gating. In the case of proteins, the net charge is determined by their isoelectric point (pI) value. When the pI value is higher than the buffer pH, the protein developed a positive net charge. In particular, PfLDH proteins (pI = 8.0) are positively charged at the physiological pH (pH = 7.5) [204]. PfLDH binding to aptamers is equivalent to applying a small positive bias and effectively shifting the Dirac point towards positive V_G. The extent of the shift is correlated with the net charge of the molecule and the protein coverage (Figure 6.6a and 6.7b).

However, the absolute change of V_{Dirac} was smaller as compared to the shift after aptamer immobilization. This smaller change might be a consequence of a lower net charge of the protein in comparison with the oligoanionic DNA and the fact that not every receptor on the surface binds a PfLDH molecule. However, an additional phenomenon needs to be considered, PfLDH with an estimated size of 7.5 nm increases thichness upon binding to aptamers depending on their concentration and binding sites available. A PfLDH concentration increase, therefore results in continuous increase of biomoleculas tickness (Fig. 6.7). An increase in thickness results in capacitance decrease associated with a gradual loss of field-effect in the rGO-FET aptasensor.

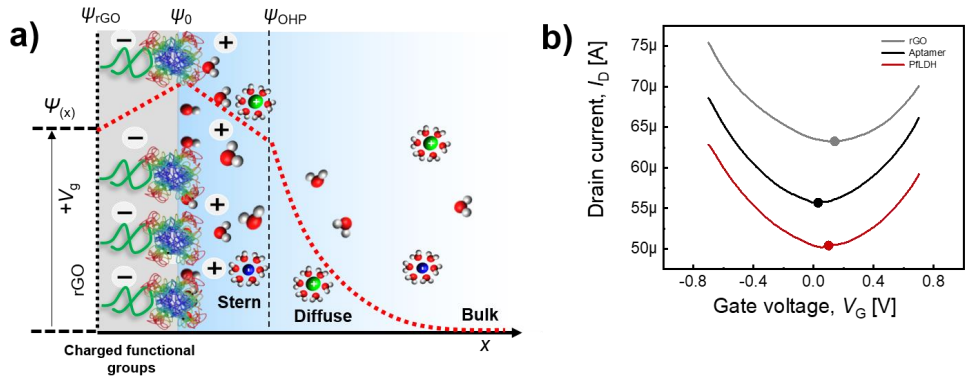

Figure 6.7 Operation of aptamer-modified rGO-FETs with solid-liquid interface model. a) Illustration of the aptamer modified rGO-electrolyte electrochemical interface containing aptamers as negatively charged biofunctional layer and PfLDH as positive layer forming the stern layer and diffused layer. b) Dirac point shift towards negative potential after aptamer immobilization (black dot) compared with bare rGO (gray dot), and positive potential shift after PfLDH detection (red dot). ψ_{rGO}: electrostatic potential of the rGO; ψ_0: electrostatic potential at the rGO-electrolyte interface; ψ_{OHP}:potential at the outer Helmholtz Plane (OHP).

Figure 6.9a demonstrates the specific signal detected for the target protein compared with the human LDHB, the analog protein of PfLDH. The small-signal detection for hLDHB could be associated with possible adsorption of the protein on the rGO surface. During the SELEX process to obtain the aptamer, a selectivity versus human LDH was established already by a counter target selection of the aptamer [14]. The 2008s aptamer binding specificity is dictated by extensive interactions of one of the aptamer loops with a PfLDH epitope absent in human lactate dehydrogenase. This type of noise signal caused by non-specific binding is typically observed in aptamer-based FET sensors. The interference caused by non-specific binding can be reduced by controlled passivation of the free receptor surface, e.g., by blocking with BSA, hydrophobic alkanethiols, or hydrophilic protein-repellent PEG molecules [34,39,90,195].

In the same regard, a control experiment was carried out to prove that the detected signal change occurred because of the specific interaction between the 2008s aptamer and the PfLDH. Hence, a prostate-specific antigen (PSA) aptamer, which has been reported as being highly-specific for such antigens, was employed as control (Figure 6.9b). The small unspecificity observed might also be related to the same fact of adsorption of proteins on the electrode's free-receptor surface. However, a higher signal was obtained with the 2008s aptamer, demonstrating the selective and specific signal obtained only for the 2008s aptamer-PfLDH complex with this rGO-FET transducer.

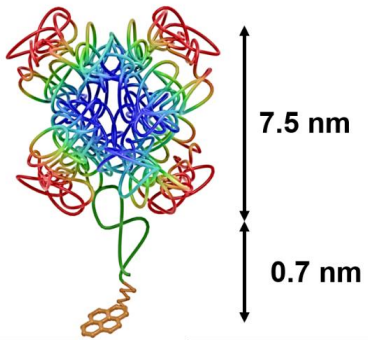

Figure 6.8 Structure of the 2008s DNA aptamer comprising a β-helical stem structure in complex with the PfLDH protein.

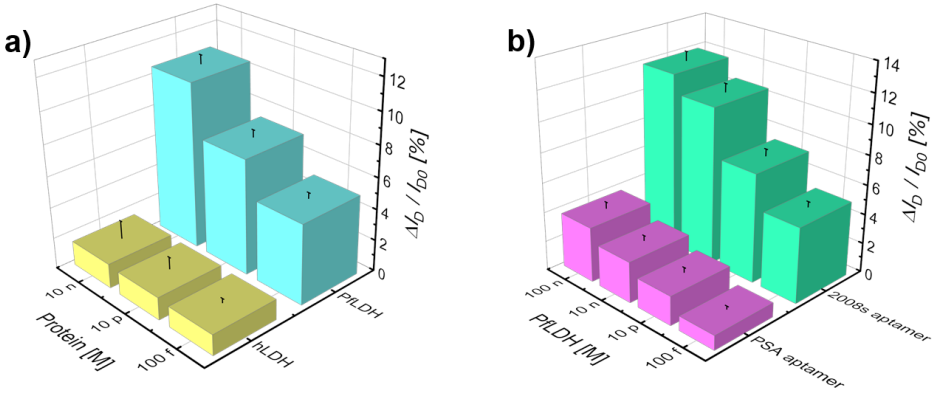

Figure 6.9 a) Selective PfLDH detection, by 2008s aptamer, proved versus its analogous protein human LDH at three different concentrations for both proteins (100 fM, 10 pM, and 10 nM). b) The experiment showed the higher specific signal detected by 2008s aptamer for PfLDH compared with a control aptamer for prostate-specific antigens.

6.3 PfLDH detection in human serum

The results from the rGO-FET aptasensor performance test in human serum (HS) are shown in Figure 6.10 and summarized in Table 6.4. A blocking step with BSA was implemented in these experiments to avoid the small unspecific adsorption registered with the control experiments. The PfLDH detection was performed in 10 % HS solutions. The concentrations of PfLDH tested were in a regimen according to the previously determined calibration curve and reported assays with patient samples [201], covering low 10 fM and 10 pM, medium 10 nM, and high concentration for 100 nM.

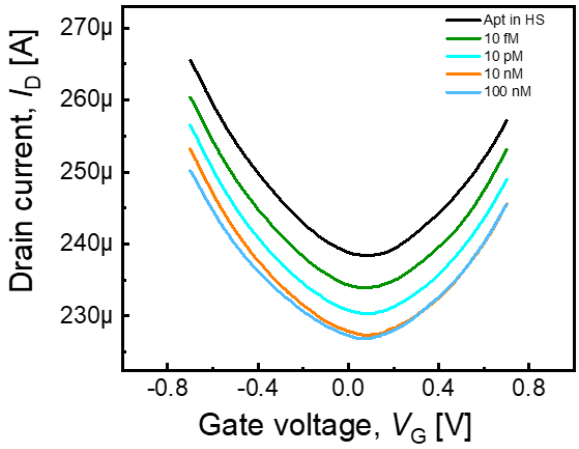

Figure 6.10 PfLDH detection in human serum (HS) at low (10 fM and 10 pM), medium (10 nM) and high (100 nM) concentrations.

Table 6.3 Results of the detection of PfLDH at the rGO-FET chip in human serum by the standard addition method.

Added PfLDH	Found PfLDH	Recovery (%)
10 fM	10,6 ± 1,3 fM	106,0 ± 13
10 pM	9,7 ± 0,2 pM	96,6 ± 2,4
10 nM	10,2 ± 1,1 nM	102,0 ± 11
100 nM	83,8 ± 2,0 nM	83,8 ± 2,0

The precise recoveries observed for the PfLDH detection in the serum samples are associated with the highly specific 2008s aptamer used that binds selectively to the target protein and the implementation of the blocking free-receptor surface with BSA. Thus, this rGO-FET aptasensor showed to be sensitive still at femtomolar concentration even in a complex matrix like human serum.

These conducted experiments showed outstanding and reliable performance of this rGO-FET aptasensor as an excellent candidate for point-of-care sensitive malaria detection.

Chapter 7

Conclusions and Outlook

This thesis focuses on the fabrication of an electrochemical aptasensor for highly sensitive, selective, and discriminatory malaria detection. For the high selectivity, the blocking molecule was first optimized and characterized in terms of the kind of molecule used and the incubation conditions for obtaining optimal signals with the aptasensor in biological fluids. For highly sensitive detection, two different transducer platforms were used. The first is based on flexible multielectrode array (flex-MEA) sensors, and the second on reduced graphene oxide field-effect transistor (rGO-FET). For the highly discriminatory detection of malaria, the flex-MEA sensor platform was implemented to fabricate a multi-target aptasensor.

Firstly, the reduction of non-specific adsorption and enhancement of PfLDH detection was achieved in a complex matrix such as human serum by optimizing the newly implemented PEG blocking molecule' incubation time. Impedance investigations, together with AFM characterization, XPS, contact angle, and QCM-D analysis, suggested that PEG's overall density did not distinctly change for different incubation times, but the morphology of the mixed receptor layer did. In fact, the incubation time significantly influences the aptamer/PEG system by cleaving weak bonds between ssDNA chains and Au, lifting the aptamer molecules driven by the covalent adsorption of PEG molecules. This liberation of the receptor strands enhanced the target binding capability of the sensor for short incubation times. However, after 9 hours of incubation and longer, declining sensor signals were observed, assigned to a phase separation between aptamer and PEG molecules. AFM investigations suggest that the phase separation locally increased the aptamer density and thereby degrades their binding capability to PfLDH due to a restricted conformational degree of freedom. Comparing the calibration curves of aptasensors using hydrophobic MCH or hydrophilic PEG revealed that the blocking molecule had no impact on the sensor sensitivity but strongly enhances the matrix tolerance, the dynamic range, and the limit of detection. The PEG/aptamer receptor system worked reliably in 50% diluted and full serum for *in situ* and *ex situ* detection, respectively, and reached its optimal working conditions after 7 h PEG incubation time. That represents a remarkable

improvement towards the desired *in situ* detection for point-of-care testing. A further improvement, in terms of the long-term storage of the aptasensor, can be achieved by implementing multi-thiol anchoring groups that might prevent the phase separation observed at long incubation times and enhance the target detection in full blood or human serum samples [171].

Subsequently, the detection was translated from the single gold macro electrode to a gold multielectrode array chip fabricated on a flexible PET substrate. The realization of the flex-MEAs was done in collaboration with the Master project of Song Chen. First, a mechanical bending test proved the mechanical robustness of the polymer-based device. This flex-MEA endured more than 1000 bending cycles without changing its electrochemical performance. The flexible PET substrate allowed to partially divide the MEA chip into four sets of electrodes to easily realize the immobilization of four different aptamer receptors: 2008s, pL1, LDHp11, and 2106s for simultaneous multi-target detection. The first three target PfLDH and the last one HRP-2, both main malaria biomarkers. The excellent detection performance of this multi-target aptasensor was demonstrated by spiking the protein analytes PfLDH and HRP-2 in blood samples. For both PfLDH and HRP-2, the obtained detection was highly sensitive in a broad range from 0.15 pM to 100 nM and 4.26 pM to 100 nM, respectively. Those lower detection values obtained with this flex-MEA aptasensor were three and two orders of magnitude smaller for pLDH and HRP-2 detection, respectively, than for the reported commercial best-in-class malaria RDTs. The multi-target flex-MEA aptasensor detection was finally challenged by blood samples with spiked *Plasmodium falciparum* parasites and *Plasmodium falciparum* parasite cultures with different percentages of parasitemia. Interestingly, the obtained sensitivities and specificities in the *Plasmodium falciparum* parasite culture samples were higher than for the blood samples with spiked *Plasmodium falciparum* parasites. The sensitivities obtained for different aptamers fulfilled and even outperformed the requirements set by the world health organization with values higher than >75 % for 50 parasites/ µL (0.001 % parasitemia). In the case of the specificities, those were slightly smaller than the required >90 %, with values of 81.8, 80.0, 87.5, and 83.3 % for 2008s, pL1, and LDHp11 aptamers. Nonetheless, this parameter, according to the WHO, does not represent a critical performance factor as the sensitivity does as stated by WHO: “sometimes it may be more important to have very high sensitivity even at the expense of high specificity, as a missed parasitemia may lead to the death of a patient" [190]. This developed flex-MEA multi-target aptasensor is the first RDT to combine the signal from four different malaria detection receptors to provide a high signal

redundancy and test reliability together with excellent detection performance in *Plasmodium falciparum* parasitized samples at low parasite densities.

Finally, the aptasensor detection was also translated to a second detection platform, utilizing a reduced graphene oxide field-effect transistor (rGO-FET). This aptasensor was realized by implementing a pyrene-modified 2008s aptamer as a receptor molecule. The improved FET characteristics of the rGO-FETs were achieved by implementing an extreme thermal annealing step in the fabrication. Optimization of the aptamer density was carried out by measuring the sensor response for timely-dependent prepared biofunctional layers. It was found that overnight (16 h) aptamer incubation was suitable for PfLDH binding, obtaining high signals with this rGO-FETs. Furthermore, an updated model for the electrical transduction mechanism for PfLDH binding on to the aptamer modified rGO-FET showed that changes in the biofunctional layer thickness and surface charges have a distinguishable influence on the electrical behavior. All this optimization, together with the improved performance of the rGO-FET transducer, allowed sensing the target PfLDH protein as low as subfemtomolar concentration. The dynamic range covered from 1 fM to 100 nM concentration was detected in both PBS buffer and human serum. The specific signal obtained from the 2008s aptamer binding to PfLDH was also demonstrated versus the human LDH and a control aptamer (PSA aptamer). All these demonstrated experiments showed excellent performance and the reliable application of this rGO-FET aptasensor as an excellent candidate for point-of-care sensitive malaria detection. A further improvement regarding the small observed unspecificity can be realized by implementing other blocking molecules, like a pyrene-terminated PEG, which might inhibit unspecific binding on the electrode as shown with the gold electrodes to detect the target in highly concentrated or full serum samples. Even, also the realization of a multi-target aptasensor on this transducer can be envisioned with the help of a micro-spotting device that locally distributes the different aptamer solutions on the different rGO-FET devices of the same chip.

In my opinion, the future work for the development of this malaria biosensor, and in general of any biosensor, should be guided towards the combination with a microfluidic setup for two reasons: reduction of sample volume and required time for the detection. With such device development and the still suggested molecule optimizations, like the dithiol aptamers, it is anticipated that either of the developed RDTs can serve as a useful and sensitive diagnostic tool for improving the diagnosis, disease management, surveillance, and treatment of malaria, particularly in remote and developing areas of the world.

References

[1] World Malaria Report 2020, (n.d.). https://www.who.int/teams/global-malaria-programme/reports/world-malaria-report-2020 (accessed January 4, 2021).

[2] L.L. Fox, T.E. Taylor, P. Pensulo, A. Liomba, A. Mpakiza, A. Varela, S.J. Glover, M.J. Reeves, K.B. Seydel, Histidine-Rich Protein 2 Plasma Levels Predict Progression to Cerebral Malaria in Malawian Children With Plasmodium falciparum Infection, J. Infect. Dis. 208 (2013) 500–503. https://doi.org/10.1093/infdis/jit176.

[3] N.J. White, S. Pukrittayakamee, T.T. Hien, M.A. Faiz, O.A. Mokuolu, A.M. Dondorp, Malaria, The Lancet. 383 (2014) 723–735. https://doi.org/10.1016/S0140-6736(13)60024-0.

[4] D.D. Jr, F. Dl, Splenectomy for the massively enlarged spleen., Am. Surg. 57 (1991) 108–113.

[5] D. House, J. Wain, V.A. Ho, T.S. Diep, N.T. Chinh, P.V. Bay, H. Vinh, M. Duc, C.M. Parry, G. Dougan, N.J. White, T.T. Hien, J.J. Farrar, Serology of Typhoid Fever in an Area of Endemicity and Its Relevance to Diagnosis, J. Clin. Microbiol. 39 (2001) 1002–1007. https://doi.org/10.1128/JCM.39.3.1002-1007.2001.

[6] K.R. Tan, P.M. Arguin, Chapter 21 - Malaria Diagnosis and Treatment, in: C.A. Sanford, P.S. Pottinger, E.C. Jong (Eds.), Travel Trop. Med. Man. Fifth Ed., Elsevier, 2017: pp. 300–314. https://doi.org/10.1016/B978-0-323-37506-1.00021-0.

[7] WHO | Guidelines for the treatment of malaria. Third edition, WHO. (n.d.). http://www.who.int/malaria/publications/atoz/9789241549127/en/ (accessed August 28, 2020).

[8] A. Moody, Rapid Diagnostic Tests for Malaria Parasites, Clin. Microbiol. Rev. 15 (2002) 66–78. https://doi.org/10.1128/CMR.15.1.66-78.2002.

[9] A. Jimenez, R.R. Rees-Channer, R. Perera, D. Gamboa, P.L. Chiodini, I.J. González, A. Mayor, X.C. Ding, Analytical sensitivity of current best-in-class malaria rapid diagnostic tests, Malar. J. 16 (2017) 128. https://doi.org/10.1186/s12936-017-1780-5.

[10] F.D. Krampa, Y. Aniweh, P. Kanyong, G.A. Awandare, Recent Advances in the Development of Biosensors for Malaria Diagnosis, Sensors. 20 (2020) 799. https://doi.org/10.3390/s20030799.

[11] J.C. Mouatcho, J.P.D. Goldring, Malaria rapid diagnostic tests: challenges and prospects, J. Med. Microbiol. 62 (2013) 1491–1505. https://doi.org/10.1099/jmm.0.052506-0.

[12] K.V. Ragavan, S. Kumar, S. Swaraj, S. Neethirajan, Advances in biosensors and optical assays for diagnosis and detection of malaria, Biosens. Bioelectron. 105 (2018) 188–210. https://doi.org/10.1016/j.bios.2018.01.037.

[13] Malaria rapid diagnostic test performance: summary results of WHO product testing of malaria RDTs: round 1-8 (2008–2018), (n.d.) 44.

[14] Y.-W. Cheung, J. Kwok, A.W.L. Law, R.M. Watt, M. Kotaka, J.A. Tanner, Structural basis for discriminatory recognition of Plasmodium lactate dehydrogenase by a DNA aptamer, Proc. Natl. Acad. Sci. 110 (2013) 15967–15972. https://doi.org/10.1073/pnas.1309538110.

[15] S. Lee, K.-M. Song, W. Jeon, H. Jo, Y.-B. Shim, C. Ban, A highly sensitive aptasensor towards Plasmodium lactate dehydrogenase for the diagnosis of malaria, Biosens. Bioelectron. 35 (2012) 291–296. https://doi.org/10.1016/j.bios.2012.03.003.

[16] K.-A. Frith, R. Fogel, J.P.D. Goldring, R.G.E. Krause, M. Khati, H. Hoppe, M.E. Cromhout, M. Jiwaji, J.L. Limson, Towards development of aptamers that specifically bind to lactate dehydrogenase of Plasmodium falciparum through epitopic targeting, Malar. J. 17 (2018) 191. https://doi.org/10.1186/s12936-018-2336-z.

[17] S. Song, L. Wang, J. Li, C. Fan, J. Zhao, Aptamer-based biosensors, TrAC Trends Anal. Chem. 27 (2008) 108–117. https://doi.org/10.1016/j.trac.2007.12.004.
[18] K. Han, Z. Liang, N. Zhou, Design Strategies for Aptamer-Based Biosensors, Sensors. 10 (2010) 4541–4557. https://doi.org/10.3390/s100504541.
[19] I.C. Baines, P. Colas, Peptide aptamers as guides for small-molecule drug discovery, Drug Discov. Today. 11 (2006) 334–341. https://doi.org/10.1016/j.drudis.2006.02.007.
[20] S. Reverdatto, D.S. Burz, A. Shekhtman, Peptide Aptamers: Development and Applications, Curr. Top. Med. Chem. 15 (2015) 1082–1101.
[21] F. Hoppe-Seyler, K. Butz, Peptide aptamers: powerful new tools for molecular medicine, J. Mol. Med. 78 (2000) 426–430. https://doi.org/10.1007/s001090000140.
[22] Y.-W. Cheung, P. Röthlisberger, A.E. Mechaly, P. Weber, F. Levi-Acobas, Y. Lo, A.W.C. Wong, A.B. Kinghorn, A. Haouz, G.P. Savage, M. Hollenstein, J.A. Tanner, Evolution of abiotic cubane chemistries in a nucleic acid aptamer allows selective recognition of a malaria biomarker, Proc. Natl. Acad. Sci. 117 (2020) 16790–16798. https://doi.org/10.1073/pnas.2003267117.
[23] G. Dutta, Electrochemical biosensors for rapid detection of malaria, Mater. Sci. Energy Technol. 3 (2020) 150–158. https://doi.org/10.1016/j.mset.2019.10.003.
[24] G. Figueroa-Miranda, C. Wu, Y. Zhang, L. Nörbel, Y. Lo, J.A. Tanner, L. Elling, A. Offenhäusser, D. Mayer, Polyethylene glycol-mediated blocking and monolayer morphology of an electrochemical aptasensor for malaria biomarker detection in human serum, Bioelectrochemistry. 136 (2020) 107589. https://doi.org/10.1016/j.bioelechem.2020.107589.
[25] S. Banerjee, M. Nilsen-Hamilton, Aptamers for Infectious Disease Diagnosis, E Coli Infect. - Importance Early Diagn. Effic. Treat. (2019). https://doi.org/10.5772/intechopen.86945.
[26] J.D. Ospina-Villa, C. López-Camarillo, C.A. Castañón-Sánchez, J. Soto-Sánchez, E. Ramírez-Moreno, L.A. Marchat, Advances on Aptamers against Protozoan Parasites, Genes. 9 (2018) 584. https://doi.org/10.3390/genes9120584.
[27] P. Jain, B. Chakma, S. Patra, P. Goswami, Potential Biomarkers and Their Applications for Rapid and Reliable Detection of Malaria, BioMed Res. Int. 2014 (2014) e852645. https://doi.org/10.1155/2014/852645.
[28] L. Vivas, A. Easton, H. Kendrick, A. Cameron, J.-L. Lavandera, D. Barros, F.G. de las Heras, R.L. Brady, S.L. Croft, Plasmodium falciparum: Stage specific effects of a selective inhibitor of lactate dehydrogenase, Exp. Parasitol. 111 (2005) 105–114. https://doi.org/10.1016/j.exppara.2005.06.007.
[29] G. Figueroa-Miranda, L. Feng, S.C.-C. Shiu, R.M. Dirkzwager, Y.-W. Cheung, J.A. Tanner, M.J. Schöning, A. Offenhäusser, D. Mayer, Aptamer-based electrochemical biosensor for highly sensitive and selective malaria detection with adjustable dynamic response range and reusability, Sens. Actuators B Chem. 255 (2018) 235–243. https://doi.org/10.1016/j.snb.2017.07.117.
[30] A. Anne, C. Demaille, J. Moiroux, Terminal Attachment of Polyethylene Glycol (PEG) Chains to a Gold Electrode Surface. Cyclic Voltammetry Applied to the Quantitative Characterization of the Flexibility of the Attached PEG Chains and of Their Penetration by Mobile PEG Chains, Macromolecules. 35 (2002) 5578–5586. https://doi.org/10.1021/ma020071d.
[31] P. Harder, M. Grunze, R. Dahint, G.M. Whitesides, P.E. Laibinis, Molecular Conformation in Oligo(ethylene glycol)-Terminated Self-Assembled Monolayers on Gold and Silver Surfaces Determines Their Ability To Resist Protein Adsorption, J. Phys. Chem. B. 102 (1998) 426–436. https://doi.org/10.1021/jp972635z.

[32] N. Liu, Z. Xu, A. Morrin, X. Luo, Low fouling strategies for electrochemical biosensors targeting disease biomarkers, Anal. Methods. 11 (2019) 702–711. https://doi.org/10.1039/C8AY02674B.
[33] K. Emoto, J.M. Harris, J.M. Van Alstine, Grafting Poly(ethylene glycol) Epoxide to Amino-Derivatized Quartz: Effect of Temperature and pH on Grafting Density, Anal. Chem. 68 (1996) 3751–3757. https://doi.org/10.1021/ac960114m.
[34] N.M. Andoy, M.S. Filipiak, D. Vetter, Ó. Gutiérrez-Sanz, A. Tarasov, Graphene Biosensors: Graphene-Based Electronic Immunosensor with Femtomolar Detection Limit in Whole Serum (Adv. Mater. Technol. 12/2018), Adv. Mater. Technol. 3 (2018) 1870046. https://doi.org/10.1002/admt.201870046.
[35] P. Li, K. Greben, R. Wördenweber, U. Simon, A. Offenhäusser, D. Mayer, Tuning neuron adhesion and neurite guiding using functionalized AuNPs and backfill chemistry, RSC Adv. 5 (2015) 39252–39262. https://doi.org/10.1039/C5RA06901G.
[36] X. Luo, Q. Xu, T. James, J.J. Davis, Redox and Label-Free Array Detection of Protein Markers in Human Serum, Anal. Chem. 86 (2014) 5553–5558. https://doi.org/10.1021/ac5010037.
[37] A. Q. Tran, C. Kaulen, U. Simon, A. Offenhäusser, D. Mayer, Surface coupling strength of gold nanoparticles affects cytotoxicity towards neurons, Biomater. Sci. 5 (2017) 1051–1060. https://doi.org/10.1039/C7BM00054E.
[38] S. Schilp, A. Rosenhahn, M.E. Pettitt, J. Bowen, M.E. Callow, J.A. Callow, M. Grunze, Physicochemical Properties of (Ethylene Glycol)-Containing Self-Assembled Monolayers Relevant for Protein and Algal Cell Resistance, Langmuir. 25 (2009) 10077–10082. https://doi.org/10.1021/la901038g.
[39] X. Wang, Y. Zhu, T.R. Olsen, N. Sun, W. Zhang, R. Pei, Q. Lin, A graphene aptasensor for biomarker detection in human serum, Electrochimica Acta. 290 (2018) 356–363. https://doi.org/10.1016/j.electacta.2018.08.062.
[40] N. Cennamo, L. Pasquardini, F. Arcadio, L.E. Vanzetti, A.M. Bossi, L. Zeni, D-shaped plastic optical fibre aptasensor for fast thrombin detection in nanomolar range, Sci. Rep. 9 (2019) 18740. https://doi.org/10.1038/s41598-019-55248-x.
[41] N. Hui, X. Sun, S. Niu, X. Luo, PEGylated Polyaniline Nanofibers: Antifouling and Conducting Biomaterial for Electrochemical DNA Sensing, ACS Appl. Mater. Interfaces. 9 (2017) 2914–2923. https://doi.org/10.1021/acsami.6b11682.
[42] K. Kaneko, M. Hara, T. Nishino, T. Maruyama, One-step biotinylation of cellulose paper by polymer-coating to prepare a paper-based analytical device, Anal. Chem. (2019). https://doi.org/10.1021/acs.analchem.9b04373.
[43] G. Wang, Q. Xu, L. Liu, X. Su, J. Lin, G. Xu, X. Luo, Mixed Self-Assembly of Polyethylene Glycol and Aptamer on Polydopamine Surface for Highly Sensitive and Low-Fouling Detection of Adenosine Triphosphate in Complex Media, ACS Appl. Mater. Interfaces. 9 (2017) 31153–31160. https://doi.org/10.1021/acsami.7b09529.
[44] T. Zhang, Z. Xu, H. Xu, Y. Gu, Y. Xing, X. Yan, H. Liu, N. Lu, Y. Song, S. Zhang, Z. Zhang, M. Yang, Catechol and zwitterion-bifunctionalized poly(ethylene glycol) based ultrasensitive antifouling electrochemical aptasensor for the quantification of adenosine triphosphate in biological media, Sens. Actuators B Chem. 288 (2019) 469–475. https://doi.org/10.1016/j.snb.2019.03.027.
[45] C. Wu, A. Offenhäusser, D. Mayer, A Highly Sensitive Amperometric Aptamer Biosensor for Adenosine Triphosphate Detection on a 64 Channel Gold Multielectrode Array, Phys. Status Solidi A. 217 (2020) 1900925. https://doi.org/10.1002/pssa.201900925.
[46] Y. Liu, Y. Liu, Z. Matharu, A. Rahimian, A. Revzin, Detecting multiple cell-secreted cytokines from the same aptamer-functionalized electrode, Biosens. Bioelectron. 64 (2015) 43–50. https://doi.org/10.1016/j.bios.2014.08.034.

[47] Y. Zhang, G. Figueroa-Miranda, C. Wu, D. Willbold, A. Offenhäusser, D. Mayer, Electrochemical dual-aptamer biosensors based on nanostructured multielectrode arrays for the detection of neuronal biomarkers, Nanoscale. (2020). https://doi.org/10.1039/D0NR03421E.
[48] S. Lee, K.-M. Song, W. Jeon, H. Jo, Y.-B. Shim, C. Ban, A highly sensitive aptasensor towards Plasmodium lactate dehydrogenase for the diagnosis of malaria, Biosens. Bioelectron. 35 (2012) 291–296. https://doi.org/10.1016/j.bios.2012.03.003.
[49] J.A. Tanner, Y.W. Cheung, M. Kotaka, Nucleic acid aptamers against plasmodium lactate dehydrogenase and histidine-rich protein II and uses thereof for malaria diagnosis, US9000137B2, 2015. https://patents.google.com/patent/US9000137B2/en (accessed January 5, 2021).
[50] X. Lu, W.-M. Munief, F. Heib, M. Schmitt, A. Britz, S. Grandthyl, F. Müller, J.-U. Neurohr, K. Jacobs, H.M. Benia, R. Lanche, V. Pachauri, R. Hempelmann, S. Ingebrandt, Front-End-of-Line Integration of Graphene Oxide for Graphene-Based Electrical Platforms, Adv. Mater. Technol. 3 (2018) 1700318. https://doi.org/10.1002/admt.201700318.
[51] T. Hianik, J. Wang, Electrochemical Aptasensors – Recent Achievements and Perspectives, Electroanalysis. 21 (2009) 1223–1235. https://doi.org/10.1002/elan.200904566.
[52] W. Zhou, P.-J.J. Huang, J. Ding, J. Liu, Aptamer-based biosensors for biomedical diagnostics, Analyst. 139 (2014) 2627–2640. https://doi.org/10.1039/C4AN00132J.
[53] A.E.G. Cass, Y. Zhang, Nucleic acid aptamers: ideal reagents for point-of-care diagnostics?, Faraday Discuss. 149 (2013) 49–61. https://doi.org/10.1039/C005487A.
[54] Y.-W. Cheung, J. Kwok, A.W.L. Law, R.M. Watt, M. Kotaka, J.A. Tanner, Structural basis for discriminatory recognition of Plasmodium lactate dehydrogenase by a DNA aptamer, Proc. Natl. Acad. Sci. 110 (2013) 15967–15972. https://doi.org/10.1073/pnas.1309538110.
[55] D. Irvine, C. Tuerk, L. Gold, Selexion, J. Mol. Biol. 222 (1991) 739–761. https://doi.org/10.1016/0022-2836(91)90509-5.
[56] J.A. Tanner, A.B. Kinghorn, Y.-W. Cheung, Aptamers, MDPI, 2018.
[57] T.J. Macke, D.A. Case, Modeling Unusual Nucleic Acid Structures, in: Mol. Model. Nucleic Acids, American Chemical Society, 1997: pp. 379–393. https://doi.org/10.1021/bk-1998-0682.ch024.
[58] R. Renneberg, F. Lisdat, eds., Biosensing for the 21st Century, Springer Berlin Heidelberg, Berlin, Heidelberg, 2008. https://doi.org/10.1007/978-3-540-75201-1.
[59] D.R. Thevenot, K. Tóth, R.A. Durst, G.S. Wilson, Electrochemical Biosensors: Recommended Definitions and Classification, Pure Appl. Chem. 71 (1999) 2333–2348. https://doi.org/10.1351/pac199971122333.
[60] W. Dias da Silva, D.V. Tambourgi, IgY: A promising antibody for use in immunodiagnostic and in immunotherapy, Vet. Immunol. Immunopathol. 135 (2010) 173–180. https://doi.org/10.1016/j.vetimm.2009.12.011.
[61] M. Tini, U.R. Jewell, G. Camenisch, D. Chilov, M. Gassmann, Generation and application of chicken egg-yolk antibodies, Comp. Biochem. Physiol. A. Mol. Integr. Physiol. 131 (2002) 569–574. https://doi.org/10.1016/S1095-6433(01)00508-6.
[62] M.-E. Park, S.-Y. Lee, R.-H. Kim, M.-K. Ko, K.-N. Lee, S.-M. Kim, B.-K. Kim, J.-S. Lee, B. Kim, J.-H. Park, Enhanced immune responses of foot-and-mouth disease vaccine using new oil/gel adjuvant mixtures in pigs and goats, Vaccine. 32 (2014) 5221–5227. https://doi.org/10.1016/j.vaccine.2014.07.040.

[63] G.R. Bishop, J. Ren, B.C. Polander, B.D. Jeanfreau, J.O. Trent, J.B. Chaires, Energetic basis of molecular recognition in a DNA aptamer, Biophys. Chem. 126 (2007) 165–175. https://doi.org/10.1016/j.bpc.2006.07.009.
[64] P. Jorgensen, L. Chanthap, A. Rebueno, R. Tsuyuoka, D. Bell, Malaria Rapid Diagnostic Tests in Tropical Climates: The Need for a Cool Chain, Am. J. Trop. Med. Hyg. 74 (2006) 750–754.
[65] A.A. Lubin, K.W. Plaxco, Folding-Based Electrochemical Biosensors: The Case for Responsive Nucleic Acid Architectures, Acc. Chem. Res. 43 (2010) 496–505. https://doi.org/10.1021/ar900165x.
[66] E.T.S.G. da Silva, D.E.P. Souto, J.T.C. Barragan, J. de F. Giarola, A.C.M. de Moraes, L.T. Kubota, Electrochemical Biosensors in Point-of-Care Devices: Recent Advances and Future Trends, ChemElectroChem. 4 (2017) 778–794. https://doi.org/10.1002/celc.201600758.
[67] A. Dhiman, P. Kalra, V. Bansal, John.G. Bruno, T.K. Sharma, Aptamer-based point-of-care diagnostic platforms, Sens. Actuators B Chem. 246 (2017) 535–553. https://doi.org/10.1016/j.snb.2017.02.060.
[68] N.Y. Adly, B. Wolfrum, M. Spehr, Inkjet-printed electrochemical devices for bioelectronics, 2018.
[69] Biosensors: an Introduction, Springer-Verlag, 2013.
[70] N. Ayawei, A.N. Ebelegi, D. Wankasi, Modelling and Interpretation of Adsorption Isotherms, J. Chem. 2017 (2017) 3039817. https://doi.org/10.1155/2017/3039817.
[71] D.A. Armbruster, T. Pry, Limit of Blank, Limit of Detection and Limit of Quantitation, Clin. Biochem. Rev. 29 (2008) S49–S52.
[72] C.M. Pandey, B.D. Malhotra, Biosensors: Fundamentals and Applications, Walter de Gruyter GmbH & Co KG, 2019.
[73] G. Evtugyn, A. Porfireva, M. Ryabova, T. Hianik, Aptasensor for Thrombin Based on Carbon Nanotubes-Methylene Blue Composites, Electroanalysis. 20 (2008) 2310–2316. https://doi.org/10.1002/elan.200804345.
[74] W. Wen, T. Bao, J. Yang, M.-Z. Zhang, W. Chen, H.-Y. Xiong, X.-H. Zhang, Y.-D. Zhao, S.-F. Wang, A novel amperometric adenosine triphosphate biosensor by immobilizing graphene/dual-labeled aptamers complex onto poly(o-phenylenediamine) modified electrode, Sens. Actuators B Chem. 191 (2014) 695–702. https://doi.org/10.1016/j.snb.2013.10.061.
[75] H. Pei, F. Li, Y. Wan, M. Wei, H. Liu, Y. Su, N. Chen, Q. Huang, C. Fan, Designed Diblock Oligonucleotide for the Synthesis of Spatially Isolated and Highly Hybridizable Functionalization of DNA–Gold Nanoparticle Nanoconjugates, J. Am. Chem. Soc. 134 (2012) 11876–11879. https://doi.org/10.1021/ja304118z.
[76] S.M. Schreiner, D.F. Shudy, A.L. Hatch, A. Opdahl, L.J. Whitman, D.Y. Petrovykh, Controlled and Efficient Hybridization Achieved with DNA Probes Immobilized Solely through Preferential DNA-Substrate Interactions, Anal. Chem. 82 (2010) 2803–2810. https://doi.org/10.1021/ac902765g.
[77] K. Maehashi, T. Katsura, K. Kerman, Y. Takamura, K. Matsumoto, E. Tamiya, Label-Free Protein Biosensor Based on Aptamer-Modified Carbon Nanotube Field-Effect Transistors, Anal. Chem. 79 (2007) 782–787. https://doi.org/10.1021/ac060830g.
[78] K. Maehashi, K. Matsumoto, Y. Takamura, E. Tamiya, Aptamer-Based Label-Free Immunosensors Using Carbon Nanotube Field-Effect Transistors, Electroanalysis. 21 (2009) 1285–1290. https://doi.org/10.1002/elan.200804552.
[79] T. Hianik, A. Porfireva, I. Grman, G. Evtugyn, EQCM Biosensors Based on DNA Aptamers and Antibodies for Rapid Detection of Prions, (2009). https://doi.org/info:doi/10.2174/092986609787848090.

[80] T. Hianik, A. Porfireva, I. Grman, G. Evtugyn, Aptabodies - New Type of Artificial Receptors for Detection Proteins, (2008). https://doi.org/info:doi/10.2174/092986608785203656.
[81] X. Lu, A. Miodek, W.-M. Munief, P. Jolly, V. Pachauri, X. Chen, P. Estrela, S. Ingebrandt, Reduced graphene-oxide transducers for biosensing applications beyond the Debye-screening limit, Biosens. Bioelectron. 130 (2019) 352–359. https://doi.org/10.1016/j.bios.2018.09.045.
[82] R.J. White, N. Phares, A.A. Lubin, Y. Xiao, K.W. Plaxco, Optimization of Electrochemical Aptamer-Based Sensors via Optimization of Probe Packing Density and Surface Chemistry, Langmuir. 24 (2008) 10513–10518. https://doi.org/10.1021/la800801v.
[83] R. Lao, S. Song, H. Wu, L. Wang, Z. Zhang, L. He, C. Fan, Electrochemical Interrogation of DNA Monolayers on Gold Surfaces, Anal. Chem. 77 (2005) 6475–6480. https://doi.org/10.1021/ac050911x.
[84] J.A. Hansen, J. Wang, A.-N. Kawde, Y. Xiang, K.V. Gothelf, G. Collins, Quantum-Dot/Aptamer-Based Ultrasensitive Multi-Analyte Electrochemical Biosensor, J. Am. Chem. Soc. 128 (2006) 2228–2229. https://doi.org/10.1021/ja060005h.
[85] A.R. Lokanathan, S. Zhang, V.R. Regina, M.A. Cole, R. Ogaki, M. Dong, F. Besenbacher, R.L. Meyer, P. Kingshott, Mixed poly (ethylene glycol) and oligo (ethylene glycol) layers on gold as nonfouling surfaces created by backfilling, Biointerphases. 6 (2011) 180–188. https://doi.org/10.1116/1.3647506.
[86] C. Reiner-Rozman, M. Larisika, C. Nowak, W. Knoll, Graphene-based liquid-gated field effect transistor for biosensing: Theory and experiments, Biosens. Bioelectron. 70 (2015) 21–27. https://doi.org/10.1016/j.bios.2015.03.013.
[87] Z. Hao, Y. Zhu, X. Wang, P.G. Rotti, C. DiMarco, S.R. Tyler, X. Zhao, J.F. Engelhardt, J. Hone, Q. Lin, Real-Time Monitoring of Insulin Using a Graphene Field-Effect Transistor Aptameric Nanosensor, ACS Appl. Mater. Interfaces. 9 (2017) 27504–27511. https://doi.org/10.1021/acsami.7b07684.
[88] S. Farid, X. Meshik, M. Choi, S. Mukherjee, Y. Lan, D. Parikh, S. Poduri, U. Baterdene, C.-E. Huang, Y.Y. Wang, P. Burke, M. Dutta, M.A. Stroscio, Detection of Interferon gamma using graphene and aptamer based FET-like electrochemical biosensor, Biosens. Bioelectron. 71 (2015) 294–299. https://doi.org/10.1016/j.bios.2015.04.047.
[89] S. Mukherjee, X. Meshik, M. Choi, S. Farid, D. Datta, Y. Lan, S. Poduri, K. Sarkar, U. Baterdene, C.-E. Huang, Y.Y. Wang, P. Burke, M. Dutta, M.A. Stroscio, A Graphene and Aptamer Based Liquid Gated FET-Like Electrochemical Biosensor to Detect Adenosine Triphosphate, IEEE Trans. NanoBioscience. 14 (2015) 967–972. https://doi.org/10.1109/TNB.2015.2501364.
[90] C.R. Tamanaha, A Survey of Graphene-Based Field Effect Transistors for Bio-sensing, in: C. Kranz (Ed.), Carbon-Based Nanosensor Technol., Springer International Publishing, Cham, 2019: pp. 165–200. https://doi.org/10.1007/5346_2017_12.
[91] Methods in Microbiology, Academic Press, 1972.
[92] C.G. Zoski, Handbook of Electrochemistry, Elsevier, 2006.
[93] Electrochemical Methods: Fundamentals and Applications, 2nd Edition | Wiley, Wiley.Com. (n.d.). https://www.wiley.com/en-us/Electrochemical+Methods%3A+Fundamentals+and+Applications%2C+2nd+Edition-p-9780471043720 (accessed May 2, 2020).
[94] B.-Y. Chang, S.-M. Park, Electrochemical Impedance Spectroscopy, Annu. Rev. Anal. Chem. 3 (2010) 207–229. https://doi.org/10.1146/annurev.anchem.012809.102211.

[95] D.D. Macdonald, Reflections on the history of electrochemical impedance spectroscopy, Electrochimica Acta. 51 (2006) 1376–1388. https://doi.org/10.1016/j.electacta.2005.02.107.
[96] T. Bertok, L. Lorencova, E. Chocholova, E. Jane, A. Vikartovska, P. Kasak, J. Tkac, Electrochemical Impedance Spectroscopy Based Biosensors: Mechanistic Principles, Analytical Examples and Challenges towards Commercialization for Assays of Protein Cancer Biomarkers, ChemElectroChem. 6 (2019) 989–1003. https://doi.org/10.1002/celc.201800848.
[97] O. Pänke, T. Balkenhohl, J. Kafka, D. Schäfer, F. Lisdat, Impedance Spectroscopy and Biosensing, in: R. Renneberg, F. Lisdat (Eds.), Biosensing 21st Century, Springer Berlin Heidelberg, 2007: pp. 195–237. https://doi.org/10.1007/10_2007_081.
[98] A.A. Moya, Identification of characteristic time constants in the initial dynamic response of electric double layer capacitors from high-frequency electrochemical impedance, J. Power Sources. 397 (2018) 124–133. https://doi.org/10.1016/j.jpowsour.2018.07.015.
[99] P.R.F. Rocha, P. Schlett, U. Kintzel, V. Mailänder, L.K.J. Vandamme, G. Zeck, H.L. Gomes, F. Biscarini, D.M. de Leeuw, Electrochemical noise and impedance of Au electrode/electrolyte interfaces enabling extracellular detection of glioma cell populations, Sci. Rep. 6 (2016) srep34843. https://doi.org/10.1038/srep34843.
[100] V.M. Mirsky, Ultrathin Electrochemical Chemo- and Biosensors: Technology and Performance, Springer Science & Business Media, 2013.
[101] 11.4: Voltammetric Methods, Chem. Libr. (2013). https://chem.libretexts.org/Under_Construction/Purgatory/Book%3A_Analytical_Chemistry_2.0_(Harvey)/11_Electrochemical_Methods/11.4%3A_Voltammetric_Methods (accessed May 7, 2020).
[102] F.A. Settle, Handbook of Instrumental Techniques for Analytical Chemistry, Prentice Hall PTR, 1997.
[103] Principles of voltammetry and microelectrode surface states. - Abstract - Europe PMC, (n.d.). https://europepmc.org/article/med/8412305 (accessed May 7, 2020).
[104] Administrator, Linear Sweep and Cyclic Voltametry: The Principles, (2013). https://www.ceb.cam.ac.uk/research/groups/rg-eme/Edu/linear-sweep-and-cyclic-voltametry-the-principles (accessed May 7, 2020).
[105] J. Zhang, S. Song, L. Wang, D. Pan, C. Fan, A gold nanoparticle-based chronocoulometric DNA sensor for amplified detection of DNA, Nat. Protoc. 2 (2007) 2888–2895. https://doi.org/10.1038/nprot.2007.419.
[106] D. Grieshaber, R. MacKenzie, J. Vörös, E. Reimhult, Electrochemical Biosensors - Sensor Principles and Architectures, Sensors. 8 (2008) 1400–1458. https://doi.org/10.3390/s80314000.
[107] S.M. Sze, K.Ng. Kwok, Physics of Semiconductor Devices, John Wiley & Sons, Inc., Hoboken, New Jersey, 2007. https://doi.org/10.1002/0470068329.
[108] D. Kireev, A. Offenhäusser, J.L. Fitter, Graphene Devices for Extracellular Measurements, Forschungszentrum Jülich GmbH, Zentralbibliothek, Jülich, 2017.
[109] Graphene based Materials for Bioelectronics and Healthcare, Mater. Res. Forum. (n.d.). https://www.mrforum.com/product/9781644900376-6/ (accessed February 2, 2021).
[110] R. Lanche, V. Pachauri, W.-M. Munief, A. Müller, M. Schwartz, P. Wagner, R. Thoelen, S. Ingebrandt, Graphite oxide electrical sensors are able to distinguish single nucleotide polymorphisms in physiological buffers, FlatChem. 7 (2018) 1–9. https://doi.org/10.1016/j.flatc.2017.12.001.
[111] I. Heller, S. Chatoor, J. Männik, M.A.G. Zevenbergen, C. Dekker, S.G. Lemay, Influence of Electrolyte Composition on Liquid-Gated Carbon Nanotube and Graphene

Transistors, J. Am. Chem. Soc. 132 (2010) 17149–17156. https://doi.org/10.1021/ja104850n.
[112] L. Zuccaro, J. Krieg, A. Desideri, K. Kern, K. Balasubramanian, Tuning the isoelectric point of graphene by electrochemical functionalization, Sci. Rep. 5 (2015) 11794. https://doi.org/10.1038/srep11794.
[113] B. Scientific, QCM-D | Measurements, (n.d.). https://www.biolinscientific.com/measurements/qcm-d (accessed May 7, 2020).
[114] Amplified QCM-D biosensor for protein based on aptamer-functionalized gold nanoparticles, Biosens. Bioelectron. 26 (2010) 575–579. https://doi.org/10.1016/j.bios.2010.07.034.
[115] Q. Chen, W. Tang, D. Wang, X. Wu, N. Li, F. Liu, Amplified QCM-D biosensor for protein based on aptamer-functionalized gold nanoparticles, Biosens. Bioelectron. 26 (2010) 575–579. https://doi.org/10.1016/j.bios.2010.07.034.
[116] G. Sauerbrey, Verwendung von Schwingquarzen zur Wägung dünner Schichten und zur Mikrowägung, Z. Für Phys. 155 (1959) 206–222. https://doi.org/10.1007/BF01337937.
[117] P. van der Heide, X-ray Photoelectron Spectroscopy: An introduction to Principles and Practices, John Wiley & Sons, 2011.
[118] J. Qu, H.M. Meyer, X-Ray Photoelectron Spectroscopy (XPS), in: Q.J. Wang, Y.-W. Chung (Eds.), Encycl. Tribol., Springer US, Boston, MA, 2013: pp. 4133–4138. https://doi.org/10.1007/978-0-387-92897-5_1222.
[119] T. Huhtamäki, X. Tian, J.T. Korhonen, R.H.A. Ras, Surface-wetting characterization using contact-angle measurements, Nat. Protoc. 13 (2018) 1521–1538. https://doi.org/10.1038/s41596-018-0003-z.
[120] B. Scientific, Contact Angle | Measurements | Biolin Scientific, (n.d.). https://www.biolinscientific.com/measurements/contact-angle (accessed May 8, 2020).
[121] P. Eaton, P. West, Atomic Force Microscopy, Oxford University Press, 2010.
[122] G. Haugstad, Atomic Force Microscopy: Understanding Basic Modes and Advanced Applications, John Wiley & Sons, 2012.
[123] Modos topográficos, Coursera. (n.d.). https://www.coursera.org/learn/tecnicas-microscopicas-caracterizacion/home/welcome (accessed May 13, 2020).
[124] Atomic Force Microscopy Working Principle — AFM Explained - Nanosurf, (n.d.). https://www.nanosurf.com/en/support/afm-operating-principle (accessed May 13, 2020).
[125] Y. Zhang, G. Figueroa-Miranda, Z. Lyu, C. Zafiu, D. Willbold, A. Offenhäusser, D. Mayer, Monitoring amyloid-β proteins aggregation based on label-free aptasensor, Sens. Actuators B Chem. 288 (2019) 535–542. https://doi.org/10.1016/j.snb.2019.03.049.
[126] F. Schröper, D. Brüggemann, Y. Mourzina, B. Wolfrum, A. Offenhäusser, D. Mayer, Analyzing the electroactive surface of gold nanopillars by electrochemical methods for electrode miniaturization, Electrochimica Acta. 53 (2008) 6265–6272. https://doi.org/10.1016/j.electacta.2008.03.068.
[127] L.E. Delle, V. Pachauri, S. Sharma, O. Shaforost, H. Ma, M. Adabi, R. Lilischkis, P. Wagner, R. Thoelen, N. Klein, R. O'Kennedy, S. Ingebrandt, ScFv-modified graphene-coated IDE-arrays for 'label-free' screening of cardiovascular disease biomarkers in physiological saline, Biosens. Bioelectron. 102 (2018) 574–581. https://doi.org/10.1016/j.bios.2017.12.005.
[128] H.C. Koydemir, H. Kulah, A. Alp, A.H. Uner, G. Hascelik, C. Ozgen, A Fully Microfabricated Electrochemical Sensor and its Implementation for Detection of Methicillin Resistance in Staphylococcus Aureus, IEEE Sens. J. 14 (2014) 1844–1851. https://doi.org/10.1109/JSEN.2014.2305152.

[129] X. Liu, C. Cheng, J. Wu, S. Eda, Y. Guo, A low cost and palm-size analyzer for rapid and sensitive protein detection by AC electrokinetics capacitive sensing, Biosens. Bioelectron. 90 (2017) 83–90. https://doi.org/10.1016/j.bios.2016.10.098.
[130] X. Liu, K. Yang, A. Wadhwa, S. Eda, S. Li, J. Wu, Development of an AC electrokinetics-based immunoassay system for on-site serodiagnosis of infectious diseases, Sens. Actuators Phys. 171 (2011) 406–413. https://doi.org/10.1016/j.sna.2011.08.007.
[131] T. Bryan, X. Luo, P.R. Bueno, J.J. Davis, An optimised electrochemical biosensor for the label-free detection of C-reactive protein in blood, Biosens. Bioelectron. 39 (2013) 94–98. https://doi.org/10.1016/j.bios.2012.06.051.
[132] R.M. Dirkzwager, S. Liang, J.A. Tanner, Development of Aptamer-Based Point-of-Care Diagnostic Devices for Malaria Using Three-Dimensional Printing Rapid Prototyping, ACS Sens. 1 (2016) 420–426. https://doi.org/10.1021/acssensors.5b00175.
[133] N.K. Singh, P. Jain, S. Das, P. Goswami, Dye Coupled Aptamer-Captured Enzyme Catalyzed Reaction for Detection of Pan Malaria and P. falciparum Species in Laboratory Settings and Instrument-Free Paper-Based Platform, Anal. Chem. 91 (2019) 4213–4221. https://doi.org/10.1021/acs.analchem.9b00670.
[134] M. Xu, X. Luo, J.J. Davis, The label free picomolar detection of insulin in blood serum, Biosens. Bioelectron. 39 (2013) 21–25. https://doi.org/10.1016/j.bios.2012.06.014.
[135] N.K. Singh, S.K. Arya, P. Estrela, P. Goswami, Capacitive malaria aptasensor using Plasmodium falciparum glutamate dehydrogenase as target antigen in undiluted human serum, Biosens. Bioelectron. 117 (2018) 246–252. https://doi.org/10.1016/j.bios.2018.06.022.
[136] N.K. Singh, P.D. Thungon, P. Estrela, P. Goswami, Development of an aptamer-based field effect transistor biosensor for quantitative detection of Plasmodium falciparum glutamate dehydrogenase in serum samples, Biosens. Bioelectron. 123 (2019) 30–35. https://doi.org/10.1016/j.bios.2018.09.085.
[137] B. Chakma, P. Jain, N.K. Singh, P. Goswami, Development of Electrochemical Impedance Spectroscopy Based Malaria Aptasensor Using HRP-II as Target Biomarker, Electroanalysis. 30 (2018) 1847–1854. https://doi.org/10.1002/elan.201800142.
[138] N.K. Singh, B. Chakma, P. Jain, P. Goswami, Protein-Induced Fluorescence Enhancement Based Detection of Plasmodium falciparum Glutamate Dehydrogenase Using Carbon Dot Coupled Specific Aptamer, ACS Comb. Sci. 20 (2018) 350–357. https://doi.org/10.1021/acscombsci.8b00021.
[139] N. Arroyo-Currás, J. Somerson, P.A. Vieira, K.L. Ploense, T.E. Kippin, K.W. Plaxco, Real-time measurement of small molecules directly in awake, ambulatory animals, Proc. Natl. Acad. Sci. 114 (2017) 645–650. https://doi.org/10.1073/pnas.1613458114.
[140] B.S. Ferguson, D.A. Hoggarth, D. Maliniak, K. Ploense, R.J. White, N. Woodward, K. Hsieh, A.J. Bonham, M. Eisenstein, T.E. Kippin, K.W. Plaxco, H.T. Soh, Real-Time, Aptamer-Based Tracking of Circulating Therapeutic Agents in Living Animals, Sci. Transl. Med. 5 (2013) 213ra165-213ra165. https://doi.org/10.1126/scitranslmed.3007095.
[141] Z. Hao, Z. Wang, Y. Li, Y. Zhu, X. Wang, C.G.D. Moraes, Y. Pan, X. Zhao, Q. Lin, Measurement of cytokine biomarkers using an aptamer-based affinity graphene nanosensor on a flexible substrate toward wearable applications, Nanoscale. 10 (2018) 21681–21688. https://doi.org/10.1039/C8NR04315A.
[142] J. Tu, R.M. Torrente-Rodríguez, M. Wang, W. Gao, The Era of Digital Health: A Review of Portable and Wearable Affinity Biosensors, Adv. Funct. Mater. (2019). https://doi.org/10.1002/adfm.201906713.
[143] L. Bezinge, A. Suea-Ngam, A. J. deMello, C.-J. Shih, Nanomaterials for molecular signal amplification in electrochemical nucleic acid biosensing: recent advances and

future prospects for point-of-care diagnostics, Mol. Syst. Des. Eng. (2020). https://doi.org/10.1039/C9ME00135B.
[144] S. Liang, A.B. Kinghorn, M. Voliotis, J.K. Prague, J.D. Veldhuis, K. Tsaneva-Atanasova, C.A. McArdle, R.H.W. Li, A.E.G. Cass, W.S. Dhillo, J.A. Tanner, Measuring luteinising hormone pulsatility with a robotic aptamer-enabled electrochemical reader, Nat. Commun. 10 (2019) 1–10. https://doi.org/10.1038/s41467-019-08799-6.
[145] Y. Hu, B. Liang, L. Fang, G. Ma, G. Yang, Q. Zhu, S. Chen, X. Ye, Antifouling Zwitterionic Coating via Electrochemically Mediated Atom Transfer Radical Polymerization on Enzyme-Based Glucose Sensors for Long-Time Stability in 37 °C Serum, Langmuir. 32 (2016) 11763–11770. https://doi.org/10.1021/acs.langmuir.6b03016.
[146] T. Date, T. Sawada, T. Serizawa, Self-assembled peptides on polymer surfaces: towards morphology-dependent surface functionalization, Soft Matter. 9 (2013) 3469–3472. https://doi.org/10.1039/C3SM27841G.
[147] C.-Y. Lee, P. Gong, G.M. Harbers, D.W. Grainger, D.G. Castner, L.J. Gamble, Surface Coverage and Structure of Mixed DNA/Alkylthiol Monolayers on Gold: Characterization by XPS, NEXAFS, and Fluorescence Intensity Measurements, Anal. Chem. 78 (2006) 3316–3325. https://doi.org/10.1021/ac052137j.
[148] L. Feng, A. Sivanesan, Z. Lyu, A. Offenhäusser, D. Mayer, Electrochemical current rectification–a novel signal amplification strategy for highly sensitive and selective aptamer-based biosensor, Biosens. Bioelectron. 66 (2015) 62–68. https://doi.org/10.1016/j.bios.2014.10.057.
[149] S. Sharma, R.W. Johnson, T.A. Desai, XPS and AFM analysis of antifouling PEG interfaces for microfabricated silicon biosensors, Biosens. Bioelectron. 20 (2004) 227–239. https://doi.org/10.1016/j.bios.2004.01.034.
[150] L. Feng, Z. Lyu, A. Offenhäusser, D. Mayer, Electrochemically triggered aptamer immobilization via click reaction for vascular endothelial growth factor detection, Eng. Life Sci. 16 (2016) 550–559. https://doi.org/10.1002/elsc.201600068.
[151] Y. Xiao, R.Y. Lai, K.W. Plaxco, Preparation of electrode-immobilized, redox-modified oligonucleotides for electrochemical DNA and aptamer-based sensing, Nat. Protoc. 2 (2007) 2875–2880. https://doi.org/10.1038/nprot.2007.413.
[152] N. Cennamo, L. Pasquardini, F. Arcadio, L.E. Vanzetti, A.M. Bossi, L. Zeni, D-shaped plastic optical fibre aptasensor for fast thrombin detection in nanomolar range, Sci. Rep. 9 (2019) 1–9. https://doi.org/10.1038/s41598-019-55248-x.
[153] P. Auroy, L. Auvray, Influence of a Polymer Solution on a Polymer Interface, Macromolecules. 29 (1996) 337–342. https://doi.org/10.1021/ma946421g.
[154] H.B. Lu, C.T. Campbell, D.G. Castner, Attachment of Functionalized Poly(ethylene glycol) Films to Gold Surfaces, Langmuir. 16 (2000) 1711–1718. https://doi.org/10.1021/la990221m.
[155] G. Wang, Q. Xu, L. Liu, X. Su, J. Lin, G. Xu, X. Luo, Mixed Self-Assembly of Polyethylene Glycol and Aptamer on Polydopamine Surface for Highly Sensitive and Low-Fouling Detection of Adenosine Triphosphate in Complex Media, ACS Appl. Mater. Interfaces. 9 (2017) 31153–31160. https://doi.org/10.1021/acsami.7b09529.
[156] J. Piehler, A. Brecht, R. Valiokas, B. Liedberg, G. Gauglitz, A high-density poly(ethylene glycol) polymer brush for immobilization on glass-type surfaces, Biosens. Bioelectron. 15 (2000) 473–481. https://doi.org/10.1016/S0956-5663(00)00104-4.
[157] V.L. Koenig, W.L. Carrier, R.O. Rahn, Viscosity studies on dna and the observation of double-stranded and single-stranded breaks in a 40% dmso-phosphate buffer system, Int. J. Biochem. 5 (1974) 601–611. https://doi.org/10.1016/0020-711X(74)90022-6.

[158] Y. Lin, X. Shen, J. Wang, L. Bao, Z. Zhang, D. Pang, Measuring radial Young's modulus of DNA by tapping mode AFM, Chin. Sci. Bull. 52 (2007) 3189–3192. https://doi.org/10.1007/s11434-007-0475-7.
[159] T. Murugesan, M. Perumalsamy, Densities and Viscosities of Polyethylene Glycol 2000 + Salt + Water Systems from (298.15 to 318.15) K, J. Chem. Eng. Data. 50 (2005) 1290–1293. https://doi.org/10.1021/je050035k.
[160] W.J. Price, S.A. Leigh, S.M. Hsu, T.E. Patten, G. Liu, Measuring the Size Dependence of Young's Modulus Using Force Modulation Atomic Force Microscopy, J. Phys. Chem. A. 110 (2006) 1382–1388. https://doi.org/10.1021/jp0544540.
[161] A.B. Steel, R.L. Levicky, T.M. Herne, M.J. Tarlov, Immobilization of Nucleic Acids at Solid Surfaces: Effect of Oligonucleotide Length on Layer Assembly, Biophys. J. 79 (2000) 975–981. https://doi.org/10.1016/S0006-3495(00)76351-X.
[162] S. Schilp, A. Rosenhahn, M.E. Pettitt, J. Bowen, M.E. Callow, J.A. Callow, M. Grunze, Physicochemical Properties of (Ethylene Glycol)-Containing Self-Assembled Monolayers Relevant for Protein and Algal Cell Resistance, Langmuir. 25 (2009) 10077–10082. https://doi.org/10.1021/la901038g.
[163] H. Wackerbarth, M. Grubb, J. Zhang, A.G. Hansen, J. Ulstrup, Dynamics of Ordered-Domain Formation of DNA fragments on Au(111) with Molecular Resolution, Angew. Chem. Int. Ed. 43 (2004) 198–203. https://doi.org/10.1002/anie.200352146.
[164] G.G. Baralia, A.-S. Duwez, B. Nysten, A.M. Jonas, Kinetics of Exchange of Alkanethiol Monolayers Self-Assembled on Polycrystalline Gold, Langmuir. 21 (2005) 6825–6829. https://doi.org/10.1021/la050245v.
[165] T. Kakiuchi, K. Sato, M. Iida, D. Hobara, S. Imabayashi, K. Niki, Phase Separation of Alkanethiol Self-Assembled Monolayers during the Replacement of Adsorbed Thiolates on Au(111) with Thiols in Solution, Langmuir. 16 (2000) 7238–7244. https://doi.org/10.1021/la991590l.
[166] N. Eliaz, Applications of Electrochemistry and Nanotechnology in Biology and Medicine I, Springer Science & Business Media, 2011.
[167] J.W. Jang, C.H. Cho, E.T. Han, S.S.A. An, C.S. Lim, pLDH level of clinically isolated Plasmodium vivax and detection limit of pLDH based malaria rapid diagnostic test, Malar. J. 12 (2013) 181. https://doi.org/10.1186/1475-2875-12-181.
[168] S.K. Martin, G.-H. Rajasekariah, G. Awinda, J. Waitumbi, C. Kifude, Unified Parasite Lactate Dehydrogenase and Histidine-Rich Protein ELISA for Quantification of Plasmodium falciparum, Am. J. Trop. Med. Hyg. 80 (2009) 516–522.
[169] P. Jain, S. Das, B. Chakma, P. Goswami, Aptamer-graphene oxide for highly sensitive dual electrochemical detection of Plasmodium lactate dehydrogenase, Anal. Biochem. 514 (2016) 32–37. https://doi.org/10.1016/j.ab.2016.09.013.
[170] S. Lee, D.H. Manjunatha, W. Jeon, C. Ban, Cationic Surfactant-Based Colorimetric Detection of Plasmodium Lactate Dehydrogenase, a Biomarker for Malaria, Using the Specific DNA Aptamer, PLOS ONE. 9 (2014) e100847. https://doi.org/10.1371/journal.pone.0100847.
[171] G. Hartwich, M. Schneider, A Tunable and Versatile Anchoring System for Gold-Surfaces, Proceedings. 1 (2017) 742. https://doi.org/10.3390/proceedings1080742.
[172] G. Figueroa-Miranda, S. Chen, M. Neis, L. Zhou, Y. Zhang, Y. Lo, J.A. Tanner, A. Kreidenweiss, A. Offenhäusser, D. Mayer, Multi-target electrochemical malaria aptasensor on flexible multielectrode arrays for detection in malaria parasite blood samples, Sens. Actuators B Chem. 349 (2021) 130812. https://doi.org/10.1016/j.snb.2021.130812.
[173] B. Bachmann, N.Y. Adly, J. Schnitker, A. Yakushenko, P. Rinklin, A. Offenhäusser, B. Wolfrum, All-inkjet-printed gold microelectrode arrays for extracellular recording of

action potentials, Flex. Print. Electron. 2 (2017) 035003. https://doi.org/10.1088/2058-8585/aa7928.
[174] A. Blau, Cell adhesion promotion strategies for signal transduction enhancement in microelectrode array in vitro electrophysiology: An introductory overview and critical discussion, Curr. Opin. Colloid Interface Sci. 18 (2013) 481–492. https://doi.org/10.1016/j.cocis.2013.07.005.
[175] A. Czeschik, A. Offenhäusser, B. Wolfrum, Fabrication of MEA-based nanocavity sensor arrays for extracellular recording of action potentials, Phys. Status Solidi A. 211 (2014) 1462–1466. https://doi.org/10.1002/pssa.201330365.
[176] T.J.J. Hondrich, B. Lenyk, P. Shokoohimehr, D. Kireev, V. Maybeck, D. Mayer, A. Offenhäusser, MEA Recordings and Cell–Substrate Investigations with Plasmonic and Transparent, Tunable Holey Gold, ACS Appl. Mater. Interfaces. 11 (2019) 46451–46461. https://doi.org/10.1021/acsami.9b14948.
[177] J.K.Y. Law, C.K. Yeung, B. Hofmann, S. Ingebrandt, J.A. Rudd, A. Offenhäusser, M. Chan, The use of microelectrode array (MEA) to study the protective effects of potassium channel openers on metabolically compromised HL-1 cardiomyocytes, Physiol. Meas. 30 (2009) 155–167. https://doi.org/10.1088/0967-3334/30/2/004.
[178] V. Maybeck, J. Schnitker, W. Li, M. Heuschkel, A. Offenhäusser, An evaluation of extracellular MEA versus optogenetic stimulation of cortical neurons, Biomed. Phys. Eng. Express. 2 (2016) 055017. https://doi.org/10.1088/2057-1976/2/5/055017.
[179] A. Stett, U. Egert, E. Guenther, F. Hofmann, T. Meyer, W. Nisch, H. Haemmerle, Biological application of microelectrode arrays in drug discovery and basic research, Anal. Bioanal. Chem. 377 (2003) 486–495. https://doi.org/10.1007/s00216-003-2149-x.
[180] S. Weidlich, K.J. Krause, J. Schnitker, B. Wolfrum, A. Offenhäusser, MEAs and 3D nanoelectrodes: electrodeposition as tool for a precisely controlled nanofabrication, Nanotechnology. 28 (2017) 095302. https://doi.org/10.1088/1361-6528/aa57b5.
[181] G. Wrobel, Y. Zhang, H.-J. Krause, N. Wolters, F. Sommerhage, A. Offenhäusser, S. Ingebrandt, Influence of the first amplifier stage in MEA systems on extracellular signal shapes, Biosens. Bioelectron. 22 (2007) 1092–1096. https://doi.org/10.1016/j.bios.2006.03.023.
[182] K.J. Krause, N. Adly, A. Yakushenko, J. Schnitker, D. Mayer, A. Offenhäusser, B. Wolfrum, Influence of Self-Assembled Alkanethiol Monolayers on Stochastic Amperometric On-Chip Detection of Silver Nanoparticles, Anal. Chem. 88 (2016) 3632–3637. https://doi.org/10.1021/acs.analchem.5b04306.
[183] K.J. Krause, A. Yakushenko, B. Wolfrum, Stochastic On-Chip Detection of Subpicomolar Concentrations of Silver Nanoparticles, Anal. Chem. 87 (2015) 7321–7325. https://doi.org/10.1021/acs.analchem.5b01478.
[184] Y. Liang, T. Guo, L. Zhou, A. Offenhäusser, D. Mayer, Label-Free Split Aptamer Sensor for Femtomolar Detection of Dopamine by Means of Flexible Organic Electrochemical Transistors, Materials. 13 (2020) 2577. https://doi.org/10.3390/ma13112577.
[185] J. Schnitker, N. Adly, S. Seyock, B. Bachmann, A. Yakushenko, B. Wolfrum, A. Offenhäusser, Rapid Prototyping of Ultralow-Cost, Inkjet-Printed Carbon Microelectrodes for Flexible Bioelectronic Devices, Adv. Biosyst. 2 (2018) 1700136. https://doi.org/10.1002/adbi.201700136.
[186] W.J. Peveler, M. Yazdani, V.M. Rotello, Selectivity and Specificity: Pros and Cons in Sensing, ACS Sens. 1 (2016) 1282–1285. https://doi.org/10.1021/acssensors.6b00564.
[187] R. Piper, J. Lebras, L. Wentworth, A. Hunt-Cooke, S. Houzé, P. Chiodini, M. Makler, Immunocapture diagnostic assays for malaria using Plasmodium lactate dehydrogenase (pLDH)., Am. J. Trop. Med. Hyg. 60 (1999) 109–118.

[188] M.K. Sharma, V.K. Rao, G.S. Agarwal, G.P. Rai, N. Gopalan, S. Prakash, S.K. Sharma, R. Vijayaraghavan, Highly Sensitive Amperometric Immunosensor for Detection of Plasmodium falciparum Histidine-Rich Protein 2 in Serum of Humans with Malaria: Comparison with a Commercial Kit, J. Clin. Microbiol. 46 (2008) 3759–3765. https://doi.org/10.1128/JCM.01022-08.

[189] M. Heutmekers, P. Gillet, J. Maltha, A. Scheirlinck, L. Cnops, E. Bottieau, M.V. Esbroeck, J. Jacobs, Evaluation of the rapid diagnostic test CareStart pLDH Malaria (Pf-pLDH/pan-pLDH) for the diagnosis of malaria in a reference setting, Malar. J. 11 (2012) 1–10. https://doi.org/10.1186/1475-2875-11-204.

[190] WHO | The role of RDTs in malaria control, WHO. (n.d.). https://www.who.int/malaria/areas/diagnosis/rapid-diagnostic-tests/role_in_malaria_control/en/ (accessed August 25, 2020).

[191] N. Nakatsuka, K.-A. Yang, J.M. Abendroth, K.M. Cheung, X. Xu, H. Yang, C. Zhao, B. Zhu, Y.S. Rim, Y. Yang, P.S. Weiss, M.N. Stojanović, A.M. Andrews, Aptamer–field-effect transistors overcome Debye length limitations for small-molecule sensing, Science. 362 (2018) 319–324. https://doi.org/10.1126/science.aao6750.

[192] Y.H. Ding, P. Zhang, Q. Zhuo, H.M. Ren, Z.M. Yang, Y. Jiang, A green approach to the synthesis of reduced graphene oxide nanosheets under UV irradiation, Nanotechnology. 22 (2011) 215601. https://doi.org/10.1088/0957-4484/22/21/215601.

[193] S. Stankovich, D.A. Dikin, R.D. Piner, K.A. Kohlhaas, A. Kleinhammes, Y. Jia, Y. Wu, S.T. Nguyen, R.S. Ruoff, Synthesis of graphene-based nanosheets via chemical reduction of exfoliated graphite oxide, Carbon. 45 (2007) 1558–1565. https://doi.org/10.1016/j.carbon.2007.02.034.

[194] W. Fu, L. Feng, D. Mayer, G. Panaitov, D. Kireev, A. Offenhäusser, H.-J. Krause, Electrolyte-Gated Graphene Ambipolar Frequency Multipliers for Biochemical Sensing, Nano Lett. 16 (2016) 2295–2300. https://doi.org/10.1021/acs.nanolett.5b04729.

[195] W. Fu, L. Feng, G. Panaitov, D. Kireev, D. Mayer, A. Offenhäusser, H.-J. Krause, Biosensing near the neutrality point of graphene, Sci. Adv. 3 (2017) e1701247. https://doi.org/10.1126/sciadv.1701247.

[196] F. Schedin, A.K. Geim, S.V. Morozov, E.W. Hill, P. Blake, M.I. Katsnelson, K.S. Novoselov, Detection of individual gas molecules adsorbed on graphene, Nat. Mater. 6 (2007) 652–655. https://doi.org/10.1038/nmat1967.

[197] W.-M. Munief, X. Lu, T. Teucke, J. Wilhelm, A. Britz, F. Hempel, R. Lanche, M. Schwartz, J.K.Y. Law, S. Grandthyll, F. Müller, J.-U. Neurohr, K. Jacobs, M. Schmitt, V. Pachauri, R. Hempelmann, S. Ingebrandt, Reduced graphene oxide biosensor platform for the detection of NT-proBNP biomarker in its clinical range, Biosens. Bioelectron. 126 (2019) 136–142. https://doi.org/10.1016/j.bios.2018.09.102.

[198] I.-Y. Sohn, D.-J. Kim, J.-H. Jung, O.J. Yoon, T. Nguyen Thanh, T. Tran Quang, N.-E. Lee, pH sensing characteristics and biosensing application of solution-gated reduced graphene oxide field-effect transistors, Biosens. Bioelectron. 45 (2013) 70–76. https://doi.org/10.1016/j.bios.2013.01.051.

[199] D.-J. Kim, I.Y. Sohn, J.-H. Jung, O.J. Yoon, N.-E. Lee, J.-S. Park, Reduced graphene oxide field-effect transistor for label-free femtomolar protein detection, Biosens. Bioelectron. 41 (2013) 621–626. https://doi.org/10.1016/j.bios.2012.09.040.

[200] F. Chen, Q. Qing, J. Xia, J. Li, N. Tao, Electrochemical Gate-Controlled Charge Transport in Graphene in Ionic Liquid and Aqueous Solution, J. Am. Chem. Soc. 131 (2009) 9908–9909. https://doi.org/10.1021/ja9041862.

[201] R.M. Dirkzwager, A.B. Kinghorn, J.S. Richards, J.A. Tanner, APTEC: aptamer-tethered enzyme capture as a novel rapid diagnostic test for malaria, Chem. Commun. 51 (2015) 4697–4700. https://doi.org/10.1039/C5CC00438A.

[202] A. Minopoli, B. Della Ventura, B. Lenyk, F. Gentile, J.A. Tanner, A. Offenhäusser, D. Mayer, R. Velotta, Ultrasensitive antibody-aptamer plasmonic biosensor for malaria biomarker detection in whole blood, Nat. Commun. 11 (2020) 6134. https://doi.org/10.1038/s41467-020-19755-0.
[203] B. Lenyk, G. Figueroa-Miranda, I. Pavlushko, Y. Lo, J.A. Tanner, A. Offenhäusser, D. Mayer, Dual-Transducer Malaria Aptasensor Combining Electrochemical Impedance and Surface Plasmon Polariton Detection on Gold Nanohole Arrays, ChemElectroChem. 7 (2020) 4594–4600. https://doi.org/10.1002/celc.202001212.
[204] D.K. Shoemark, M.J. Cliff, R.B. Sessions, A.R. Clarke, Enzymatic properties of the lactate dehydrogenase enzyme from Plasmodium falciparum, FEBS J. 274 (2007) 2738–2748. https://doi.org/10.1111/j.1742-4658.2007.05808.x.

Acknowledgments

To my supervisor Prof. Andreas Offenhäusser for his support in this project for the realization of my doctoral degree and for his unconditional support towards my future professional plans. Thank you very much, Chef.

To my second supervisor Prof. Sven Ingebrandt for supporting my application to the engineering degree, for the nice work collaboration with his Institute, and for his support towards my future professional plans. Many thanks, Prof. Ingebrandt.

To my third supervisor Prof. Lothar Elling for supporting my first application to the faculty, for his nice collaboration and feedback on the PEG work. Many thanks, Prof. Elling.

To my dear supervisor and one of my mentors, Dirk Mayer, for his unconditional guiding and support through the realization of this really nice work and for being my blood donor. Infinite thanks, Dirk.

To former Professor and first mentor, Francisco Buenrostro Zagal, for teaching me a lot of things, for helping and supporting my professional and personal growth. Especially for teaching me the importance of “sentipensar”. Infinite thanks, Frans.

To my lovely family, especially my parents, not only for giving me the life, but also for, no matter what, always supporting all my dreams. Thank you so much, family.

To my lovely boyfriend, Stefan Kirch, for your support, for your help, for encouraging me. Thank you for giving more meaning and more fun to this life, honey.

To my friends from Mexico and Germany for providing emotional support and fun through this doctoral phase. Many thanks to all.

To my colleagues (Yuting, Yuanying, Lena, Bohdan, Changtong, Viviana) from IBI-3 Institute for teaching, helping, and having funny moments through the daily work. Thank you so much to all.

Last but not least, to my sponsors the Mexican National Council for Science and Technology (CONACyT) and the German Academic Exchange Service (DAAD), for economically supporting the realization of my doctoral study.

Appendix A: Nomenclature

Acronyms / Abbreviations

AFM	Atomic Force Microscopy
Apt	Aptamer
BSA	Bovine Serum Albumin
CC	Chronocoulometry
CE	Counter Electrode
CV	Cyclic Voltammetry
DPV	Differential Pulse Voltammetry
EDL	Electrical Double Layer
EEC	Electrical Equivalent Cicuit
EIS	Electrochemical Impedance Spectroscopy
ESA	Electrochemical Surface Area
flex-MEA	flexible Multielectrode Array
GRE	Gold Rod Electrode
hLDHB	human Lactate Dehydrogenase B
HRP-2	Histidine-Rich Protein 2
HS	Human Serum
HSA	Human Serum Albumin
LOD	Limit of Detection
MCH	6-Mercapto-hexanol
PEG	Polyethylene glycol
PET	Polyethylene terephthalate
PfLDH	*Plasmodium falciparum* Lactate Dehydrogenase
pI	Isoelectric point
POC	Point-of-care

PSA	Prostate-Specific Antigen
PvLDH	*Plasmodium vivax* Lactate Dehydrogenase
QCM-D	Quartz Crystal Microbalance with Dissipation
RBC	Red Blood Cell
RDT	Rapid Diagnostic Test
RE	Reference Electrode
rGO-FET	reduced Graphene Oxide Field-Effect Transistor
RTA	Rapid Thermal Annealing
SELEX	Systematic Evolution of Ligands by Exponential Enrichment
ssDNA	single-stranded DeoxyriboNucleic Acid
WE	Working Electrode
WHO	World Health Organization
XPS	X-ray Photoelectron Spectroscopy

Appendix B: Supporting images and table for results and discussion

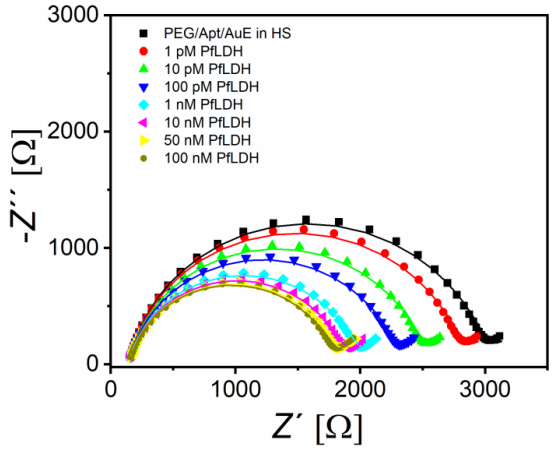

Figure S1 Nyquist plot showing the different concentrations of PfLDH detected for *in situ* detection from a range of 1 pM to an observed saturation of 100 nM.

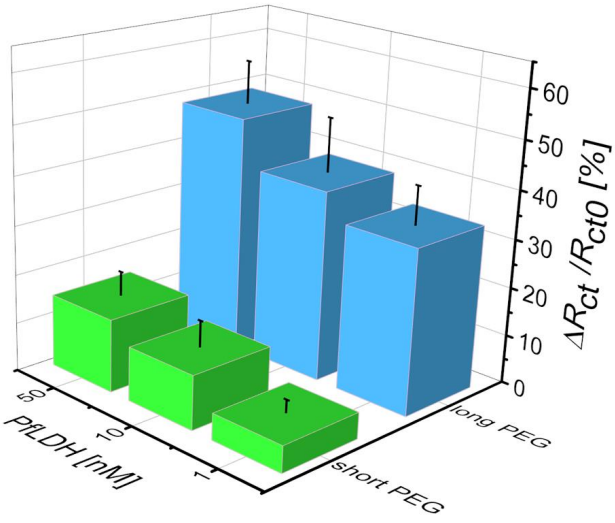

Figure S2 Comparison of the blocking performance of short PEG (400 Da, green) and long PEG (2 kDa, blue) molecules for different PfLDH concentration detection in human serum.

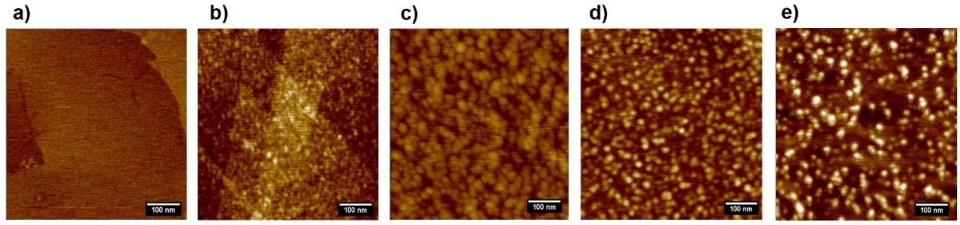

Figure S3 Tapping mode AFM image for a bare single-crystal gold (111) surface (a), after aptamer immobilization (b), and additional PEG binding for 2 h (c), 7 h PEG (d); and 16 h PEG (e) with aptamer concentration of 0.1 µM. The color scale of a) goes from -1.2 nm to 1.2 nm; the color scales from b)-e) go from -2 to 2 nm.

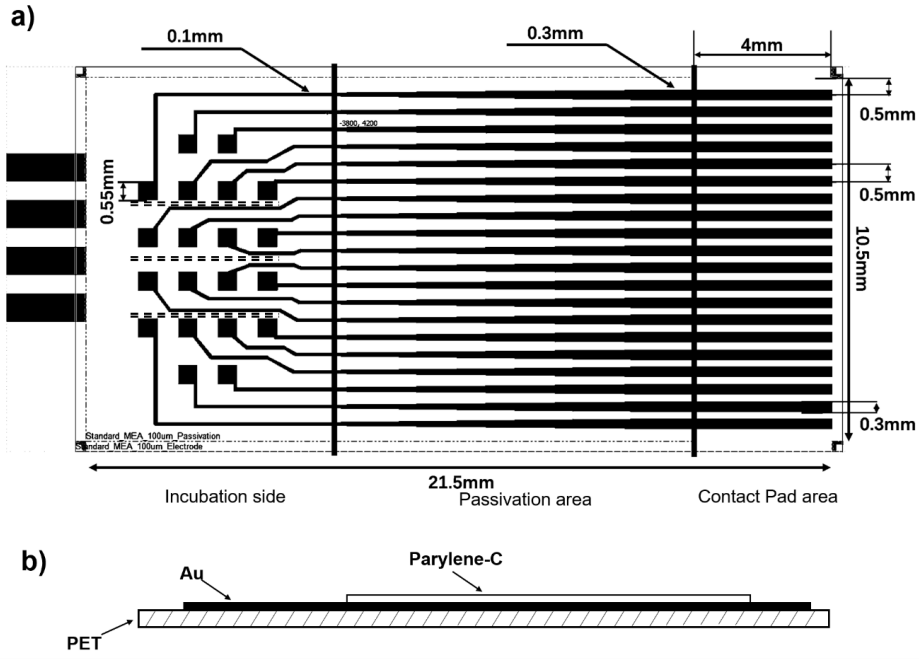

Figure S4 a) Top-view of flex-MEA layout. The double dashed lines represent the cutting area for the generation of different electrode sets to realize the immobilization of different aptamers. The Incubation side, Passivation area, and Contact Pad area are also indicated. b) Side-view of the flex-MEA, including PET substrate, gold (Au) metal, and Parylene-C passivation.

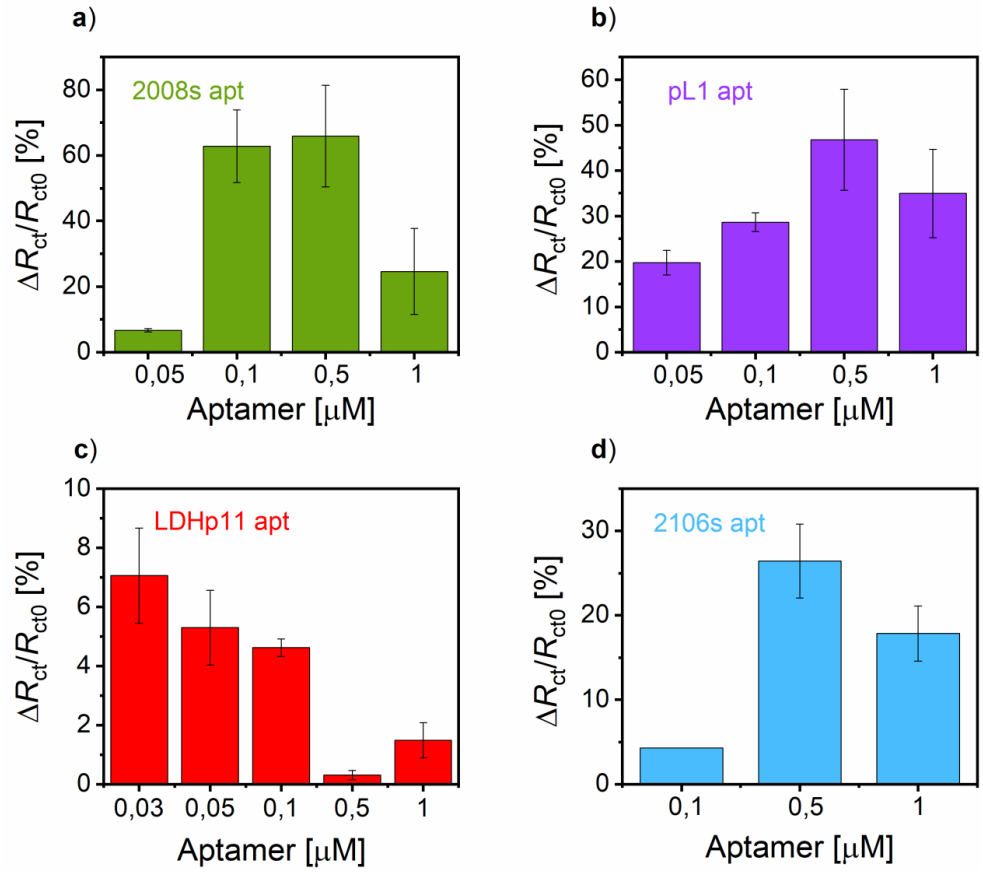

Figure S5 Different aptamer concentrations tested for optimized aptasensor signals with 10 nM PfLDH protein for 2008s, pL1, and LDHp11 aptamers and 10 nM HRP-2 protein for 2106s aptamer.

Table S1 Electrochemical surface area **(**ESA) of different electrodes.

Electrode	Area (mm^2)
GRE	3.5 ± 0.27
flex-MEA	
E1	1.56 ± 0.15
E3	0.90 ± 0.09
E5	0.91 ± 0.10
E7	0.73 ± 0.06
E9	0.70 ± 0.08
E11	0.88 ± 0.10
E13	1.05 ± 0.09
E15	0.60 ± 0.08

GRE: gold rod electrode; flex-MEA: flexible multielectrode array.

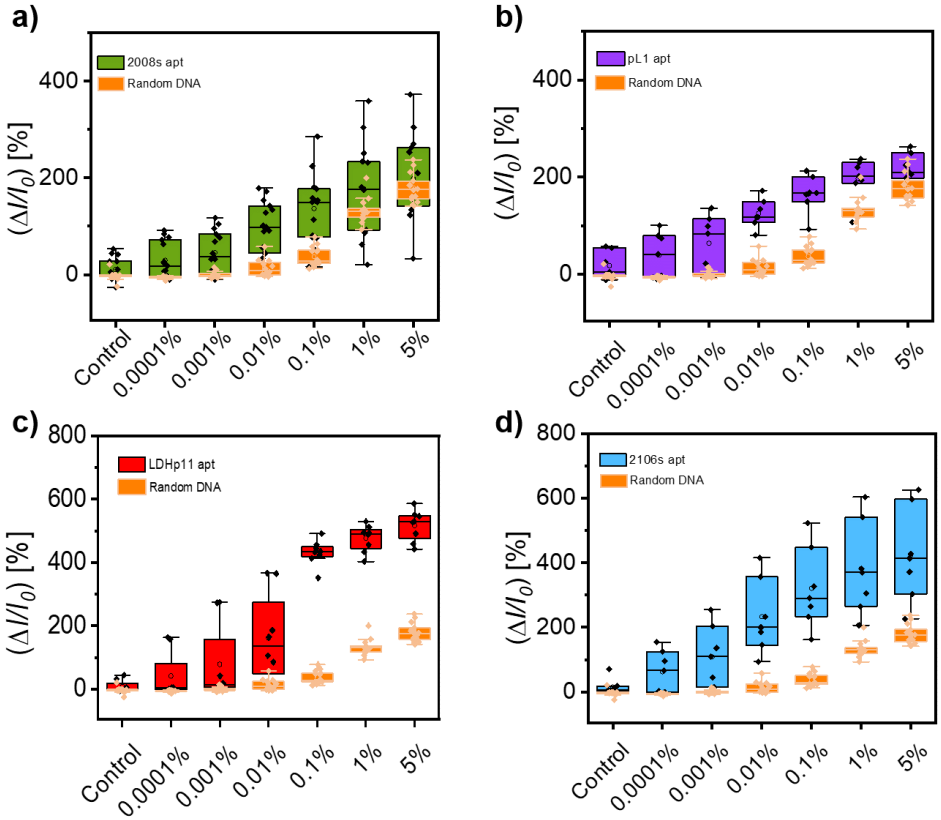

Figure S6 Comparison of specific biomarker detection by aptamers versus a random ssDNA sequence in blood samples with spiked *Plasmodium falciparum* parasites. The % represents the percent of parasitemia.

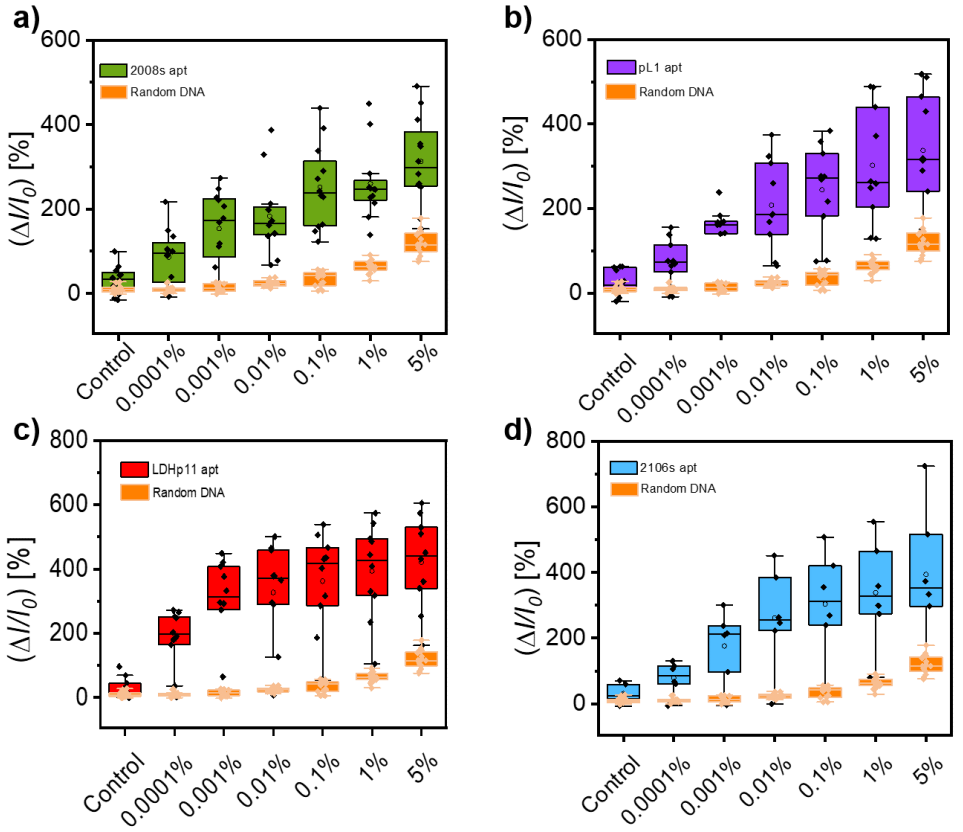

Figure S7 Comparison of specific biomarker detection by aptamers versus a random ssDNA sequence in *Plasmodium falciparum* parasite culture samples. The % represents the percent of parasitemia.

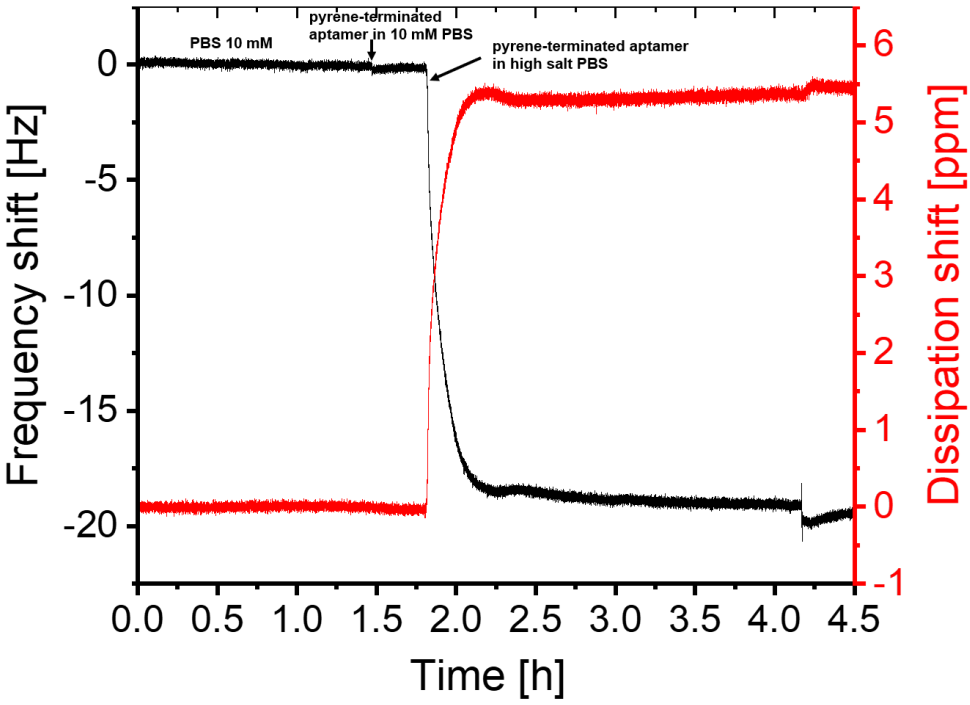

Figure S8 QCM-D measurement for pyrene-terminal aptamer immobilization in low salt 10 mM PBS (0.1 M NaCl) and high salt 10 mM PBS (1 M NaCl).

Author´s List of Publications

Gabriela Figueroa-Miranda, Lingyan Feng, Simon Chi-Chin Shiu, Roderick Marshall Dirkzwager, Yee-Wai Cheung, Julian Alexander Tanner, Michael Josef Schöning, Andreas Offenhäusser, Dirk Mayer. Aptamer-based electrochemical biosensor for highly sensitive and selective malaria detection with adjustable dynamic response range and reusability. Sensors and Actuators B: Chemical. 2018, 255, 235-243.

Yuting Zhang, **Gabriela Figueroa-Miranda**, Zhaozi Lyu, Christian Zafiu, Dieter Willbold, Andreas Offenhäusser, Dirk Mayer. Monitoring amyloid-β proteins aggregation based on label-free aptasensor. Sensors and Actuators B: Chemical. 2019, 288, 535-542.

Yuanying Liang, Changtong Wu, **Gabriela Figueroa-Miranda**, Andreas Offenhäusser, Dirk Mayer. Amplification of aptamer sensor signals by four orders of magnitude via interdigitated organic electrochemical transistors. Biosensors and Bioelectronics. 2019, 144, 111668.

Yuting Zhang, **Gabriela Figueroa-Miranda**, Christian Zafiu, Dieter Willbold, Andreas Offenhäusser, Dirk Mayer. Amperometric aptasensor for amyloid-beta oligomer detection by optimized stem-loop structures with adjustable detection range. ACS Sensors. 2019, 4, 11, 3042-3050.

Gabriela Figueroa-Miranda, Changtong Wu, Yuting Zhang, Lena Nörbel, Young Lo, Julian Alexander Tanner, Lothar Elling, Andreas Offenhäusser, Dirk Mayer. Polyethylene glycol-mediated blocking and monolayer morphology of an electrochemical aptasensor for malaria biomarker detection in human serum. Bioelectrochemistry. 2020, 107589.

Yuting Zhang, **Gabriela Figueroa-Miranda**, Changtong Wu, Dieter Willbold, Andreas Offenhäusser, Dirk Mayer. Electrochemical dual-aptamer biosensors based on nanostructured microelectrode arrays for the detection of neuronal biomarkers. Nanoscale. 2020, 31, 16501-16513.

Gabriela Figueroa-Miranda[†], Bohdan Lenyk[†], Ivan Pavlushko, Young Lo, Julian A. Tanner, Andreas Offenhäusser, and Dirk Mayer. Dual-Transducer Malaria Aptasensor Combining Electrochemical Impedance and Surface Plasmon Polariton Detection on Gold Nanohole Arrays. ChemElectroChem. 2020, 7, 4594–4600.

[†] contributed equally as the first author to this work

Young Lo, Yee-Wai Cheung, Lin Wang, Megan Lee, **Gabriela Figueroa-Miranda**, Shaolin Liang, Dirk Mayer, Julian Alexander Tanner. An electrochemical aptamer-based biosensor targeting Plasmodium falciparum histidine-rich protein II for malaria diagnosis. Biosensors and Bioelectronics. 2021, 192, 113472.

Gabriela Figueroa-Miranda, Song Chen, Marc Neis, Lei Zhou, Yuting Zhang, Young Lo, Julian A. Tanner, Andrea Kreidenweiss, Andreas Offenhäusser, Dirk Mayer. Multi-target electrochemical malaria aptasensor on flexible multielectrode arrays for detection in malaria parasite blood samples. Sensors and Actuators B: Chemical. 2021, 349, 130812.

Gabriela Figueroa-Miranda, Yuanying Liang, Mohit Suranglikar, Matthias Stadler, Nagesh Samane, Marcel Tintelott, Young Lo, Julian A. Tanner, Xuan T. Vu, Joachim Knoch, Sven Ingebrandt, Andreas Offenhäusser, Vivek Pachauri, Dirk Mayer. Delineating charge and capacitance transduction in system-integrated graphene-based BioFETs used as aptasensors for malaria detection. Manuscript submitted for publication. 2021.

Author´s List of Patents

Gabriela Figueroa Miranda, Viviana Rincón Montes, Michael Prömpers, Andreas Offenhäusser, Dirk Mayer. “Biosensor basierend auf flexiblen Multielektroden-Feldern für elektrochemische Detektion von multiplen Malaria-Biomarkern“. DE 102021100290.7, filed 11.01.2021.

Band / Volume 62
Development of Electromagnetic Induction Measurement and Inversion Methods for Soil Electrical Conductivity Investigations
X. Tan (2020), ix, 124 pp
ISBN: 978-3-95806-490-4

Band / Volume 63
Novel System Approach for a mm-range Precision Indoor Positioning System
R. Xiong (2020), xi, 144 pp
ISBN: 978-3-95806-517-8

Band / Volume 64
Quantitative investigation of group III-nitride interfaces by a combination of scanning tunneling microscopy and off-axis electron holography
Y. Wang (2021), 102 pp
ISBN: 978-3-95806-534-5

Band / Volume 65
Scalable Control Electronics for a Spin Based Quantum Computer
L. Geck (2021), xiv, 114, xv-xxxiii
ISBN: 978-3-95806-540-6

Band / Volume 66
DNA-capped silver nanoparticles for stochastic nanoparticle impact electrochemistry
L. Nörbel (2021), VI, 142 pp
ISBN: 978-3-95806-541-3

Band / Volume 67
Development, characterization, and application of intraretinal implants
V. Rincón Montes (2021), XII, 173 pp
ISBN: 978-3-95806-553-6

Band / Volume 68
Optogenetic and electrical investigation of network dynamics in patterned neuronal cultures
T. J. J. Hondrich (2021), x, 177 pp
ISBN: 978-3-95806-555-0

Band / Volume 69
Disentangling parallel conduction channels by charge transport measurements on surfaces with a multi-tip scanning tunneling microscope
S. Just (2021), xii, 225 pp
ISBN: 978-3-95806-574-1

Band / Volume 70
Nanoscale four-point charge transport measurements in topological insulator thin films
A. Leis (2021), ix, 153 pp
ISBN: 978-3-95806-580-2

Band / Volume 71
Investigating the Interaction between π-Conjugated Organic Molecules and Metal Surfaces with Photoemission Tomography
X. Yang (2021), xviii, 173 pp
ISBN: 978-3-95806-584-0

Band / Volume 72
Three-Dimensional Polymeric Topographies for Neural Interfaces
F. Milos (2021), 133 pp
ISBN: 978-3-95806-586-4

Band / Volume 73
Development, characterization, and application of compliant intracortical implants
K. Srikantharajah (2021), xiv, 155, xv-xvii pp
ISBN: 978-3-95806-587-1

Band / Volume 74
Modelling, implementation and characterization of a Bias-DAC in CMOS as a building block for scalable cryogenic control electronics for future quantum computers
P. N. Vliex (2021), xiv, 107, xv-xxviii pp
ISBN: 978-3-95806-588-8

Band / Volume 75
Development of Electrochemical Aptasensors for the Highly Sensitive, Selective, and Discriminatory Detection of Malaria Biomarkers
G. Figueroa Miranda (2021), XI, 135 pp
ISBN: 978-3-95806-589-5

Information
Band / Volume 75
ISBN 978-3-95806-589-5

Mitglied der Helmholtz-Gemeinschaft

JÜLICH
Forschungszentrum